



**HAL**  
open science

# Slab-derived metasomatism in the Carpathian-Pannonian mantle revealed by investigations of mantle xenoliths from the Bakony-Balaton Highland Volcanic Field

Laura Créon, Guillaume Delpech, Virgile Rouchon, François Guyot

► **To cite this version:**

Laura Créon, Guillaume Delpech, Virgile Rouchon, François Guyot. Slab-derived metasomatism in the Carpathian-Pannonian mantle revealed by investigations of mantle xenoliths from the Bakony-Balaton Highland Volcanic Field. *Lithos*, 2017, 286-287, pp.534 - 552. 10.1016/j.lithos.2017.06.004 . hal-01637216

**HAL Id: hal-01637216**

**<https://ifp.hal.science/hal-01637216>**

Submitted on 17 Nov 2017

**HAL** is a multi-disciplinary open access archive for the deposit and dissemination of scientific research documents, whether they are published or not. The documents may come from teaching and research institutions in France or abroad, or from public or private research centers.

L'archive ouverte pluridisciplinaire **HAL**, est destinée au dépôt et à la diffusion de documents scientifiques de niveau recherche, publiés ou non, émanant des établissements d'enseignement et de recherche français ou étrangers, des laboratoires publics ou privés.

1 **Slab-derived adakitic metasomatism in the Carpathian-Pannonian mantle**  
2 **revealed by mantle xenolith investigations from the Bakony-Balaton**  
3 **Highland Volcanic Field**

4  
5 *Laura Créon<sup>a</sup>, Guillaume Delpech<sup>b</sup>, Virgile Rouchon<sup>a</sup> and François Guyot<sup>c</sup>*

6  
7 *<sup>a</sup> IFP Energies nouvelles, 1 & 4 avenue Bois Préau, 92852 Rueil-Malmaison Cedex, France ; <sup>b</sup> Geosciences*  
8 *Paris Sud department, Paris Sud University, Bâtiment 504, 91405 Orsay Cedex, France ; <sup>c</sup> IMPMC, Museum*  
9 *National d'histoire Naturelle, Sorbonne Universités, CNRS, UPMC, IRD, 61 Rue Buffon, 75005 Paris, France ;*

10  
11 Corresponding Author: Laura Créon, [lauracreon@gmail.com](mailto:lauracreon@gmail.com); Present address: Universidad  
12 Nacional Autónoma de México, Centro de Geociencias, Campus Juriquilla, A.P. 1-742,  
13 Boulevard Juriquilla No. 3001, Juriquilla. Qro., C.P. 76230

14  
15 Abstract

16  
17 We report new major and trace element data on minerals and glass from fifteen xenoliths from  
18 four different locations (Szentbékállá, Szigliget, Füzes-tó and Mindszentkállá) in the  
19 Bakony-Balaton Highland Volcanic Field (Pannonian Basin, Central Europe). We show  
20 evidences for different stages of partial melting and metasomatism in the lithospheric mantle.

21 The relict mantle minerals show compositions related to previous lithospheric mantle  
22 conditions, resulting from (1) an important early stage partial melting (~10-15 %) event  
23 indicated by a low modal content of clinopyroxene (cpx) 4-9 vol. % and low HREE contents  
24 in cpx ((La/Yb)<sub>N</sub> = 0.2 to 0.8), and (2) a metasomatic event associated to the crystallization of  
25 pargasite amphiboles and enrichment of cpx trace element patterns ((La/Yb)<sub>N</sub> = 0.7 to 15.7).

26 A more recent metasomatic event is widespread and associated to the breakdown of

27 amphibole and to the formation of silicate melt pockets, forming a network of melt veins and  
28 pockets associated with large CO<sub>2</sub> vesicles at grain boundaries. The melt in veins is trachy-  
29 andesitic and displays trace element patterns very distinct from the andesitic melt in pockets,  
30 the latter resulting from *in situ* amphibole breakdown. The melt in veins records the extraction  
31 and onset of migration of a silicic melt with high-Nb and adakitic affinities (high SiO<sub>2</sub> = 54.2  
32 to 62.7 wt. % and high LREE contents (La/Yb)<sub>N</sub> = 2.6 to 68.5). Adakite-like melts are  
33 believed to have been produced at conditions of 1000-1200°C and 2-3 GPa from a subducting  
34 slab, and injected in the lithospheric mantle where they triggered widespread pargasite  
35 melting at 1200°C and pressures above 0.7-1.1 GPa, below Moho depths. We suggest that this  
36 late stage metasomatic event is associated to the calc-alkaline volcanic suite that was active  
37 throughout most of the Miocene during the formation of the Pannonian Basin. This late stage  
38 event is also believed to have injected large amounts of CO<sub>2</sub> in the lithosphere mantle.

39

## 40 1 Introduction

41

42 Quenched melts in the form of glasses have been extensively reported in mantle xenoliths  
43 from many locations worldwide; they commonly occur in veins as intergranular films and/or  
44 as pockets between the primary minerals, or as inclusions in primary mantle minerals (e.g.,  
45 [Coltorti et al., 1999](#); [Yaxley and Kamenetsky, 1999](#); [Beccaluva et al., 2001](#); [Shaw et al., 2006](#);  
46 [Lu et al., 2015](#)). The occurrence of glass provides important information on chemical and  
47 physical processes occurring in the lithospheric mantle, such as partial melting and  
48 metasomatism. Glasses in mantle xenoliths show a very wide range of compositions, from  
49 carbonate-rich melts ([Coltorti et al., 1999](#); [Delpech et al., 2004](#); [Moine et al., 2004](#)), to highly  
50 silicic melts (e.g., [Wulff-Pederson et al. 1999](#)).

51 Different origins for glasses in mantle xenoliths have been proposed on the basis of  
52 mineralogical observations, geochemical datasets and experimental results. Such melts have  
53 been interpreted either as agents or products of mantle metasomatism (e.g., [Coltorti et al.,](#)  
54 [1999](#); [Beccaluva et al., 2001](#); [Neumann et al., 2002](#); [Ionov et al., 2005](#)), or the products of in  
55 situ incongruent melting of pre-existing minerals (e.g., [Laurora et al., 2001](#)) prior to or during  
56 entrainment of the xenoliths. There are also compelling evidence for the circulation of  
57 volatile-rich fluids that play a significant role as efficient metasomatic agents (e.g. [Szabó et al.](#)  
58 [1996](#); [Dawson 1984](#)). Another alternative explanation is that the melts are the products of  
59 reaction between xenoliths and their host magma due to chemical disequilibrium (e.g., [Shaw](#)  
60 [et al., 2006](#); [Shaw and Dingwell, 2008](#); [Miller et al., 2012](#)) during their transport to the Earth's  
61 surface.

62 [Embey-Isztin & Scharbert \(2001\)](#) and [Bali et al. \(2002\)](#) suggested that melt pockets in  
63 ultramafic xenoliths from the Bakony–Balaton Highland Volcanic Field (BBHVF, Western  
64 Hungary) formed by reactions between pre-existing mantle phases (clinopyroxene  $\pm$   
65 amphibole) and metasomatic agents that were compositionally distinct from the host alkali  
66 basalts. The infiltrating melts were inferred to have originated from melting of previously  
67 metasomatized upper mantle during the Middle Miocene mantle upwelling ([Huisman et al.,](#)  
68 [2002](#)). [Bali et al. \(2002; 2008a; 2008b\)](#) and [Szabó et al. \(2009\)](#) also showed that migrating  
69 melts within the lithospheric mantle beneath the BBHVF have strong affinities with  
70 subduction-related melts/fluids or slab melts.

71 In this contribution, we present new major and trace element data on minerals and glass from  
72 fifteen xenoliths from four different BBHVF locations (Szentbékállá, Szigliget, Füzes-tó and  
73 Mindszentkállá), two of which having never been published before in the literature for mantle  
74 xenoliths (Füzes-tó and Mindszentkállá). This new dataset, together with textural features,  
75 allows further constraining the origin of the metasomatic agents migrating through the

76 lithospheric mantle beneath the Pannonian Basin and their chemical reactions with the host  
77 lithospheric mantle. Based on the results, two metasomatic and partial melting events are  
78 recognized. The source of the last metasomatic event is also constrained.

79

## 80 2 Geological background

81

### 82 2.1 Geodynamic context

83

84 The Pannonian Basin (PB) is located in Central Europe and is part of the Carpathian–  
85 Pannonian region (CPR). The PB is surrounded by the Carpathian fold and thrust belt to the  
86 east and north, and by the Alps to the west and Dinarides to the south (Fig.1).

87 The CPR is composed of the ALCAPA (ALpian–CARpathian PANnonian) and the Tisza–  
88 Dacia tectonic units that are separated by a major shear zone, the Middle Hungarian Zone.

89 The PB is a typical inter-arc basin ([Embey-Isztin et al., 2001](#)); nevertheless, it shows a  
90 number of features characteristic of rift zones, such as high heat flow, recent alkali basaltic  
91 volcanism, a thin crust and lithospheric mantle, and a doming asthenosphere ([Spakman, 1990](#);  
92 [Falus et al., 2007](#)). The major driving forces that led to the formation of the Pannonian Basin  
93 (~20 Ma) were the continuous subduction and roll-back on its eastern boundaries and the  
94 synchronous eastward extrusion of ALCAPA blocks ([Kazmer and Kovacs, 1985](#)) from the  
95 Alpine compressional belt ([Csontos et al., 1992](#); [Horvath, 1993](#); [Fodor et al., 1999](#)).

96 The Pannonian Basin has experienced several geodynamic events during Miocene to  
97 Pleistocene times ([Bali et al. 2008](#)): (1) an early extensional phase during Miocene, related to  
98 the roll-back of the subducting European plate ([Csontos et al., 1992](#); [Horvath, 1993](#)), resulting  
99 in a lithospheric thinning over the entire basin; (2) a short-lived compressional event during  
100 late Miocene to Pleistocene ([Fodor et al., 1999](#)); and (3) a late extensional phase during the

101 Plio-Pleistocene that affected the central part of the Carpathian–Pannonian region (Bada et al.,  
102 1999; Huisman et al., 2002). An extensive volcanic activity followed this second rifting  
103 phase ( $7.96 \pm 0.03$  to  $2.61 \pm 0.03$  Ma, Wijbrans et al. 2007) during which formed the Bakony–  
104 Balaton Highland Volcanic Field (BBHVF).

105

## 106 2.2 The Bakony–Balaton Highland Volcanic Field (BBHVF)

107

108 The Bakony–Balaton Highland Volcanic Field (BBHVF) is situated in the northern part of the  
109 Lake Balaton (western Hungary, Fig.1). It is a well-studied young volcanic area on the  
110 southern margin of the ALCAPA microplate, which is located in the center of the Carpathian–  
111 Pannonian region and in the central southeastern part of the ALCAPA mega unit (Bali et al.  
112 2008). The BBHVF itself has more than 50 basaltic volcanoes in a relatively small (around  
113  $3500 \text{ km}^2$ ) area (Martin et al., 2003; Kereszturi et al., 2011). The volcanic centers of the  
114 BBHVF were active between 7.96 Ma and 2.61 Ma (Balogh and Pécskay, 2001; Balogh and  
115 Németh, 2005; Wijbrans et al., 2007; Szabó et al., 2010) and produced mostly alkali basaltic  
116 volcanics (Szabó et al., 1992; Embey-Isztin et al., 1993). The Szigliget, Mindszentkállya and  
117 Füzes-tó volcanic events are respectively dated at 4.2-3.9 Ma, 2.8-2.6 Ma and 2.6 Ma. The  
118 age of the Szentbékállya volcanic event is not known.

119 Ultramafic xenoliths can be found in basaltic lava flows and pyroclastic products at six  
120 locations (Tihany, Bondoró Hill, Füzes-tó, Szentbékállya, Mindszentkállya, and Szigliget).

121 Most xenoliths are spinel-bearing lherzolites; however, spinel-bearing harzburgites,  
122 clinopyroxenites, orthopyroxenites, wehrlites, websterites and more rarely, composite  
123 xenoliths were also found. The lithospheric mantle beneath the BBHVF is more deformed  
124 than the known mantle portions on the edges of the Carpathian–Pannonian region (Downes et  
125 al., 1992; Szabó et al., 1995). The most common textural type in peridotites is equigranular

126 (e.g. [Downes et al., 1992](#); [Szabó et al., 2004](#); [Embey-Isztin et al., 2014](#)), whereas xenoliths  
127 with protogranular, porphyroclastic and poikilitic are rarer. The peridotite xenoliths contain  
128 olivine (ol), orthopyroxene (opx), clinopyroxene (cpx) and spinel (sp) as primary minerals.  
129 The equilibrium temperatures of BBHVF mantle xenoliths vary between 880 and 1090 °C  
130 ([Downes et al., 1992](#); [Szabó et al., 1995](#); [Bali et al., 2002](#); [Kovacs et al., 2012](#)). Using the  
131 geotherm of [Kovacs et al. \(2012\)](#), the sampling depths represent a mantle column of about 33  
132 to 56 km and correspond to pressures between 0.95 and 1.60 GPa.  
133 The occurrence of middle and lower crustal xenoliths in the BBHVF are also described by  
134 [Szabó et al. \(2010\)](#) and references therein. These crustal xenoliths were brought to the surface  
135 by the BBHVF alkali volcanism. These granulites are composed of clinopyroxenes,  
136 plagioclases, garnets ± orthopyroxenes ± amphiboles ([Török et al., 2005](#)).

137

### 138 3 Petrography

139

#### 140 3.1 Petrography of the mantle xenoliths

141

142 More than 150 ultramafic xenoliths from the BBHVF (Szentbékállá, Szigliget, Füzes-tó and  
143 Mindszentkállá) were collected. After observation by optical microscopy, six ultramafic  
144 xenoliths from Szentbékállá, four from Szigliget, three from Füzes-tó and two from  
145 Mindszentkállá were selected for geochemical analyses (Table 1).

146 Selected samples are 7 to 18 cm in diameter, except one smaller sample from Mindszentkállá  
147 (2.5 cm in diameter). Xenoliths are composed of ol, opx, cpx and sp as primary minerals.

148 Point-counting analyses (400 points) indicate that most xenoliths are spinel-bearing  
149 peridotites (n = 13), ten of which are lherzolites and three are harzburgites (Fig. 2). The Cpx  
150 modal composition varies from 1.8 to 4 wt. % in harzburgites and from 6 to 18.5 wt. % in

151 lherzolites. Two samples (SZB51 and SZB66) were classified as cpx-poor lherzolites (<10%  
152 cpx).

153 Based on the classification of [Mercier & Nicolas \(1975\)](#), the xenoliths show either  
154 protogranular or equigranular microstructures. Samples with a protogranular microstructure  
155 display coarse grain sizes (2-6 mm), whereas those with equigranular microstructure are fine-  
156 grained (1-2 mm). Protogranular samples have grains of olivine and orthopyroxene with  
157 heterogeneous sizes (<1 to 5 mm) and show curvilinear grain boundaries and vermicular  
158 spinels. Most samples with an equigranular microstructure refer to the mosaic subtype variety  
159 (SZB44, SZB50, SZG30, FT12) and one has a tabular texture (FT08P). In these xenoliths,  
160 grains have straight grain boundaries and they very often show triple junctions with angles at  
161 120°. Spinel (and amphibole in FT08P) may be abundant in these samples (up to 12 vol. %)  
162 and it occurs as an interstitial (frequently) sub-euhedral mineral forming alignments of spinel  
163 aggregates. Two samples (SZG14, SZG44) display an intermediate microstructure grading  
164 from a protogranular to an equigranular texture. Some also display poikilitic features marked  
165 by poikilitic olivine enclosing opx or poikilitic opx enclosing olivine (Fig. 3b). There is no  
166 relationship between microstructures and the cpx modal contents of the peridotites.

167 Amphibole also occurs in some xenoliths (Szigliget, Füzes-tó and Mindszentkállya), regardless  
168 of the microstructure, as a secondary mineral disseminated between primary minerals (up to 7  
169 vol. %).

170

### 171 3.2 Petrography of melt pockets and veins

172

173 All the xenoliths in this study bear mineralogical evidence of melt and fluid circulation in  
174 both lherzolites and harzburgites such as fluid and silicate melt inclusions in primary minerals  
175 (opx, cpx, ol) and silicate glass in veins or melt pockets (Fig. 3). Clinopyroxenes sometimes



176 displays spongy rims when in contact with melt veins or melt pockets (Fig.3a). Spinel can  
177 also display spongy rims but in lower abundance. Melt pockets (Fig. 3d, e, g, h) were  
178 observed in seven samples in SZB44, SZB50, SZB51, SZG23, SZG44 and FT12 lherzolites  
179 and in FT08P harzburgite. The size of silicate melt pockets is variable and ranges from few  
180 hundred microns up to few millimeters in diameter (similar to those described by [Bali et al.,](#)  
181 [2002](#)). In most cases, they are connected to each other by a network of thin silicate melt veins  
182 occurring at the contacts or cross cutting primary minerals. The shape of melt pockets is  
183 mostly irregular or it may have the shape of ghost minerals that have entirely broken down  
184 (e.g. amphibole).

185 Melt pockets are composed of brownish glass (gl), in which euhedral to sub-hedral secondary  
186 minerals crystallized such as olivine (ol-II), clinopyroxene (cpx-II) and spinel (sp-II), all  
187 smaller than 0.3 mm in diameter. Most melt pockets also contain large vesicles (up to 0.5  
188 mm) (Fig. 3d, g, h). In xenoliths SZG23, FT12 and FT08P, melt pockets are associated with  
189 resorbed amphibole (amp-I). In this case, a resorbed amphibole crystal is often observed in  
190 the center of the pockets, surrounded by silicate glass and secondary minerals mentioned  
191 above. Some melt pockets are entirely composed of glass.

192 Melt veins (Fig. 3c) are observed in all samples and are mainly located at grain boundaries  
193 between primary minerals or cross-cut the primary mineralogy. The size of melt veins is  
194 variable (few tens of microns to 0.4 mm) and they are mainly composed of brownish glass  
195 and large vesicles (Fig. 3c), where ol-II, cpx-II, sp-II are present in lower abundance  
196 compared to melt pockets.

197

198 3.3 Petrography of silicate melt and fluid inclusions

199

200 Silicate melt inclusions (SMI) were only observed in the SZG14 lherzolite. They occur as  
201 primary inclusions (Roedder, 1984) in the rim of a clinopyroxene (Fig. 3a). The size of the  
202 primary SMI are 40, 60 and 100  $\mu\text{m}$  in diameter and their shape is spherical. The SMIs  
203 consist of brownish glass (50-70 vol. %), one  $\text{CO}_2$ -rich retraction bubble (10-25 vol. %) and  
204 tiny not identified mineral phases (10-40 vol. %).

205 Fluid inclusions are present by order of abundance (i.e. number of inclusions per unit volume  
206 of hosting mineral) in Opx, Cpx and Ol. They occur along healed fractures that crosscut the  
207 entire host crystal (Fig. 3f) as already described in the BBHVF by Bali, et al., (2008). The  
208 fluid inclusions display negative crystal shapes or have rounded shapes with sizes varying  
209 between 5 and 60  $\mu\text{m}$ . At room temperature, the fluid inclusions contain one (liquid) or two  
210 (liquid + vapor) phases. Using the definition of Roedder (1984), the inclusions can be  
211 classified as secondary fluid inclusions.

212

## 213 4 Geochemistry

214

### 215 4.1 Analytical methods

216

#### 217 4.1.1 Major and volatile element analyses

218

219 Electron microprobe analyses (EMPA) of mantle minerals, melt pockets and veins were  
220 carried out on a CAMECA SX FIVE at CAMPARIS (Jussieu, Paris, France). Minerals were  
221 analyzed with a focused beam (1-2  $\mu\text{m}$ ), a beam current of 20 nA and a counting time of 10 s  
222 for each element on peak and 10 s on background. Vanadium was determined with a beam  
223 current of 300 nA in all minerals. Glass was analyzed with a 10 nA defocused beam (10  $\mu\text{m}$ )  
224 and a counting of 10 s on the peak and 10 s on the background. The concentrations of S, Cl

225 and F were determined with a 45 nA defocused beam and a counting time of 100 s on peak.

226 Accuracy was checked against standards (albr, phn9, ortr, apat, mnti, baso, sca2 and Fe<sub>2</sub>O<sub>3</sub>).

227 Detection limits are <50 ppm for S, <60 ppm for F, <100 ppm for Cl, <300 ppm for P and

228 <1000 ppm for other major elements.

229

#### 230 4.1.2 Trace element analyses

231

232 Clinopyroxene, amphibole, and glass in melt pockets and veins were analyzed for trace

233 elements by laser ablation LA-ICP-MS, using a 193 nm ArF laser ablation system (Photon

234 Machine Analyte G2) coupled to an ICP-QMS (Varian 800-MS) at the Laboratoire de

235 Planétologie et de Géodynamique (LPGN, Nantes, France). Cpx and amphibole were

236 analyzed using a laser repetition rate of 5 Hz, a pulse energy of 6 mJ, a 65 to 85 μm laser spot

237 diameter, corresponding to a fluence between 4.08 and 7.26 J/cm<sup>2</sup>. Glass in melt pockets and

238 veins was analyzed using identical pulse frequency and energy, but with a 20 to 50 μm laser

239 spot diameter (fluence of 5.45 J/cm<sup>2</sup>). The background was measured for 30 s before ablation

240 and each analysis lasted for about 90 s. Measurements were calibrated against NIST 612 glass

241 standard ([Gagnon et al., 2008](#)), using CaO for Cpx and amphibole, and Al<sub>2</sub>O<sub>3</sub> for glass as

242 internal standards (measured by EMPA). Reproducibility and accuracy were characterized

243 using the BCR-2G international standard, which was analyzed at the beginning and end of

244 each run as well as every series of 10-15 unknown analyses. The analytical reproducibility is

245 better than 5% except for Cr, Th and U, which are better than 10%. Data reduction was

246 performed using the Glitter software ([Achterberg et al., 2001](#)).

247

#### 248 4.2 Chemistry of the primary mantle minerals

249

250 4.2.1 Major element analyses

251

252 No significant major element zonation was observed between cores and rims in the rock-  
253 forming minerals of peridotites from Szentbékállá, Szigliget, Füzes-tó and Mindszentkállá  
254 (Table 2).

255

256 4.2.1.1 Olivine

257

258 Primary olivines in lherzolites have homogeneous compositions and relatively low Mg-  
259 number (88.8-90.6). Their Mg-numbers are slightly higher in the spinel harzburgites (90.2–  
260 90.4) than in the other xenoliths. NiO contents in olivines from harzburgites and cpx-poor  
261 lherzolites vary from 0.33 to 0.41 wt. % and from 0.28 to 0.42 wt. % in the lherzolites. The  
262 Mg-numbers of secondary olivines (Ol II) in melt pockets are higher than those of primary  
263 olivines (89.7–92.7). Concentration of CaO (0.1–1.9 wt. %), Cr<sub>2</sub>O<sub>3</sub> (0.0– 0.3 wt. %) and  
264 Al<sub>2</sub>O<sub>3</sub> (0.0– 0.22 wt. %) in secondary olivines are higher than those in the primary olivines  
265 (Table 3).

266

267 4.2.1.2 Orthopyroxene

268

269 The composition of orthopyroxene ranges from En<sub>90.2</sub> to En<sub>91.3</sub> in harzburgites and from En<sub>89.0</sub>  
270 to En<sub>90.9</sub> in the lherzolites. The Al<sub>2</sub>O<sub>3</sub> contents (2.5–3.6 wt. %) of orthopyroxenes in the  
271 harzburgites and in the lherzolites (3.8-5.8 wt. %) are variable; the Cr<sub>2</sub>O<sub>3</sub> content is in the  
272 range of 0.0–0.1 wt. % in harzburgites and lherzolites orthopyroxenes (Table 2).

273

274 4.2.1.3 Clinopyroxene

275

276 Primary clinopyroxenes (Cpx I) are augites ( $\text{En}_{36.8-37.6} \text{Wo}_{35.5-36.8} \text{Fs}_{26.0-27.2}$ ). Their Mg-number  
277 ranges from 88.0 to 91.0 in the lherzolite and from 90.7 to 92.5 in the harzburgites. Major  
278 element contents of Cpx I in lherzolites are highly heterogeneous (Fig. 4) with higher  $\text{Al}_2\text{O}_3$   
279 and  $\text{Na}_2\text{O}$  and lower CaO content ( $\text{Al}_2\text{O}_3$  5.3-8.0 wt. %,  $\text{Na}_2\text{O}$  0.7-1.9 wt. % and CaO 17-8-  
280 21.6 wt. %, respectively) than in harzburgites ( $\text{Al}_2\text{O}_3$  2.2-4.1 wt. %;  $\text{Na}_2\text{O}$  0.3-1.2 wt. % and  
281 CaO 19.0-23.7 wt. %, respectively). Concentrations of  $\text{TiO}_2$  in Cpx I are  $< 0.94$  wt. % in  
282 lherzolites and between 0.1-0.2 in harzburgites (Table 2). The CaO (18.3-21.7 wt. %),  $\text{Al}_2\text{O}_3$   
283 (6.2-10.5 wt. %) and  $\text{TiO}_2$  (0.2-2.8 wt. %) contents of secondary cpx (Cpx II, augites,  $\text{En}_{40.7-}$   
284  $41.2 \text{Wo}_{28.8-29.2} \text{Fs}_{29.7-30.1}$ ) in melt pockets are higher than those of the primary clinopyroxenes  
285 for similar Mg-number (Fig.5, Table 3).

286

#### 287 4.2.1.4 Spinel

288

289 The primary spinel displays large variations in composition ranging from magnesian and  
290 aluminous chromite (SZB16, SZB44, SZB50, SZB52, SZG14, SZG30, SZG44, FT12,  
291 MSZK1308) to chromite (SZB51, SZB66, SZG23, FT01P, FT08P, MSZK1306A). The Mg-  
292 numbers and Cr-numbers range from 59.6 to 78.1 and from 7.7 to 43.9, respectively (Table 2,  
293 Fig. 4). The spinels in harzburgites are more chromiferous than in the lherzolites; the Mg-  
294 number versus Cr-number diagram (Fig. 4) shows a linear distribution from low Cr-number–  
295 high Mg-number in spinels from the lherzolite to high Cr-number–low Mg-number in spinels  
296 from harzburgites. Secondary spinels in reaction zones commonly have higher Mg-number  
297 (65.9-82.4) and Cr-number (9.7–45.8) compared with primary spinel, corresponding to the  
298 most chromiferous spinels of the harzburgites (Fig.5, Table 3).

299

#### 300 4.2.1.5 Amphibole

301

302 Amphiboles occur in four xenoliths (SZG30, FT12, FT08P, MSZK1306A, Table 3) and are  
303 pargasites according to the classification of [Locock, \(2014\)](#). Their Mg-numbers range from  
304 88.2 to 89.0 and are similar to those described by [Bali et al. \(2002\)](#) and [Szabó et al. \(2004\)](#).  
305 They are variable in TiO<sub>2</sub> (0.3-2.7 wt. %) and rather rich in Cr<sub>2</sub>O<sub>3</sub> (1.0-1.8 wt. %) and Na<sub>2</sub>O  
306 (2.1-3.7 wt. %). Amphiboles in MSZK1306A have lower TiO<sub>2</sub>, Al<sub>2</sub>O<sub>3</sub> and Na<sub>2</sub>O contents and  
307 higher CaO, SiO<sub>2</sub> and K<sub>2</sub>O contents than resorbed amphiboles in reaction zones (SZG30,  
308 FT12, FT08P).

309

#### 310 4.2.1.6 Carbonates

311

312 Carbonates were analyzed in veins in lherzolite SZG30. They have compositions typical of  
313 Mg-calcites (CaO between 50.7 and 52.6 wt. %) with low FeO (1.61 to 1.99 wt. %), MgO  
314 (4.36 to 5.02 wt. %), MnO (0.31 to 0.51 wt. %) and SiO<sub>2</sub> (0.02 to 0.07 wt. %).

315

316 In summary, primary minerals (Ol, Opx, Cpx, Sp) show the same range of major element  
317 compositions as those published in previous studies for xenoliths from Szentbékállá and  
318 Szigliget ([Downes et al., 1992](#); [Bali et al., 2002](#); [Falus et al., 2004](#); [Demény et al., 2004](#); [Bali  
319 et al., 2007](#); [Szabó et al., 2009](#)) (Fig.4). However, some samples display more fertile  
320 compositions than those from previous studies, as shown by the lower Mg-numbers (e.g.  
321 samples SZB44, SZB50, SZG30, SZG44 and FT12) in olivine (88.8-89.3), orthopyroxene  
322 (89.2-90.0) and clinopyroxene (88.8-90.4). Similar major element compositions of secondary  
323 minerals were previously reported by [Bali et al. \(2008\)](#) in melt pockets from mantle xenoliths  
324 from Szentbékállá (Fig. 5).

325

326 4.2.2 Trace element analyses

327

328 The rare-earth elements (REE) concentrations of mineral phases (clinopyroxene, amphibole)

329 are given in Table 4 and REE and trace element patterns are presented in Figure 6. Trace

330 element contents of clinopyroxenes correspond to cores of primary clinopyroxenes (Cpx I) to

331 avoid potential metasomatic modification.

332 The lherzolites have clinopyroxenes with very variable trace element contents and were

333 subdivided into three groups on the basis of the shape of their REE patterns and on the light

334 REE (LREE)/Heavy REE (HREE) ratios, as follows.

335 Group I. Clinopyroxenes are characterized by low abundances of LREE compared with

336 MREE and HREE (SZB16, SZG14, SZG30, SZG44, MSZK1308, Fig. 6). The lherzolites in

337 which they occur have a protogranular texture (except SZG30). The  $(La/Yb)_N$  (where N

338 indicates primitive mantle normalized) ratios are low and range from 0.2 to 0.8. The

339 multielement patterns display low contents in highly incompatible elements. A slight

340 enrichment in Nb is observed on MSZK1308. There are negative anomalies in Ba, Zr and Ti

341 and a slight Pb negative anomaly in SZB16, SZG30, MSZK1308. The concentration of Sr in

342 this group ranges from 56.9 to 90.0 ppm (Table 4).

343 Group II. Clinopyroxenes from group II are characterized by flat or nearly flat REE patterns

344 (SZB44, SZB50, SZB52). They are found in lherzolites with equigranular mosaic textures

345 (except SZB52). These clinopyroxenes have  $(La/Yb)_N = 0.6-1.3$ ,  $(La/Sm)_N = 0.8-1.0$  and

346  $(Sm/Yb)_N = 0.6-1.5$  with weak negative anomalies in Nb, Zr and Ti and no enrichment in the

347 most incompatible elements (Th and U). The concentration of Sr in this group ranges from

348 21.4 to 71.9 ppm.

349 Group III. Clinopyroxenes from group III are characterized by REE or trace element patterns  
350 showing enrichments in the most incompatible trace elements (SZB51, SZB66, SZG23, FT12,  
351 FT01P, FT08P, MSZK1306A), and therefore high  $(La/Yb)_N$  ratios ranging from 0.7 to 15.7.  
352 Their trace element patterns show enrichments in large ion lithophile elements (LILE Th and  
353 U) and negative anomalies in Ba and high field strength elements (HFSE; Ta, Zr and Ti)  
354 except Nb. The concentration of Sr in group III ranges from 36.9 to 182 ppm. Finally, the  
355 microstructure in group III lherzolites range from protogranular to equigranular mosaic. The  
356 harzburgites have clinopyroxenes with very variable trace element contents and are  
357 characterized by low abundances of HREE and variable MREE and LREE abundances. All  
358 the HREE depleted clinopyroxenes are in the group III (SZB51, SZB66, FT01P, FT08P,  
359 MSZK1306A).

360

361 REE and other trace element patterns of the amphibole in harzburgite MSZK1306A and  
362 FT08P (Fig. 6) are similar to those of clinopyroxene from the same sample (group I).  
363 However, amphiboles in sample MSZK1306A have a higher concentration in most trace  
364 elements such as U, Th and Sr (U 0.1 ppm, Th 0.6 ppm and Sr 107.1-115.6 ppm; in  
365 MSZK1306A and U 3.0-3.4 ppm, Th 13.9-15.3 ppm and Sr 472.9-513.2 ppm in FT08P) than  
366 in the coexisting clinopyroxene (U 0.0 ppm, Th 0.2 ppm and Sr 36.9-39.4 ppm; in  
367 MSZK1306A and U 1.5-2.0 ppm, Th 5.3-7.5 ppm and Sr 121-144 ppm in FT08P), in  
368 agreement with observations in amphibole-bearing xenoliths from Antarctica ([Coltorti et al.,](#)  
369 [2004](#)) and Kapfenstein ([Coltorti et al., 2007](#)).

370

## 371 4.3 Chemistry of the melt phases

372

### 373 4.3.1 Major element analyses



374

375 Glasses show very variable compositions (Table 5, Fig.7) and will be subdivided into three  
376 groups on the basis of their petrographic textures and of their major element contents, as  
377 follows.

378 Group I. The glasses in melt veins. The major element compositions of glass in melt veins are  
379 highly variable both between and within single xenoliths. Overall, they are characterized by  
380 relatively high SiO<sub>2</sub> (55.8-62.7 wt. %) and K<sub>2</sub>O (1.6-5.9 wt. %) and low Na<sub>2</sub>O (3.9–5.7 wt.  
381 %), Al<sub>2</sub>O<sub>3</sub> (17.0-20.4 wt. %), MgO (2.4-4.2 wt. %) and FeO<sub>T</sub> (2.5-4.3 wt. %) contents (Fig.  
382 7).

383 Group II. The glasses in silicate melt inclusions. The major element compositions of glass in  
384 silicate melt inclusions are characterized by relatively high SiO<sub>2</sub> (55.0 wt. %), Na<sub>2</sub>O (7.31 wt.  
385 %), Al<sub>2</sub>O<sub>3</sub> (22.9 wt. %), and low FeO<sub>T</sub> (3.3 wt. %), MgO (2.3 wt. %) and K<sub>2</sub>O (<1.8 wt. %)  
386 contents (Fig. 7).

387 Group III. The glass in melt pockets. The major element compositions of glass in melt pockets  
388 are highly variable both between and within single samples. Overall, they are characterized by  
389 relatively low SiO<sub>2</sub> (50.8-57.2 wt. %), Na<sub>2</sub>O (4.0-5.5 wt. %), high Al<sub>2</sub>O<sub>3</sub> (19.5-23.8 wt. %)  
390 and FeO<sub>T</sub> (3.0-4.9 wt. %) contents (Fig. 7) compared with group I and II.

391

#### 392 4.3.2 Trace element analyses

393

394 The trace element concentrations of glass phases are given in Table 6 and REE and their  
395 patterns are shown in Figure 8. The glasses present very variable trace element contents and  
396 were subdivided into two groups on the basis of their location and their trace element  
397 contents, as follows.

398 Group I. The glass in melt veins and silicate melt inclusions. Glasses are characterized by  
399 REE or other trace element patterns showing enrichments in the most incompatible trace  
400 elements (SZB16, SZB51, SZB52, SZB66, SZG14, FT01P, Fig. 8a) and therefore high  
401 (La/Yb)<sub>N</sub> ratios ranging from 2.6 to 68.5. Glass in melt veins have trace element patterns  
402 similar to glass analyzed by Szabó et al. (2009) in silicate melt inclusions.

403 Group II. The glasses in melt pockets present very variable trace element contents and were  
404 subdivided into two sub-groups on the basis of their trace element contents, as follows.

405 Group IIa. Glasses from group IIa are characterized by flat or nearly flat REE patterns  
406 (SZB44, SZB50, SZG44). These glasses have (La/Yb)<sub>N</sub> = 0.1-1.6, (La/Sm)<sub>N</sub> = 0.1-1.2 and  
407 (Sm/ Yb)<sub>N</sub> = 1.0-1.4 with positive anomalies in Nb, Sr and Ti and a negative anomaly in Zr,  
408 Hf.

409 Group IIb. Glasses from group IIb are characterized by REE or trace element patterns  
410 showing enrichments in the most incompatible trace elements (SZG23, FT12, FT08P), and  
411 therefore high (La/Yb)<sub>N</sub> ratios ranging from 6.2-53.0. Their trace element patterns show  
412 enrichments in LILE (Th and U) and negative anomalies in HFSE (Nb, Ta, Zr and Ti). The  
413 MREE–HREE pattern is almost flat and resembles that of group I or group IIa glasses.  
414 Glasses in melt pockets (Group IIa, IIb, Fig.3) present incompatible element enrichments that  
415 parallel those of the associated amphiboles, and those described in the Pannonian Basin  
416 (Demény et al. 2004; Demény et al. 2005; Bali et al., 2008).

417

#### 418 4.4 Bulk melt pocket compositions

419

420 Bulk compositions of melt pockets have been reconstructed from modal composition and  
421 from the chemistry of the glasses and the secondary mineral phases that compose them. The  
422 results are presented in Table 7 for one sample of Szentbékállá, one of Szigliget and one of

423 Mindszentkállya. The reconstructed bulk compositions of the silicate melt pockets are very  
424 similar to pargasitic amphibole compositions and to the analyzed amphiboles in the respective  
425 locations.

426

#### 427 4.5 Thermobarometry

428

429 Equilibrium temperatures of the studied xenoliths were determined using the ‘Ca-in-opx’ and  
430 ‘opx-cpx’ thermometers of [Brey et al. \(1990\)](#), using a pressure of 1.5 GPa. All xenoliths show  
431 moderate equilibrium temperatures (Szentbékállya: 960-1080°C; Szigliget: 990-1010°C;  
432 Füzes-tó: 960-1090°C; and Mindszentkállya: 930-1030°C). These results are similar to those of  
433 mantle xenoliths published from the same volcanic field (BBHVF) ([Szabó et al., 1995](#); [Bali et al., 2002](#);  
434 [Szabó et al., 2009](#)). The equilibrium temperatures vary with the microstructure of  
435 the xenoliths. Xenoliths with coarse-grained protogranular microstructure record high  
436 equilibrium temperatures (930-1090°C) whereas xenoliths with a mosaic microstructure  
437 record lower equilibrium temperatures (930-993°C), consistent with the recent study of  
438 [Embey-Isztin et al. \(2014\)](#). According to the geotherm of [Kovacs et al. \(2012\)](#), the mantle  
439 section sampled represents depths of 35 to 50 km.

440

#### 441 5 Discussion

442

443 The peridotite xenoliths from the BBVHF record a complex multi-stage partial melting and  
444 metasomatic history, such as demonstrated by [Bali et al. \(2002, 2008\)](#) and [Downes et al. \(1992\)](#).  
445 The following discussion will mostly focus on the origin of the latest metasomatic  
446 imprint in the four xenolith suites. The mineralogical and geochemical evidences for earlier  
447 processes are briefly described below.

448

## 449 5.1 Processes recorded before the late stage metasomatism

450

### 451 5.1.1 Partial melting of the peridotite

452

453 The major element compositions of the primary mineral phases in six protogranular samples  
454 of the suite show high Mg# or Cr# (Ol, Opx, Cpx Sp) associated to a low modal content of  
455 clinopyroxene (4-9 vol.%), low contents of basaltic components in the primary clinopyroxene  
456 and low HREE contents in clinopyroxenes. These mineralogical and geochemical  
457 characteristics indicate that some samples have recorded variable, yet high partial melting  
458 degrees in the lithospheric mantle beneath the Pannonian Basin. Some xenoliths (SZB66,  
459 MSZK1306A, FT01P and FT08P) have low Dy, Er, Yb and Lu contents compared with the  
460 CI-chondrite and primitive mantle estimates (Fig. 6) and have preserved the trace element  
461 signature of partial melting residues. To assess the extent of partial melting, we used the non-  
462 modal fractional partial melting model of [Johnson et al. \(1990\)](#) and [Hellebrand et al. \(2002\)](#) in  
463 the spinel stability field (see supplementary material). Two harzburgites (MSZK1306A and  
464 FT08P) and two lherzolites from Szentbékállá (SZB52 and SZB66) indicate moderate to  
465 high melting degrees of  $\approx 10$ -15%, in accordance with their low cpx modal contents (1.75-9  
466 vol.%) and the low basaltic components of their cpx. The occurrence of peridotites showing  
467 evidence of moderate to high partial melting degree (until 25 %) has been already described in  
468 the BBHVF ([Bali et al. 2002, 2008](#) for Szentbékállá and [Downes et al., 1992](#) for Szigliget  
469 and other locations in the BBHVF).

470 However, there is a discrepancy between mineralogical and geochemical indicators in some  
471 cases. One of the lherzolites (SZB52) and one of the harzburgites (FT08P) show lower melting  
472 degrees of  $\approx 5$ -10% and have low Cr# in spinel (16.7-18.5 wt. %). In case of FT08P this is

473 incompatible with the low cpx modal content of the harzburgite (2.3 vol.%;  $\approx$ 20% melting). In  
474 the SZB52 lherzolite the cpx modal content is very high (18.5 vol.%). Since these samples  
475 show enrichments in the most incompatible elements, their HREE contents may not simply  
476 represent melting residues, but were also likely re-enriched due to metasomatic overprint.  
477 Some protogranular lherzolites (SZB16, SZG14, SZG44, MSZK1308) from Szentbékállá,  
478 Mindszentkállá and Szigliget have fertile compositions with minerals with low Mg# and Cr#,  
479 high modal contents of cpx (12-18 vol.%), high amounts of basaltic components in their cpx  
480 as well as slightly LREE depleted REE patterns. Major and trace element compositions for  
481 these samples are very similar to Primitive Mantle values ([McDonough and Sun, 1995](#)). These  
482 mineralogical and geochemical characteristics suggest that these samples suffered from very  
483 low degrees of melting. Most of these samples also have high HREE compared to those of the  
484 primitive cpx used in the trace element modeling (taken from [Johnson et al., 1990](#)), which  
485 suggest that if these samples melted, the melting degree was low enough (<1%) not to affect  
486 the HREE contents but only the most incompatible LREE.

487

#### 488 5.1.2 Metasomatism

489

490 Metasomatic processes have also affected the xenoliths prior to the formation of melt pockets  
491 and veins. The occurrence of amphibole is widespread in the lithospheric mantle below the  
492 BBHVF ([Bali et al. 2002, 2008](#)) and has been interpreted as a crystallization from volatile-  
493 bearing silicate melt possibly linked to the percolation of subduction zone melts during the  
494 Miocene. The trace element patterns in primary clinopyroxenes from most xenoliths  
495 (lherzolites and harburgites) also show enrichments in the most incompatible elements (Th, U,  
496 Ba, LREE) that were acquired during metasomatism. Lherzolites SZB51, SZG23, FT12,  
497 FT08P have clinopyroxenes with selective enrichments in Th, U, LREE and depletions in

498 HFSE. The gradual enrichments in the most incompatible elements can result from  
499 metasomatic imprint during chromatographic-like effects produced during interaction  
500 between the host peridotite and small melt fractions of a silicate melt enriched in trace  
501 elements (Bodinier et al., 1990). These trace elements characteristics in clinopyroxenes have  
502 also been interpreted as resulting from metasomatism by carbonate-rich melts below the  
503 BBHVF (Embey-Isztin et al., 2014). These enrichments are mostly seen in lherzolites with a  
504 mosaic microstructure that equilibrated at shallow depth below the MOHO (~30 km, Posgay  
505 et al. 1995). The metasomatic overprint is also more pronounced in clinopyroxenes from  
506 harzburgites with enrichments in MREE and HREE, a characteristic feature of SZB51,  
507 SZB66, MSZK1306A and FT01P.

508

## 509 5.2 Late stage metasomatism

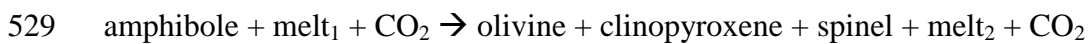
510

511 Textural observations in the studied BBHVF xenoliths indicate that trails of secondary fluid  
512 inclusions, glass veins and glass pockets form a common network of melt circulation (Fig. 3d,  
513 Creon et al., this volume). Moreover, as shown by Creon et al. (this volume), vesicles trapped  
514 in melt veins and melt pockets and FIs are composed almost exclusively of CO<sub>2</sub>. The CO<sub>2</sub>-  
515 rich character of percolating melts has previously been highlighted by the observation of  
516 carbonates in veins and melt pockets in some xenoliths of the BBHVF (Embey-Isztin and  
517 Scharbert, 2001; Bali et al., 2002; Demény et al., 2004; Demény et al., 2010). However, only  
518 few carbonates were recognized in this study (SZG30). Seven xenoliths from three locations  
519 (SZB44, SZB50, SZB51, SZG23, SZG44, FT12, FT08P; Table 1) display the development of  
520 reaction zones at the expense of amphibole (Fig. 3g, h). The others (SZB16, SZB52, SZB66,  
521 SZG14, SZG30, FT01P, MSZK 1306A, MSZK1308, Table 1) display glass in veins between

522 primary minerals, commonly associated with newly formed minerals (olivine, clinopyroxene  
523 and spinel) that have higher Mg# than the primary minerals (Fig. 9).

524 The amphibole-bearing harzburgite FT08P probably illustrates a primordial stage for melt  
525 pocket formation. The textural features in FT08P (Fig. 9) indicate that a melt was formed by  
526 incongruent breakdown of amphibole, due to heating or infiltration of a melt/fluid in the  
527 xenolith, according to the following reaction (Ban et al., 2005):

528



530

531 In other xenoliths (SZB44, SZB50, SZB51, SZG23, SZG44), the melt pockets only displays  
532 gl+ol+cpx+sp+CO<sub>2</sub> but no relict amphibole. This observation suggests that amphibole may  
533 locally have fully reacted and broken down. These melt pockets are similar to those described  
534 by Bali et al. (2008) for lherzolites and websterites from Szentbékállá and Szigliget or by  
535 Embey-Isztin & Scharbert (2001). The occurrence of large empty vesicles also indicates that a  
536 gas phase formed at some stage during in-situ partial melting of the amphibole or was rather  
537 inherited from a CO<sub>2</sub>-supersaturated metasomatic agent. This idea is in agreement with the  
538 measured high abundance of dissolved volatiles in the trapped glass (veins and melt pockets)  
539 which are up to 4.25 ± 0.27 wt. % H<sub>2</sub>O and 0.96 ± 0.02 wt. % CO<sub>2</sub> (Creon et al., this volume),  
540 corresponding to CO<sub>2</sub>-saturated melt at lithospheric conditions (0.69 to 1.78 GPa).

541 The glass in the melt pockets has variable major element compositions and vary from basaltic  
542 andesitic or basaltic trachy-andesitic to andesitic-trachyte in composition (53.7-58.4 wt. %  
543 SiO<sub>2</sub>). The glass in veins has a comparably more silicic composition and is typically trachy-  
544 andesitic (57.1-62.1 wt. % SiO<sub>2</sub>). The glass in veins are also more homogeneous at the scale  
545 of the sample than the glass in melt pockets. Such variable major element compositions are  
546 frequent in glass from mantle xenoliths worldwide (e.g. Wulff-Pedersen et al., 1999; Coltorti

547 [et al., 2000](#)). [Wulff-Pedersen et al. \(1999\)](#) interpreted silicic glasses as cogenetic melts  
548 derived by infiltration-reaction-crystallization (IRC) processes ([Vannucci et al., 1998](#)), with  
549 the (highly) silicic melts being derived by percolation-reaction-crystallization mechanisms  
550 during metasomatism by an infiltrating silicate melt (host basalt) and preferential reaction  
551 with orthopyroxene. However, similar melt compositions in the BBHVF xenoliths have been  
552 attributed by several authors (e.g. [Bali et al., 2007](#); [Bali et al., 2008a,b](#)) to metasomatic  
553 imprints unrelated to the alkali host basalts. These authors proposed that melt pockets have  
554 formed by the breakdown of former amphibole due to the introduction of a metasomatic melt  
555 ([Bali et al., 2007](#)). In the following sections, the origin of melt veins and pockets will be  
556 addressed based on geochemical and petrographic grounds.

557

#### 558 5.2.1 Glass in the melt pockets

559

560 Compared with the literature data on glass from xenoliths from the BBHVF, the glass in the  
561 melt pockets analyzed in this study resembles the compositional spectrum of glasses  
562 documented in [Bali et al. \(2002\)](#) for similar melt pockets in peridotites and pyroxenites from  
563 Szentbékállá (samples from SZB group, Fig.7). The SMI in pyroxenes from spinel-  
564 lherzolites from Szigliget ([Szabó et al., 2009](#)) have comparable SiO<sub>2</sub> (54.2 wt. %) and other  
565 major elements (Al, Ca, Na) than in the glass analyzed in the melt pockets but have lower  
566 MgO, FeO and higher K<sub>2</sub>O contents (5.3 wt. %). The glass in melt pockets is very different in  
567 composition from the SMI reported by [Bali et al. \(2008\)](#) from Szigliget since the latter is Si-  
568 rich (57.3-74.0 wt. %) and has always low MgO (0-0.88 wt. %), FeO (0.44-3.57 wt. %) and  
569 CaO (0.69-3.06 wt. %). Most of the glass in melt pockets has lower contents of the most  
570 incompatible elements than alkali basalts ([Embey-isztin et al., 1993](#)) and also than calc-alkali  
571 volcanics ([Harangi and Lenkey, 2007](#)) in the area for similar SiO<sub>2</sub> contents (50.5-77.9 wt. %).



572 Some of the major element variations in glasses in veins and melt pockets could be consistent  
573 with a fractional crystallization process (e.g. SiO<sub>2</sub>, MgO, CaO, FeO; Fig.7). The possible  
574 cogenetic relationship between glass in veins and less silicic melt pockets was tested using  
575 crystal fractionation modeling of olivine, clinopyroxene and spinel from a parental melt in the  
576 reaction zones using the rhyolite-MELTS software (Gualda et al., 2012; Ghiorso and Gualda,  
577 2015) including the H<sub>2</sub>O and CO<sub>2</sub> contents of the melts. The starting compositions were taken  
578 from the most primitive composition measured for SZG44 glass. The crystal fractionation  
579 (CF) calculations for a crystallizing assemblage of 0.1% ol + 84.4% cpx + 15.6% sp at 970°C  
580 and 1.2 GPa fit well some major elements in glass from veins (CaO, MgO, FeO) for about  
581 30% FC (Fig. 7). However, the model fails to explain the high K<sub>2</sub>O and the low Na<sub>2</sub>O and  
582 Al<sub>2</sub>O<sub>3</sub> concentrations of the glass in veins. Trace elements contents of the Si-rich glass in  
583 veins also argue against a cogenetic relationship with melt pockets by crystal fractionation  
584 (Fig. 8). For example, the glass in the melt pockets and in the veins that have similar SiO<sub>2</sub>%  
585 display contrasting trace element patterns, one being smoothly enriched in the most  
586 incompatible elements (veins) and one displaying a rather flat distribution of trace elements  
587 with some pronounced “negative” anomalies in HFSE (Fig. 8). The absence of negative HFSE  
588 anomalies in the glass from veins is difficult to reconcile with an origin by simple crystal  
589 fractionation process of an assemblage of ol+cpx+sp from a glass in melt pockets that display  
590 negative/positive anomalies of these elements (Nb, Ta, Zr, Hf, Sr, Pb). We conclude that the  
591 glass in veins does not in most cases evolve from the glass in melt pockets due to simple  
592 fractional crystallization of secondary ol+cpx+sp.

593 We suggest that the glass in veins represents a CO<sub>2</sub> (-H<sub>2</sub>O) rich Si-rich melt, that infiltrated  
594 the xenoliths and triggered melting of interstitial amphibole to form the secondary melt  
595 pockets. This interpretation is supported by the very similar trace element patterns in some  
596 glasses from melt pockets and coexisting resorbing amphibole (Fig. 10). The compositional

597 spectrum of hybrid melts resulting from assimilation of amphibole into Si- and trace element-  
598 rich melt such as that occurring in some veins is shown in Figure 10. The close resemblance  
599 of hybrid melts with the glass in melt pockets suggests that the incongruent melting of  
600 amphibole buffered most of the trace element contents of the glass in melt pockets, except the  
601 HREE budget. For instance, sample FT08P has glasses with trace element compositions very  
602 similar to the resorbed amphibole (Fig. 10). Furthermore, the calculated bulk major element  
603 compositions of the melt pockets by inverting the fractional crystallization of  
604 OIII+CpxII+SpII in the pockets are fairly similar to that of the amphibole in the xenoliths  
605 (this study, Table 7; [Bali et al., 2008](#)). Therefore, the glass in melt pockets is believed to result  
606 from incongruent melting of amphibole, triggered by the influx of a hot CO<sub>2</sub>-rich silica-rich  
607 melt into the peridotites (similar to the glass in veins), and subsequent CF of newly formed  
608 OIII, CpxII and SpII. This metasomatic agent was defined as a CO<sub>2</sub> or aqueous-rich fluid  
609 enriched in LILE or as a LREE-enriched silicate melt. The Sr-Nd-Pb isotopic data on glass in  
610 similar melt pockets from other SZB xenoliths ([Bali et al., 2002](#)) are not consistent with those  
611 of the host Pliocene and Quaternary alkali basalts but rather support a melt source containing  
612 a slab-derived component, that may have reacted with the upper lithospheric mantle during  
613 percolation. This study further demonstrates that the metasomatic agent was likely Si-rich,  
614 and enriched in LILE, HFSE, LREE, and had high volatile contents such as H<sub>2</sub>O and CO<sub>2</sub>  
615 ([Creon et al., this volume](#)).

616 The geothermometer of [Putirka \(2008\)](#) has been used on clinopyroxeneII-glass pairs that  
617 show evidence for chemical equilibrium to estimate the temperature of clinopyroxene-melt  
618 equilibration in the melt pockets. Calculated temperatures (Szentbékállá: 1,210-1,250°C;  
619 Szigliget: 1,230-1,270°C; Füzes-tó: 1,220°C; Table 8) represent minimum temperatures for  
620 the formation of melt pockets. Similar calculations for clinopyroxenes in melt pocket in other  
621 xenoliths from the Szentbékállá locality yield similar temperatures (1110 to 1200°C from

622 [Demény et al. \(2004\)](#) and [Bali et al. \(2008\)](#)). This range is 150–350°C higher than the  
623 estimated equilibrium temperatures of the host peridotites and pyroxenites (Table 8). These  
624 temperature estimates suggest that the studied melt pockets formed at higher temperatures  
625 than equilibrium temperatures recorded by the primary mantle minerals, likely induced by hot  
626 Si-rich magma injection. Pressure estimates based on [Putirka \(2008\)](#) indicate a minimum  
627 pressure for melt pocket formation of 0.7-0.8 GPa for Szentbékállá, 1.0-1.1 GPa for  
628 Szigliget and 0.8-1.0 GPa for Füzes-tó, corresponding to depths of 28–38 km (Fig. 11). Figure  
629 11 shows the comparison of the pressures determined from primary mineral chemical  
630 equilibrium (M-I), fluid inclusions trapping pressures (FI), vesicles pressure at the last melt-  
631 fluid equilibrium (CO<sub>2</sub>-melt; [Creon et al., this volume](#)) and newly formed minerals chemical  
632 equilibrium in melt pockets (M-II). The figure 11 illustrates in Szentbékállá samples that  
633 vesicles, fluid inclusions and secondary crystallization of melt pockets happened almost at the  
634 same pressure, at about ~0.8 GPa. In Szigliget samples, vesiculation and secondary  
635 crystallization of melt pockets took place at the same pressure close to the MOHO (~1.0  
636 GPa). However fluid inclusions trapping seems to have happened at shallower depths (~0.5  
637 GPa), a result likely biased by fluid inclusions decrepitation ([Creon et al., this volume](#)). In  
638 Füzes-tó samples, secondary crystallization of melt pockets and fluid inclusions show the  
639 same pressure close to the MOHO (~0.9 GPa), whereas vesicles have lower pressure (~0.6  
640 GPa), which can be the result of a late melt-fluid equilibrium before the melt quenching. The  
641 P-T conditions estimated for mineral-melt equilibrium in the melt pockets show that the melt  
642 pockets formed in the upper part of the lithosphere, close to the MOHO, and that this occurred  
643 outside the stability field of amphibole-bearing peridotite due to an increase in temperature  
644 after melt injection ([Olafsson and Eggler, 1983](#); [Niida and Green, 1999](#)).

645

646 5.2.2 Glass in veins

647

648 The glass in the veins has variable but high SiO<sub>2</sub> contents (54.2 to 62.7 wt. %). The lowest  
649 silica-rich glass in veins (SZB16, SZB52) has a composition similar to the richest silica glass  
650 in melt pockets (55.8-59.0 wt. %). According to petrographic observations, there is only little  
651 evidence for reaction between primary minerals (CpxI and SpI) and the interstitial glass in  
652 veins. Figure 12 evidences that the melt in veins cannot be associated to in-situ melting of  
653 peridotites (Draper and Green, 1997). This observation suggests that the Si-rich glass was in  
654 close equilibrium with the host spinel peridotites in which they are found.

655 The glass in veins has high SiO<sub>2</sub>, MgO and K<sub>2</sub>O contents and has trace element contents  
656 enriched in the most incompatible elements, showing variable Pb negative/positive and Sr  
657 positive anomalies but no relative depletion in HFSE (Fig. 13). The Si-rich glass in veins has  
658 different major element compositions compared to the Pliocene alkali basalts and calc-alkali  
659 volcanics (Fig. 12) and show differentiated compositions in terms of major elements. The  
660 glass in veins also display different trace element abundances or ratios than the more mafic  
661 alkali basalts and calc-alkali volcanics from the Pannonian Basin (Fig. 13).

662 They also do not display the typical geochemical characteristics of worldwide calc-alkali  
663 magmas as seen in most pannonian calc-alkali volcanics (ie. high Ba/Nb, negative anomalies  
664 in HFSE) but it resembles some of the calc-alkali volcanics of the Pannonian Basin (Fig. 13  
665 and 15), especially from the Northern Pannonian Basin (NPB, 17-10 Ma, Harangi and  
666 Lenkey, 2007). They are however distinctive given their higher Nb and Ti and lower HREE  
667 contents (Fig. 13) but also their higher SiO<sub>2</sub> and Na<sub>2</sub>O and lower FeO, CaO than the NPB  
668 (Fig. 12).

669 The occurrence of Si-rich melts as efficient metasomatic agents and their interaction with the  
670 lithospheric mantle beneath the BBHVF has already been documented by Bali et al. (2007,  
671 2008a, 2008b) for xenoliths from Szentbékállá and Szigliget (samples SZB and SZG) and

672 was also documented by [Coltorti et al. \(2007\)](#) for mantle xenoliths from the Kapfenstein  
673 (Austria). In the BBHVF, there are mineralogical and geochemical evidences that the  
674 lithospheric mantle was modified by percolation of Si-saturated melts. The occurrence of opx-  
675 rich lithologies in peridotites as well as of Qz-bearing websterite veins/bands were interpreted  
676 as resulting from the interaction between melts/fluids derived from subducted slab ([Bali et al.,](#)  
677 [2008](#)) and the lithospheric mantle beneath the BBHVF. In the BBHVF, the silica richest glass  
678 (54.2-62.7 wt. % SiO<sub>2</sub>) occurs as primary silicate melt inclusions in pyroxenes (opx, cpx) as  
679 well as interstitial glass in veins in pyroxenes-rich xenoliths (Qz-bearing websterite,  
680 clinopyroxenite) or in peridotites (lherzolites, harzburgites) from Szigliget ([Bali et al., 2008](#)).  
681 However, these primary SMI have lower MgO, CaO and much higher K<sub>2</sub>O for 57.3-80.2 wt.  
682 % SiO<sub>2</sub> compared to the glass in veins (54.2-62.7 wt. % SiO<sub>2</sub>). Of particular interest, the  
683 interstitial glass in veins reported by [Bali et al. \(2008\)](#) in the Qz-bearing websterite is much  
684 more silicic (63.8-80.5 wt. % SiO<sub>2</sub>) and more depleted in terms of most major elements  
685 except K<sub>2</sub>O. In terms of trace elements, the SMI in opx and cpx from [Bali et al. \(2008\)](#) have  
686 quite similar LREE, MREE ( $\pm$ HREE) but they have higher Th, U contents and pronounced  
687 negatives anomalies in Nb, Ta, Sr.

688 [Bali et al., \(2008\)](#) described several features of the trace element composition which resemble  
689 those of adakites in silicate melt inclusions of Szentbékállá and Szigliget. Oppositely, the  
690 low Sr content of the silicate melt inclusions (74-116 ppm) and high K/Na ratios, and large  
691 ion lithophile element (LILE) and LREE concentrations are not typical for adakites (4400  
692 ppm Sr). These features were interpreted as resulting from (1) the presence of a mineral phase  
693 that retains Sr in the source during slab melt generation, (2) incompatible trace elements of  
694 the source and (3) small degrees of partial melting. In this study, several characteristics of the  
695 major and trace element compositions of the glass in veins also resemble those of adakites,  
696 especially the low-Si adakites as illustrated in Figures 12 and 14. For instance, the Si-rich

697 glasses have high MgO and CaO, high La/Yb at low Yb contents, high Sr/Y at low Y contents  
698 (Fig. 14). However, as demonstrated for the lithospheric mantle beneath the BBHVF (Bali et  
699 al. 2008), the silicic melts derived from subduction zones have probably reacted within the  
700 lithospheric mantle before being trapped as SMI or silicate melt pockets in the host peridotites  
701 so it is unlikely that they have preserved their original geochemical signature.  
702 Rapp et al. (1999) showed in their experiments a range of melts produced by assimilation of  
703 peridotite by adakitic melts in order to understand the geochemical changes during migration  
704 of melts in the mantle wedge. Some of the vein glasses have major element compositions  
705 close to the composition obtained by assimilation experiments in Rapp et al. (1999) (MgO,  
706 Na<sub>2</sub>O, K<sub>2</sub>O). However CaO and Al<sub>2</sub>O<sub>3</sub> are much higher in the glass in veins than in the  
707 experiments (Fig. 12). The trace elements of the glass in veins are also comparable in terms of  
708 REE+Y, U, Rb, Ba from the assimilation experiments, but have higher Th, Nb and do not  
709 display a relative enrichment in Sr. The high HFSE contents observed in the glass in veins  
710 could be a geochemical characteristic of high-Nb basalts that are found associated with  
711 adakites in subduction zones (Defant and Kepezhinskas, 2001), such as the in Northern  
712 Pannonian Basin found in the area (Harangi and Lenkey, 2007). The experiments of Xiong et  
713 al. (2005) and those of Foley et al. (2000) show that rutile dominates Nb and Ta budgets  
714 during the partial melting of subducted oceanic crust and only rutile is able to cause strong  
715 fractionation of Nb and Ta from other trace elements to produce a negative Nb–Ta anomaly in  
716 the derived liquid (see next section). The absence of negative anomaly in Nb-Ta imply  
717 therefore the absence of rutile as a stable phase during melting in the source region of these  
718 melts and during interaction with the lithospheric mantle.  
719 The trace elements in the glass in veins could allow to place some constraints on the P-T  
720 conditions of the formation of the adakitic melts. The low HREE contents (La/Yb > 20) and Y  
721 (< 18 ppm) suggests the presence of garnet in the source region (Castillo et al., 1999; Defant

722 and Kepezhinskas, 2001). The high abundance of  $K_2O$  in the melts also suggests a substantial  
723 contribution of phlogopite. In figure 15, the postulated melt source is located below the  
724 lithosphere-asthenosphere boundary (LAB, ~2.2GPa, Tašárová et al., 2009) above the  
725 Pannonian Basin (1000-1200°C and 2.2-3 GPa, Fig. 15). These estimations are higher than  
726 those of Bali et al., (2008) for the melt source (950-1050°C and 1.5-2 GPa), which were  
727 determined using silicate melt pockets modified by amphibole assimilation. Our estimation is  
728 based on melt compositions unmodified by amphibole assimilation, and are thus more  
729 representative of the source of the metasomatic agent.

730

### 731 5.3 Melt generation and migration in the Carpathian-Pannonian mantle

732

733 In the Figure 15a, the different P-T conditions determined using geochemical thermo-  
734 barometers of the different magma genesis events are shown together with mineral phase  
735 stability fields. The metasomatic agent was generated along a subduction geotherm, in contact  
736 with hotter asthenospheric mantle between 2-3 GPa. The metasomatic agent migrated from its  
737 source region to the primary lithospheric mantle mineral equilibrium area ( $M_I$ ), which we  
738 locate on the geotherm postulated by Kovacs et al. (2012) to react with the amphiboles and  
739 form SMPs. Melt-mineral equilibrium compositions in SMPs ( $M_{II}$ ) recorded minimum  
740 pressure/temperature conditions near present day Moho depths. The  $M_{II}$  P-T region is located  
741 in the plagioclase equilibrium field, which is contradiction with our observations. We suggest  
742 that the minimum pressures estimated with the method of Putirka are underestimating true  
743 melt generation pressures which were more likely in the spinel stability field, at above 1.2-1.3  
744 GPa, within the pressure range of primary mineral equilibrium ( $M_I$ ). The  $M_{II}$  area is located  
745 within the carbonate equilibrium field; which does not satisfy our observations and those of  
746 the literature (Bali et al., 2002; Demény et al., 2004; Demény et al., 2010) which illustrate the

747 presence of free CO<sub>2</sub> and potentially carbonates in the mantle xenoliths. We do not explain  
748 this discrepancy between known thermodynamic phase equilibrium and our observations. The  
749 determination of carbon phase stability is beyond the scope of this work and will not be  
750 discussed further here.

751 The Si-rich melts percolating the lithospheric mantle of the BBHVF have strong affinities  
752 with high-Nb adakites and are associated with subduction zone fluids. The high CO<sub>2</sub> and H<sub>2</sub>O  
753 contents of Si-rich melts (Creon et al., this volume) are in favor of a hydrated and carbonated  
754 pyrolith. Altered oceanic lithosphere and/or sediment melting are best candidates for  
755 providing a significant carbon and hydrogen budget (Staudigel et al., 1989; Plank and  
756 Langmuir, 1998) to subduction melts. Dehydration and decarbonation of eclogites and  
757 metasediments on the subduction geotherm at pressures above 3 GPa liberated volatile and  
758 incompatible element-rich fluids that migrated towards the metasomatized mantle wedge (Fig.  
759 15). The percolation of these primary fluids destabilized phlogopite and amphibole rich  
760 peridotites to generate CO<sub>2</sub>-supersaturated Nb-rich silicic melts that rapidly reached  
761 asthenospheric temperatures. The injection of such hot Si-rich melts in the lithospheric mantle  
762 in turn triggered the fusion of pargasite due to increased temperatures within the spinel  
763 stability field. Amphibole melts of initial basaltic compositions fractionated into olivine,  
764 clinopyroxene, spinel and andesitic melts before the system quenched on its way up to the  
765 surface.

766

## 767 6 Conclusion

768

769 Compositional and textural features of fifteen ultramafic mantle xenoliths from four different  
770 localities (Szentbékállá, Szigliget, Füzes-tó and Mindszentkállá) have been studied. They  
771 contain trails of secondary fluid inclusions, primary silicate melt inclusions, veins and pockets



772 of melts which allow reconstructing different stages of partial melting and metasomatism in  
773 the lithospheric mantle:

- 774 1. The lithospheric mantle below the Pannonian Basin is highly heterogeneous and has  
775 recorded a history of high to low partial fusion events overprinted by cryptic and  
776 modal metasomatism involving the formation of widespread pargasitic amphiboles.
- 777 2. The melting of a CO<sub>2</sub>-rich subducting slab derived source produced high-Nb silicic  
778 melts of adakitic affinity. Melting conditions were comprised at temperatures between  
779 1000-1200°C and pressures between 2 and 3 GPa, near the lithosphere-asthenosphere  
780 boundary. This silicic melt is found in mantle xenoliths as a network of glass veins  
781 enclosing large CO<sub>2</sub> vesicles.
- 782 3. The silicic melt migrated into the lithospheric mantle and interacted with pargasitic  
783 amphiboles. The melting of amphiboles was triggered by temperature increase due to  
784 magma injection and the high CO<sub>2</sub> abundances in melts. The P-T conditions for  
785 melting and crystal fractionation of amphibole melt pockets were of 0.7-1.1 GPa and  
786 1200 °C, near the Moho transition. The melt pockets are found in mantle peridotites as  
787 an assemblages of andesitic glass, CO<sub>2</sub>-vesicles and secondary olivine, clinopyroxene  
788 and spinel. Pargasite melts could be the parental magmas of the calc-alkaline suite of  
789 the Pannonian Basin.

790

## 791 7 Acknowledgements

792

793 This project was funded by IFP Energies nouvelles. Thank you to Csaba Szabó for his  
794 kindness help in the field and in the study of these mantle xenoliths. Herman Ravalajaona is  
795 acknowledged for his assistance during sample and thin section preparation. We are grateful  
796 to Carole La for her efficient help in LA-ICP-MS analyses of trace elements at LPG Nantes.

797 Michel Fialin and Nicolas Rividi of the centre CAMPARIS at UPMC assisted for EPMA.

798

799 8 References

800

801 Achterberg V., E., Ryan C. G., Jackson S. E. and Griffin W. (2001) Data reduction software

802 for LA-ICP-MS. In: Sylvester, P. (ed.) *Laser Ablation ICPMS in Earth Science:*

803 *Principles and Applications. Mineral. Assoc. Canada* **29**, 239–243.

804 Bada G., Hovath F., Gerner P. and Fejes I. (1999) Review of the present day geodynamics of

805 the Pannonian Basin progress and problems. *Geodynamics* **27**, 501–527.

806 Bali E., Falus G., Szabó C., Peate D. W., Hidas K., Török K. and Ntaflou T. (2007) Remnants

807 of boninitic melts in the upper mantle beneath the central Pannonian Basin? *Mineral.*

808 *Petrol.* **90**, 51–72. Available at: <http://link.springer.com/10.1007/s00710-006-0167-z>

809 [Accessed January 25, 2014].

810 Bali E., Szabó C., Vaselli O. and Torok K. (2002) Significance of silicate melt pockets in

811 upper mantle xenoliths from the Bakony – Balaton Highland Volcanic Field , Western

812 Hungary. *Lithos* **61**, 79–102.

813 Bali E., Zajacs Z., Kovacs I., Szabó C., Halter W., Vaselli O., Torok K. and Bodnar R. J.

814 (2008) A Quartz-bearing Orthopyroxene-rich Websterite Xenolith from the Pannonian

815 Basin , Western Hungary : Evidence for Release of Quartz-saturated Melts from a

816 Subducted Slab. *J. Petrol.* **49**, 421–439.

817 Bali E., Zanetti A., Szabó C., Peate D. W. and Waight T. E. (2008) A micro-scale

818 investigation of melt production and extraction in the upper mantle based on silicate melt

819 pockets in ultramafic xenoliths from the Bakony–Balaton Highland Volcanic Field

820 (Western Hungary). *Contrib. to Mineral. Petrol.* **155**, 165–179. Available at:

821 <http://link.springer.com/10.1007/s00410-007-0234-4> [Accessed January 25, 2014].

- 822 Balogh K. and Németh K. (2005) Evidence for the Neogene small-volume intracontinental  
823 volcanism in Western Hungary: K/Ar geochronology of the Tihany Maar Volcanic  
824 Complex. *Geol. Carpathica* **56**, 91–99.
- 825 Balogh K. and Pécskay Z. (2001) K/Ar and Ar/Ar geochronological studies in the Pannonian-  
826 Carpathians-Dinarides (PANCARDI) region. *Acta Geol. Hung.* **44**, 281–299.
- 827 Ban M., Witt-Eickschen G., Klein M. and Seck H. a. (2005) The origin of glasses in hydrous  
828 mantle xenoliths from the West Eifel, Germany: Incongruent break down of amphibole.  
829 *Contrib. to Mineral. Petrol.* **148**, 511–523.
- 830 Beccaluva L., Bonadiman C., Coltorti M., Salvini L. and Siena F. (2001) Depletion Events,  
831 Nature of Metasomatizing Agent and Timing of Enrichment Processes in Lithospheric  
832 Mantle Xenoliths from the Veneto Volcanic Province. *J. Petrol.* **42**, 173–187.
- 833 Bodinier J. ., Vasseur G., Vernieres J. and Dupuy C. F. (1990) Mechanisms of mantle  
834 metasomatism: geochemical evidence from the Lherz orogenic peridotite. *J. Petrol.* **31**,  
835 597–628.
- 836 Brey G. P., Kohler T. and Nickel K. G. (1990) Geothermobarometry in Four-phase  
837 Lherzolites I . Experimental Results from 10 to 60 kb. *J. Petrol.* **31**, 1313–1352.
- 838 Castillo P. R., Janney P. E. and Solidum R. U. (1999) Petrology and geochemistry of  
839 Camiguin Island, southern Philippines: insights to the source of adakites and other lavas  
840 in a complex arc setting. *Contrib. to Mineral. Petrol.* **134**, 33–51.
- 841 Coltorti M., Beccaluva L., Bonadiman C., Faccini B., Ntaflos T. and Siena F. (2004)  
842 Amphibole genesis via metasomatic reaction with clinopyroxene in mantle xenoliths  
843 from Victoria Land, Antarctica. *Lithos* **75**, 115–139.
- 844 Coltorti M., Beccaluva L., Bonadiman C., Salvini L. and Siena F. (2000) Glasses in mantle  
845 xenoliths as geochemical indicators of metasomatic agents. *Earth Planet. Sci. Lett.* **183**,  
846 303–320. Available at: <http://linkinghub.elsevier.com/retrieve/pii/S0012821X00002740>.

847 Coltorti M., Bonadiman C., Faccini B., Ntaflos T. and Siena F. (2007) Slab melt and  
848 intraplate metasomatism in Kapfenstein mantle xenoliths (Styrian Basin, Austria). *Lithos*  
849 **94**, 66–89.

850 Coltorti M., Bonadiman C., Hinton R. W., Siena F. and Upton B. G. J. (1999) Carbonatite  
851 Metasomatism of the Oceanic Upper Mantle : Evidence from Clinopyroxenes and  
852 Glasses in Ultramafic Xenoliths of Grande Comore , Indian Ocean. *J. Petrol.* **40**, 133–  
853 165.

854 Creon L., Rouchon V., Youssef S., Rosenberg E., Delpéch G., Guyot F., Szabó C., Tafforeau  
855 P., Boller E., Asimow P. D., Antoshechkina P. M. and Ghiorso M. S. Highly CO<sub>2</sub>-  
856 supersaturated melts in the Pannonian lithospheric mantle – A transient carbon reservoir?  
857 *this Vol.*

858 Csontos L., Nagymarosy A., Horváth F. and Kovác M. (1992) Tertiary evolution of the Intra-  
859 Carpathian area: a model. *Tectonophysics* **208**, 221–241.

860 Dawson J. (1984) Contrasting types of upper-mantle metasomatism? In: Kornprobst J (ed)  
861 Kimberlites II: The mantle and crust– mantle relationships. *Holland*, 289.

862 Defant M. J. and Kepezhinskas P. (2001) Evidence suggests slab melting in arc magmas. *Eos*,  
863 *Trans. Am. Geophys. Union* **83**, 256.

864 Delpéch G., Grégoire M., O’Reilly S. Y., Cottin J. Y., Moine B., Michon G. and Giret a.  
865 (2004) Feldspar from carbonate-rich silicate metasomatism in the shallow oceanic  
866 mantle under Kerguelen Islands (South Indian Ocean). *Lithos* **75**, 209–237.

867 Demény A., Dallai L., Frezzotti M.-L., Vennemann T. W., Embey-Isztin A., Dobosi G. and  
868 Nagy G. (2010) Origin of CO<sub>2</sub> and carbonate veins in mantle-derived xenoliths in the  
869 Pannonian Basin. *Lithos* **117**, 172–182. Available at:  
870 <http://linkinghub.elsevier.com/retrieve/pii/S0024493710000575> [Accessed December 7,  
871 2012].

872 Demény A., Vennemann T. ., Hegner E., Nagy G., Milton J. ., Embey-Isztin A., Homonnay Z.  
873 and Dobosi G. (2004) Trace element and C–O–Sr–Nd isotope evidence for subduction-  
874 related carbonate–silicate melts in mantle xenoliths (Pannonian Basin, Hungary). *Lithos*  
875 **75**, 89–113. Available at:  
876 <http://www.sciencedirect.com/science/article/pii/S0024493704000209> [Accessed March  
877 16, 2015].

878 Demény A., Vennemann T. W., Homonnay Z. and Milton A. (2005) Origin of amphibole  
879 megacrysts in the Pliocene-Pleistocene basalts of the Carpathian-Pannonian region. *Geol.*  
880 *Carpathica* **56**, 179–189.

881 Downes H., Embey-Isztin A. and Thirlwall M. F. F. . (1992) Petrology and geochemistry of  
882 spinel peridotite xenoliths from the western Pannonian Basin (Hungary): evidence for an  
883 association between enrichment and texture in the upper mantle. *Contrib. Mineral.*  
884 *Petrol.* **109**, 340–354.

885 Draper D. S. and Green T. H. (1997) P – T Phase Relations of Silicic , Alkaline , Aluminous  
886 Mantle-Xenolith Glasses Under Anhydrous and C – O – H Fluid-saturated Conditions. *J.*  
887 *Petrol.* **38**, 1187–1224.

888 Embey-Isztin a, Dobosi G., Altherr R. and Meyer H.-P. (2001) Thermal evolution of the  
889 lithosphere beneath the western Pannonian Basin: evidence from deep-seated xenoliths.  
890 *Tectonophysics* **331**, 285–306. Available at:  
891 <http://linkinghub.elsevier.com/retrieve/pii/S0040195100002870>.

892 Embey-Isztin A., Dobosi G., Bodinier J.-L., Bosch D., Jenner G. a., Pourtales S. and Bruguier  
893 O. (2014) Origin and significance of poikilitic and mosaic peridotite xenoliths in the  
894 western Pannonian Basin: geochemical and petrological evidences. *Contrib. to Mineral.*  
895 *Petrol.* **168**, 1054. Available at: <http://link.springer.com/10.1007/s00410-014-1054-y>.

896 Embey-Isztin A., Dobosi G., James D., Downes H., Poultidis C. and Scharbert H. G. (1993) A

897 compilation of new major, trace element and isotope geochemical analyses of the young  
898 alkali basalts from the Pannonian Basin. *Fragm. Mineral. Palaeontol.* **16**, 5–26.

899 Embey-isztin A., Downes H., James D. E. E., Upton B. G. J. G. J., Dobosi G., Ingram G. A.  
900 a., Harmon R. S. S. and Scharbert H. G. G. (1993) The petrogenesis of Pliocene alkaline  
901 volcanic rocks from the Pannonian Basin, Eastern central Europe. *J. Petrol.* **34**, 317–343.

902 Embey-Isztin A. and Scharbert H. G. (2001) Glasses in peridotite xenoliths from the western  
903 Pannonian Basin. *Per. Mineral.* **70**, 359–376.

904 Embey-Isztin A., Scharbert H. G., Dietrich H. and Poultidis H. (1989) Petrology and  
905 geochemistry of peridotite xenoliths in alkali basalts from the Transdanubian volcanic  
906 region. *J. Petrol.* **30**, 79–106.

907 Falus G., Drury M. R., van Roermund H. L. M. and Szabó C. (2004) Magmatism-related  
908 localized deformation in the mantle: a case study. *Contrib. to Mineral. Petrol.* **146**, 493–  
909 505. Available at: <http://link.springer.com/10.1007/s00410-003-0513-7> [Accessed  
910 February 8, 2014].

911 Falus G., Szabó C., Kovács I., Zajacz Z. and Halter W. (2007) Symplectite in spinel lherzolite  
912 xenoliths from the Little Hungarian Plain, Western Hungary: A key for understanding  
913 the complex history of the upper mantle of the Pannonian Basin. *Lithos* **94**, 230–247.  
914 Available at: <http://linkinghub.elsevier.com/retrieve/pii/S0024493706001848> [Accessed  
915 December 7, 2012].

916 Fodor L., Csontos L., Bada G., Györfi I. and Benkovics L. (1999) Tertiary tectonic evolution  
917 of the Pannonian basin and neighbouring orogenes: a new synthesis of palaeostress data.  
918 In: Durand, B., Jolivet, L., Horváth, F., Séranne, M. (Eds.), *The Mediterranean Basins:  
919 Tertiary Extension with Alpine Orogen.* *Geol. Soc.* **156**, 295–334.

920 Foley S. F., Barth M. G. and Jenner G. a. (2000) Rutile/melt partition coefficients for trace  
921 elements and an assessment of the influence of rutile on the trace element characteristics

922 of subduction zone magmas. *Geochim. Cosmochim. Acta* **64**, 933–938.

923 Gagnon J. E., Fryer B. J., Samson I. M. and Williams-Jones A. E. (2008) Quantitative  
924 analysis of silicate certified reference materials by LA-ICPMS with and without an  
925 internal standard. *J. Anal. At. Spectrom.* **23**, 1529.

926 Ghiorso M. S. and Gualda G. A. R. (2015) An H<sub>2</sub>O-CO<sub>2</sub> mixed fluid saturation model  
927 compatible with rhyolite-MELTS. *Contrib. to Mineral. Petrol.*

928 Gualda G. A. R., Ghiorso M. S., Lemons R. V. and Carley T. L. (2012) Rhyolite-MELTS: a  
929 Modified Calibration of MELTS Optimized for Silica-rich, Fluid-bearing Magmatic  
930 Systems. *J. Petrol.* **53**, 875–890. Available at:  
931 [http://www.petrology.oxfordjournals.org/cgi/doi/10.1093/](http://www.petrology.oxfordjournals.org/cgi/doi/10.1093/petrology/egr080)  
[petrology/egr080](http://www.petrology.oxfordjournals.org/cgi/doi/10.1093/petrology/egr080).

932 Harangi S. and Lenkey L. (2007) Genesis of the Neogene to Quaternary volcanism in the  
933 Carpatian Pannonian region : Role of subduction , extension , and mantle plume. *Geol.*  
934 *Soc. Am. Special Pa*, 67–92.

935 Hellebrand E., Snow J. E., Hoppe P. and Hofmann A. W. (2002) Garnet-field Melting and  
936 Late-stage Refertilization in “ Residual ” Abyssal Peridotites from the Central Indian  
937 Ridge. *J. Petrol.* **43**, 2305–2338.

938 Horvath F. (1993) Towards a mechanical model for the formation of the Pannonian Basin.  
939 *Tectonophysics* **226**, 333–357.

940 Huisman R. S., Podladchikov Y. Y. and Cloetingh S. a. P. L. (2002) The Pannonian basin:  
941 Dynamic modelling of the transition from passive to active rifting. In *EGU Special*  
942 *publication Series* pp. 41–63. Available at: [http://www.stephan-mueller-spec-publ-](http://www.stephan-mueller-spec-publ-ser.net/3/41/2002/)  
943 [ser.net/3/41/2002/](http://www.stephan-mueller-spec-publ-ser.net/3/41/2002/).

944 Ionov D. a., Chanefo I. and Bodinier J. L. (2005) Origin of Fe-rich Iherzolites and wehrlites  
945 from Tok, SE Siberia by reactive melt percolation in refractory mantle peridotites.  
946 *Contrib. to Mineral. Petrol.* **150**, 335–353.

947 Johnson K. T. M., Dick H. J. B. and Shimizu N. (1990) Melting in the oceanic upper mantle:  
948 An ion microprobe study of diopsides in abyssal peridotites. *J. Geophys. Res.* **95**, 2661.

949 Kazmer M. and Kovacs S. (1985) Eocene–Paleogene paleogeography along the Eastern part  
950 of the Insubric–Periadriatic Lineament system: evidence for continental escape of the  
951 Bakony–Drauzug unit. *Acta Geol. Hung.* **1-2**, 71–84.

952 Kereszturi G., Németh K., Csillag G., Balogh K. and Kovács J. (2011) The role of external  
953 environmental factors in changing eruption styles of monogenetic volcanoes in a  
954 Mio/Pleistocene continental volcanic field in western Hungary. *J. Volcanol. Geotherm.*  
955 *Res.* **201**, 227–240. Available at:  
956 <http://www.sciencedirect.com/science/article/pii/S0377027310002647> [Accessed  
957 January 19, 2015].

958 Kovacs I., Falus G., Stuart G., Hidas K., Szabó C., Flower M. F. J., Hegedűs E., Posgay K.  
959 and Zilahi-Sebess L. (2012) Seismic anisotropy and deformation patterns in upper  
960 mantle xenoliths from the central Carpathian–Pannonian region: Asthenospheric flow as  
961 a driving force for Cenozoic extension and extrusion? *Tectonophysics* **514-517**, 168–179.  
962 Available at: <http://linkinghub.elsevier.com/retrieve/pii/S0040195111004562> [Accessed  
963 November 14, 2014].

964 Laurora a, Mazzucchelli M., Rivalenti G., Vannucci R., Zanetti A., Barbieri M. a and  
965 Cingolani C. a (2001) Metasomatism and melting in carbonated peridotite xenoliths from  
966 the mantle wedge: The Gobernador Gregores case (southern Patagonia). *J. Petrol.* **42**,  
967 69–87.

968 Locock A. J. (2014) An Excel spreadsheet to classify chemical analyses of amphiboles  
969 following the IMA 2012 recommendations. *Comput. Geosci.* **62**, 1–11. Available at:  
970 <http://dx.doi.org/10.1016/j.cageo.2013.09.011>.

971 Lu J., Zheng J., Grif W. L., Reilly S. Y. O. and Pearson N. J. (2015) Lithos Microscale effects



972 of melt in filtration into the lithospheric mantle : Peridotite xenoliths from Xilong , South  
973 China. *Lithos* **232**, 111–123.

974 Martin U., Auer A., Németh K. and Breitschneider C. (2003) Mio-pliocene phreatomagmatic  
975 volcanism in a Fluvio–Lacustrine basin in Western Hungary. *GeoLines* **15**, 93–97.

976 McDonough W. F. F. and Sun S. -s. S. . (1995) The composition of the Earth. *Chem. Geol.*  
977 **120**, 223–253. Available at:  
978 <http://www.sciencedirect.com/science/article/pii/0009254194001404> [Accessed January  
979 15, 2015].

980 Mercier J. C. and Nicolas A. (1975) Textures and Fabrics of Upper-Mantle Peridotites as  
981 Illustrated by Xenoliths from Basalts. *J. Petrol.* **16**.

982 Miller C., Zanetti a., Thöni M., Konzett J. and Klötzli U. (2012) Mafic and silica-rich glasses  
983 in mantle xenoliths from Wau-en-Namus, Libya: Textural and geochemical evidence for  
984 peridotite-melt reactions. *Lithos* **128-131**, 11–26. Available at:  
985 <http://dx.doi.org/10.1016/j.lithos.2011.11.004>.

986 Moine B. N., Grégoire M., O’Reilly S. Y., Delpech G., Sheppard S. M. F., Lorand J. P.,  
987 Renac C., Giret a. and Cottin J. Y. (2004) Carbonatite melt in oceanic upper mantle  
988 beneath the Kerguelen Archipelago. *Lithos* **75**, 239–252.

989 Neumann E.-R., Wulff-Pedersen E., Pearson N. J. and Spenser E. a (2002) Mantle xenoliths  
990 from Tenerife (Canary Islands): evidence for reactions between mantle peridotites and  
991 silicic carbonatite melts inducing Ca metasomatism. *J. Petrol.* **43**, 825–857. Available at:  
992 <http://petrology.oupjournals.org/cgi/content/abstract/43/5/825>.

993 Niida K. and Green D. H. (1999) Stability and chemical composition of pargasitic amphibole  
994 in MORB pyroxenite under upper mantle conditions. *Contrib. to Mineral. Petrol.* **135**, 18–  
995 40.

996 Olafsson M. and Eggler D. H. (1983) Phase relations of amphibole, amphibole-carbonate, and

997 phlogopite-carbonate peridotite: petrologic constraints on the asthenosphere. *Earth*  
998 *Planet. Sci. Lett.* **64**, 305–315. Available at:  
999 <http://linkinghub.elsevier.com/retrieve/pii/0012821X83902121>.

1000 Posgay K., Bodoky T., Hegedus E., Kovacsvolgyi S., Lenkey L., Szafian P., Takacs E., Timar  
1001 Z. and Varga G. (1995) Asthenospheric structure beneath a Neogene basin in southeast  
1002 Hungary. *Tectonophysics* **252**, 467–484.

1003 Putirka K. D. (2008) Thermometers and Barometers for Volcanic Systems. *Mineral.*  
1004 *Geochemistry* **69**, 61–120.

1005 Rapp R. ., Shimizu N., Norman M. . and Applegate G. . (1999) Reaction between slab-derived  
1006 melts and peridotite in the mantle wedge: experimental constraints at 3.8 GPa. *Chem.*  
1007 *Geol.* **160**, 335–356. Available at:  
1008 <http://www.sciencedirect.com/science/article/pii/S0009254199001060> [Accessed March  
1009 16, 2015].

1010 Roedder E. (1984) Fluid inclusions. *Rev. Mineral.* **12**.

1011 Shaw C. S. J. and Dingwell D. B. (2008) Experimental peridotite-melt reaction at one  
1012 atmosphere: A textural and chemical study. *Contrib. to Mineral. Petrol.* **155**, 199–214.

1013 Shaw C. S. J., Heidelbach F. and Dingwell D. B. (2006) The origin of reaction textures in  
1014 mantle peridotite xenoliths from Sal Island, Cape Verde: the case for “metasomatism” by  
1015 the host lava. *Contrib. to Mineral. Petrol.* **151**, 681–697. Available at:  
1016 <http://link.springer.com/10.1007/s00410-006-0087-2> [Accessed November 14, 2014].

1017 Spakman W. (1990) Tomographic images on the upper mantle below Europe and the  
1018 Mediterranean. *Ter. Nov.* **2**, 542–553.

1019 Szabó C., Bodnar R. J. and Sobolev A. V. (1996) Metasomatism associated with subduction-  
1020 related, volatile-rich silicate melt in the upper mantle beneath the Nograd-Gomor  
1021 Volcanic Field, Northern Hungary/Southern Slovakia – Evidence from silicat. *Eur. J.*

- 1022 *Miner.* **8**, 881–899.
- 1023 Szabó C., Falus G., Zajacz Z., Kovács I. and Bali E. (2004) Composition and evolution of  
1024 lithosphere beneath the Carpathian–Pannonian Region: a review. *Tectonophysics* **393**,  
1025 119–137. Available at: <http://linkinghub.elsevier.com/retrieve/pii/S0040195104002574>  
1026 [Accessed December 7, 2012].
- 1027 Szabó C., Harangi S. and Csontos L. (1992) Review of Neogene and Quaternary volcanism of  
1028 the Carpathian-Pannonian region. *Tectonophysics* **208**, 243–256.
- 1029 Szabó C., Harangi S., Vaselli O. and Downes H. (1995) Temperature and oxygen fugacity in  
1030 peridotite xenoliths from the Carpathian-Pannonian Region. *Acta Vulcanol.* **7**, 231–239.
- 1031 Szabó C., Hidas K., Bali E., Zajacz Z., Kovács I., Yang K., Guzmics T. and Török K. (2009)  
1032 Melt-wall rock interaction in the mantle shown by silicate melt inclusions in peridotite  
1033 xenoliths from the central Pannonian Basin (western Hungary). *Isl. Arc* **18**, 375–400.  
1034 Available at: <http://doi.wiley.com/10.1111/j.1440-1738.2009.00672.x> [Accessed  
1035 December 7, 2012].
- 1036 Szabó C., Kovacs I., Dégi J., Kothay K., Torok K., Hidas K. K., Konya P., Berkesi M., Degi  
1037 J., Kothay K., Torok K., Hidas K. K., Konya P. and Berkesi M. (2010) From maars to  
1038 lava lakes: Ultramafic and granulite xenoliths associated with the alkaline basaltic  
1039 volcanism of the Pannonian Basin. In *Mineralogica-petrographica field guide series* pp.  
1040 1–32.
- 1041 Tašárová A., Afonso J. C., Bielik M., Götze H.-J. and Hók J. (2009) The lithospheric structure  
1042 of the Western Carpathian–Pannonian Basin region based on the CELEBRATION 2000  
1043 seismic experiment and gravity modelling. *Tectonophysics* **475**, 454–469. Available at:  
1044 <http://linkinghub.elsevier.com/retrieve/pii/S0040195109003229> [Accessed January 22,  
1045 2014].
- 1046 Török K., Dégi J., Szép A. and Marosi G. (2005) Reduced carbonic fluids in mafic granulite

1047 xenoliths from the Bakony–Balaton Highland Volcanic Field, W-Hungary. *Chem. Geol.*  
1048 **223**, 93–108. Available at:  
1049 <http://linkinghub.elsevier.com/retrieve/pii/S0009254105002913> [Accessed December 7,  
1050 2012].

1051 Vannucci R., Bottazzi P., Wulff-Pedersen E. and Neumann E.-R. (1998) Partitioning of REE,  
1052 Y, Sr, Zr, and Ti between clinopyroxene and silicate melts in the mantle under La Palma  
1053 (Canary Islands): implications for the nature of the metasomatic agents. *Earth Planet.*  
1054 *Sci. Lett.* **158**, 39–51.

1055 Wijbrans J., Németh K., Martin U. and Balogh K. (2007) <sup>40</sup>Ar/<sup>39</sup>Ar geochronology of  
1056 Neogene phreatomagmatic volcanism in the western Pannonian Basin, Hungary. *J.*  
1057 *Volcanol. Geotherm. Res.* **164**, 193–204. Available at:  
1058 <http://www.sciencedirect.com/science/article/pii/S0377027307001357> [Accessed  
1059 January 14, 2015].

1060 Wulff-Pedersen E., Neumann E.-R., Vannucci R., Bottazzi P. and Ottolini L. (1999) Silicic  
1061 melts produced by reaction between peridotite and infiltrating basaltic melts : ion probe  
1062 data on glasses and minerals in veined xenoliths from La Palma , Canary Islands.  
1063 *Contrib. to Mineral. Petrol.* **137**, 59–82.

1064 Xiong X. L., Adam J. and Green T. H. (2005) Rutile stability and rutile/melt HFSE  
1065 partitioning during partial melting of hydrous basalt: Implications for TTG genesis.  
1066 *Chem. Geol.* **218**, 339–359.

1067 Yaxley G. M. and Kamenetsky V. (1999) In situ origin for glass in mantle xenoliths from  
1068 southeastern Australia : insights from trace element compositions of glasses and  
1069 metasomatic phases. *Earth Planet. Sci. Lett.* **172**, 97–109. Available at:  
1070 [http://dx.doi.org/10.1016/S0012-821X\(99\)00196-X](http://dx.doi.org/10.1016/S0012-821X(99)00196-X).  
1071

1 Figure captions

2

3 Figure 1: Location of the Bakony Balaton highland volcanic field and of the four sampling  
4 areas (Szentbékakála, Szigliget, Füzes-tó, Mindszentkála). The light grey area is the Outer  
5 Carpathians and the dark grey area represents the Carpathian belt (North, East and South-  
6 East), Eastern Alps (West) and Dinarides (South West).

7

8 Figure 2: Streckeisen diagram (Streckeisen, 1976) of studied mantle xenoliths. They are all  
9 within the fields of lherzolites (diamonds) and harzburgites (triangles). Small circles are  
10 literature data from [Downes et al. \(1992\)](#); [Falus et al. \(2004\)](#); [Bali et al. \(2002\)](#). SZB-  
11 Szentbékakála, SZG- Szigliget, FT- Füzes-tó and MSZK- Mindszentkála. The grey area  
12 corresponds to the Sub-continental lithospheric mantle (Downes et al., 1992).

13

14 Figure 3: Textural characteristics of the Szentbékakála, Szigliget, Füzes-tó and Mindszentkála  
15 mantle xenoliths. A- Primary silicate melt inclusions (SMI) in a primary cpx; Some cpx  
16 present spongy rim (SZG14). B- Poikilitic opx containing ol and trails of secondary fluid  
17 inclusions (SZG14). C- Melt vein crosscutting the peridotite sample and reacting with Cpx  
18 (spongy textures); secondary crystallization of SpII, OIII and CpxII in the melt; trails of  
19 secondary fluid inclusions are crosscutting the vein (SZB16). D- Interconnected melt pockets  
20 in SZG23; The box is a zoom in a melt pocket of SZB16. E- Glass pocket with few cpx  
21 secondary crystallization at boundaries (SZG44). F- Numerous trails of secondary fluid  
22 inclusions crosscutting together cpx and opx (SZB51); The box is a zoom on fluid inclusions.  
23 G-. Pseudomorphic melt pocket after amphibole breakdown (SZB51). H- Pseudomorphic melt  
24 pocket after amphibole breakdown (FT08P. Ol- olivine, Opx- Orthopyroxene, Cpx-

25 Clinopyroxene, Sp- spinel, Amp- amphibole, FI- fluid inclusions, MP- melt pocket, Vs-  
26 vesicle, M.I- Primary mineral, M.II- Secondary mineral, SMI- silicate melt inclusion.

27

28 Figure 4: Major-element compositions for primary minerals of the mantle xenoliths from the  
29 four sampled areas. Literature from [Downes et al. \(1992\)](#); [Embey-Isztin et al. \(1989\)](#); [Bali et](#)  
30 [al. \(2002\)](#); [Falus et al. \(2004\)](#); [Demény et al. \(2004, 2005\)](#). Blue squares: primitive mantle,  
31 triangles: harzburgite-like, diamonds: lherzolites. Black, dark-grey, light grey and white  
32 colors are respectively assigned to Szentbékállá, Szigliget, Füzes-tó and Mindszentkállá. PM  
33 – partial melting.

34

35 Figure 5: Major element compositions of the newly formed cpx, ol and spinels. The grey area  
36 shows the domain for primary mineral compositions for comparison. Black circles:  
37 Szentbékállá, dark-grey circles: Szigliget, light-grey circles: Füzes-tó. Smaller dots are from  
38 [Bali et al. \(2002\)](#).

39

40 Figure 6: REE and trace-element patterns for primary clinopyroxene and amphibole from the  
41 four localities. Grey areas are literature data from [Embey-Isztin et al. \(2014\)](#). Black, dark-  
42 grey, light grey and black dashed lines are respectively assigned to Szentbékállá, Szigliget,  
43 Füzes-tó and Mindszentkállá samples. See text for group description.

44

45 Figure 7: Major-element compositions for vein (circles) and melt pocket (diamond) glass in  
46 samples from SZB (black), SZG (dark-grey) and FT (light grey). The small grey circles are  
47 from [Bali et al. \(2002\)](#). Dotted lines are assimilation of cpx (black), amp (dark grey) and sp  
48 (light grey). The dashed lines represent crystal fractionation (CF) trends calculated using

49 Rhyolite-MELTS ([Gualda et al., 2012](#); [Ghiorso and Gualda, 2015](#)). Black and grey square  
50 present respectively the starting compositions for crystal fractionation and assimilation.

51

52 Figure 8: Trace-element patterns for glass in melt pockets (SMP) in samples of SZB (dark),  
53 SZG (dark-grey) and FT (light-grey).

54

55 Figure 9: Textural observations of amphibole breakdown for the FT08P xenoliths. Vs –  
56 vesicle, Gl – glass, Amp – amphibole, Cpx – clinopyroxene, Sp – spinel.

57

58 Figure 10: Trace element patterns illustrating the assimilation of amphibole in melt. Each  
59 dotted line corresponds to the addition of 10% amphibole in initial vein type melt.

60

61 Figure 11: Pressure comparison between primary mineral chemical equilibrium, secondary  
62 crystalized mineral/melt chemical equilibrium, fluid inclusions trapping and vesicles last  
63 equilibrium with melt. Primary minerals are formed at deeper pressures and vesicles, silicate  
64 melt pockets and fluid inclusions trapping happened at close pressures near to the MOHO.

65

66 Figure 12: Major element variations in veins and melt pockets (MP) for Szentbékállá (SZB),  
67 Szigliget (SZG) and Füzes-tó (FT). Comparison is given by adakites, mantle xenolith glasses  
68 from [Draper & Green \(1997\)](#), experimental melts from [Rapp et al. \(1999\)](#), calc-alkali magmas  
69 of the Pannonian Basin ([Harangi and Lenkey, 2007](#)), silicate melt pockets of SZB mantle  
70 xenoliths (small circles, [Bali et al., 2002](#); [Demény et al., 2004](#)) and silicate melt inclusions of  
71 SZG mantle xenoliths (small circles, [Szabó et al., 2009](#)).

72

73 Figure 13: Trace element patterns comparison between glasses in veins from mantle xenoliths  
74 and Northern Panonnian Basalts, calc-alkaline (16.5-2 Ma, [Harangi and Lenkey, 2007](#)) and  
75 alkaline basalt (11.5 to recently) magmas from BBHVF and assimilation adakite + peridotite  
76 experiments.

77

78 Figure 14: Glass from melt veins compared with known adakite compositional domains (Grey  
79 areas). Small dots are data from [Bali et al. \(2008\)](#).

80

81 Figure 15: Phase equilibrium diagram. A- Modified from [Stern \(2002\)](#) and [Martin \(1999\)](#). The  
82 blue field represents the assumed P-T source of the Si-rich melts in veins. lhz- lherzolite; gar-  
83 garnet; amph- amphibole; sp- spinel; plg- plagioclase. The dry peridotite solidus is from  
84 [Gudfinnsson & Presnall \(2005\)](#). B- Pressure–temperature diagram showing the effects of CO<sub>2</sub>  
85 on the solidus of carbonated lithologies in the mantle. Two different estimates of the  
86 peridotite–CO<sub>2</sub> solidus are reported: CMAS–CO<sub>2</sub> after [Dalton & Presnall \(1998\)](#) and  
87 [Gudfinnsson & Presnall \(2005\)](#), and peridotite–CO<sub>2</sub> (2.5 wt.%) from [Dasgupta & Hirschmann](#)  
88 [\(2006\)](#). The dry peridotite solidus in the CMAS system is from [Gudfinnsson & Presnall](#)  
89 [\(2005\)](#). Eclogite–CO<sub>2</sub> solidus (dry eclogite+5 wt.% CO<sub>2</sub>) from [Dasgupta et al. \(2004\)](#).

90 Asterisks (\*) correspond to the KNCFMASH–CO<sub>2</sub> solidus (carbonated pelite+1.1 wt.%  
91 H<sub>2</sub>O+4.8 wt.% CO<sub>2</sub>) from [Thomsen & Schmidt \(2008\)](#). The effect of carbonates on the  
92 composition of melts generated at increasing temperature is reported as wt. % CO<sub>2</sub>, based on  
93 the CMAS–CO<sub>2</sub> system. The solid blue line represents the geotherm from [Kovacs et al.](#)  
94 [\(2012\)](#)

95

96 Supp\_data, Fig. a: Trace element modeling of residual clinopyroxene using the non-modal  
97 partial melting equations and parameters of [Hellebrand et al. \(2002\)](#) and CI-chondrite



98 normalization values after [McDonough & Sun \(1995\)](#). The numbers refer to the amount of  
99 melting in percentage. Triangles are harzburgite-like rocks and diamonds are lherzolites-like  
100 rocks.

101

Figure 1  
[Click here to download high resolution image](#)

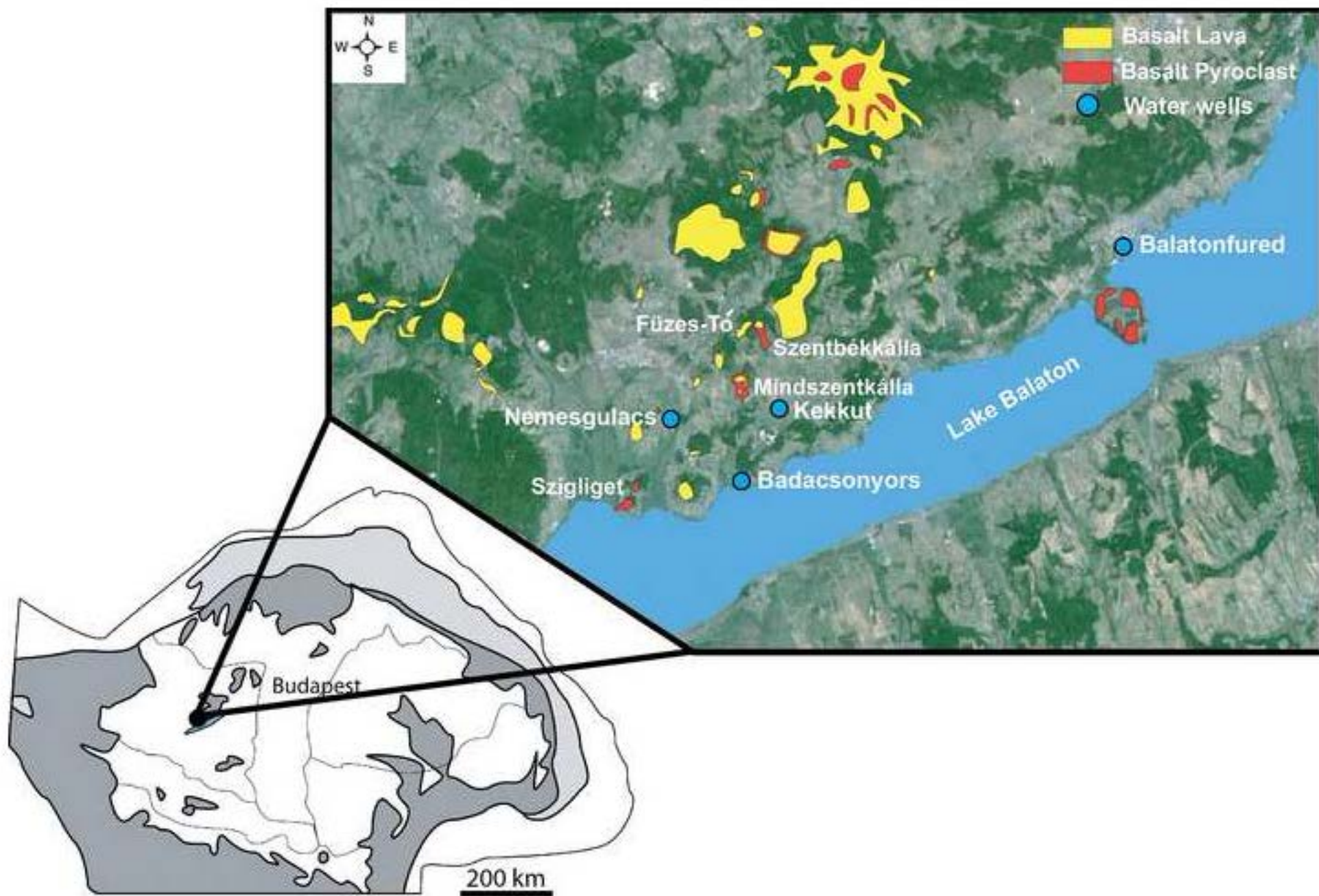


Figure 2  
[Click here to download high resolution image](#)

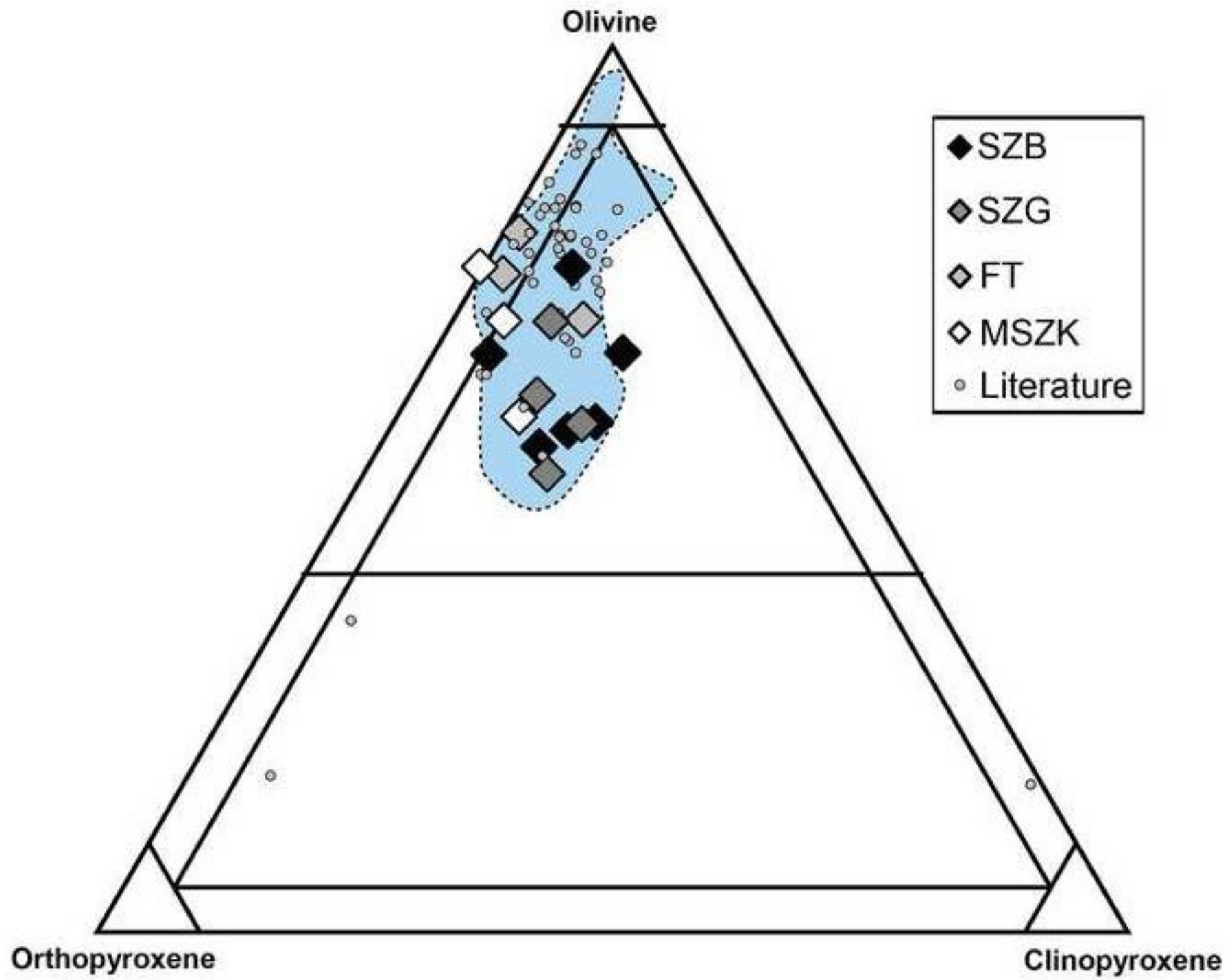




Figure 3  
[Click here to download high resolution image](#)

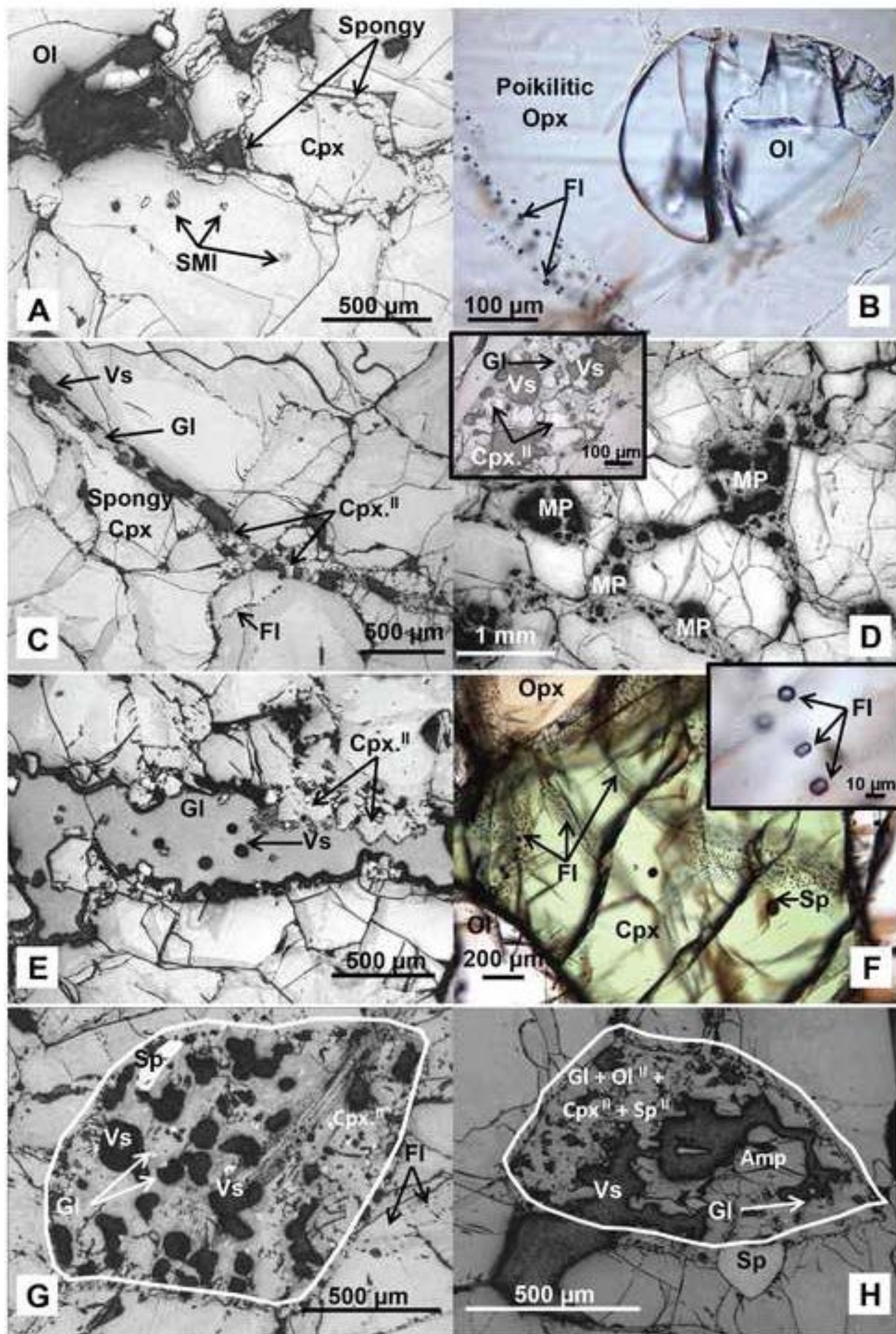


Figure 4  
[Click here to download high resolution image](#)

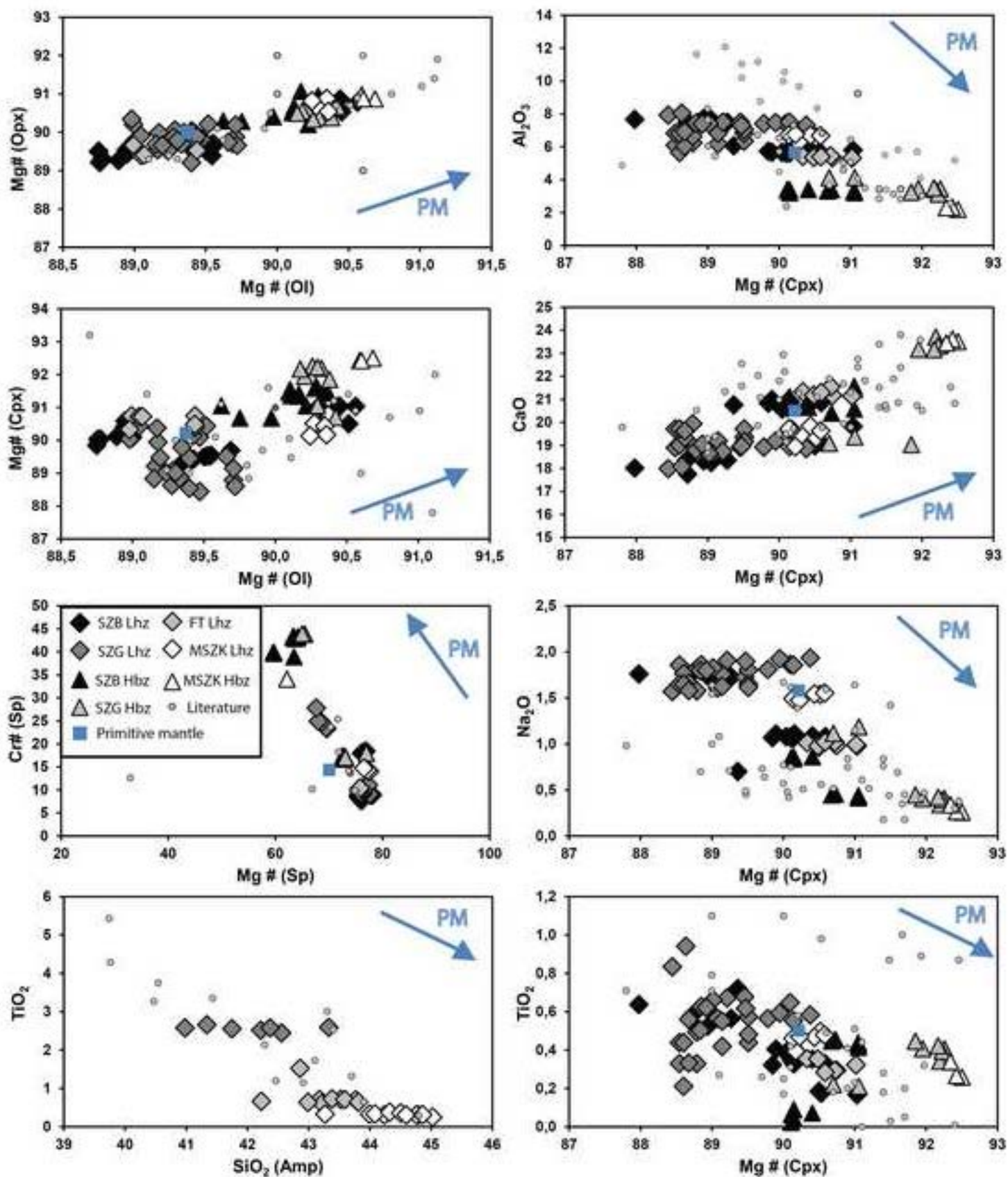




Figure 5  
[Click here to download high resolution image](#)

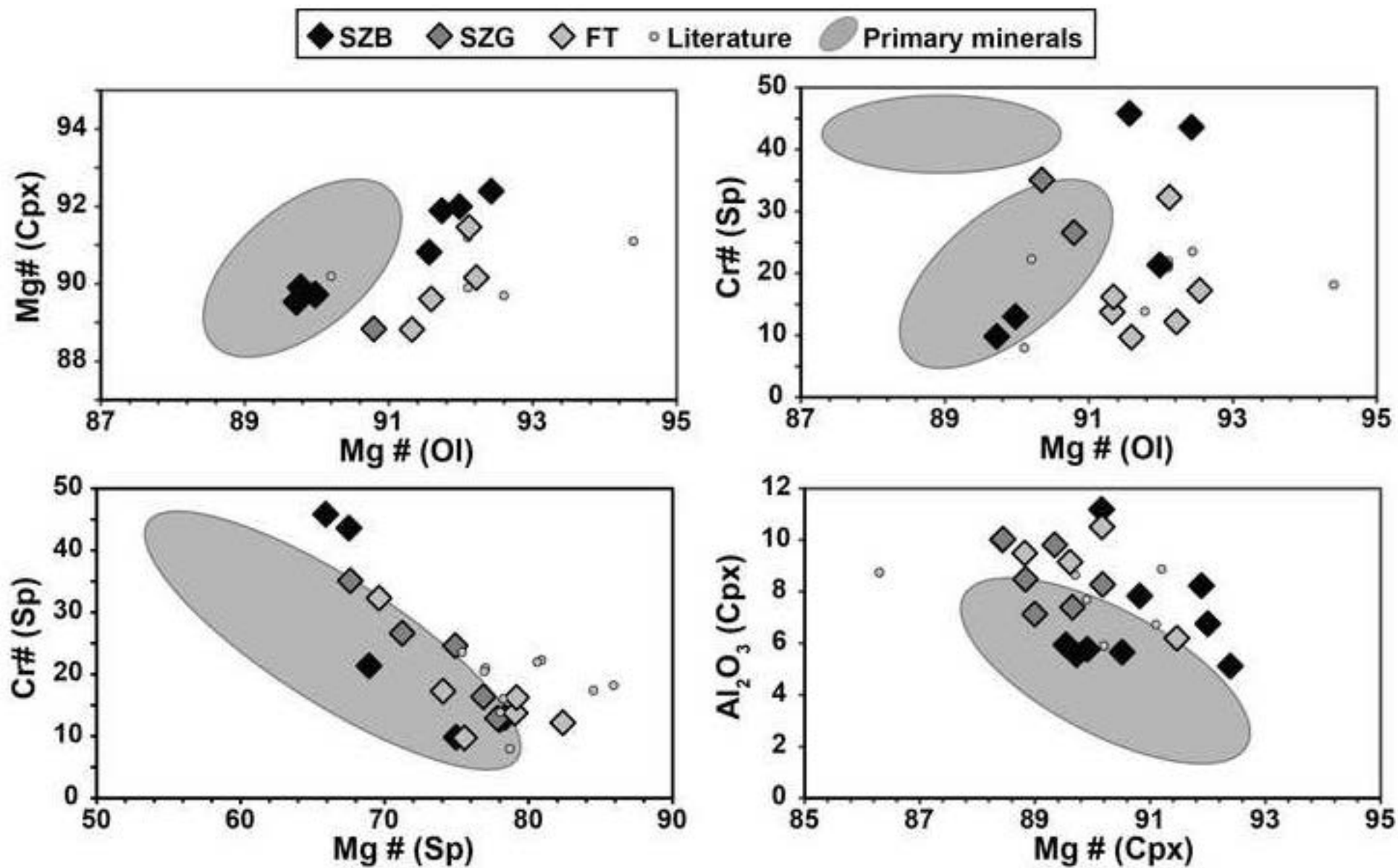


Figure 6  
[Click here to download high resolution image](#)

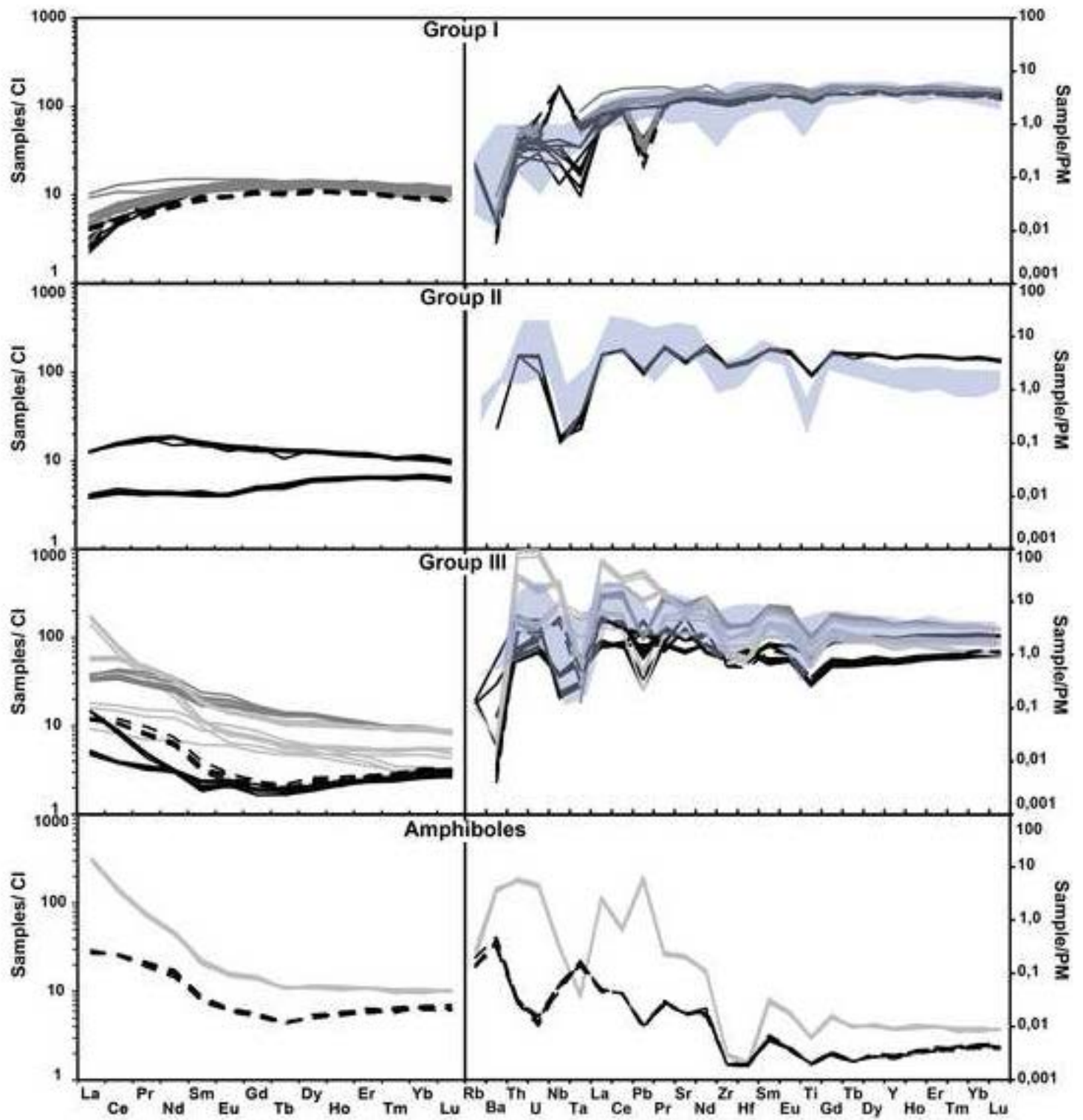


Figure 7  
[Click here to download high resolution image](#)

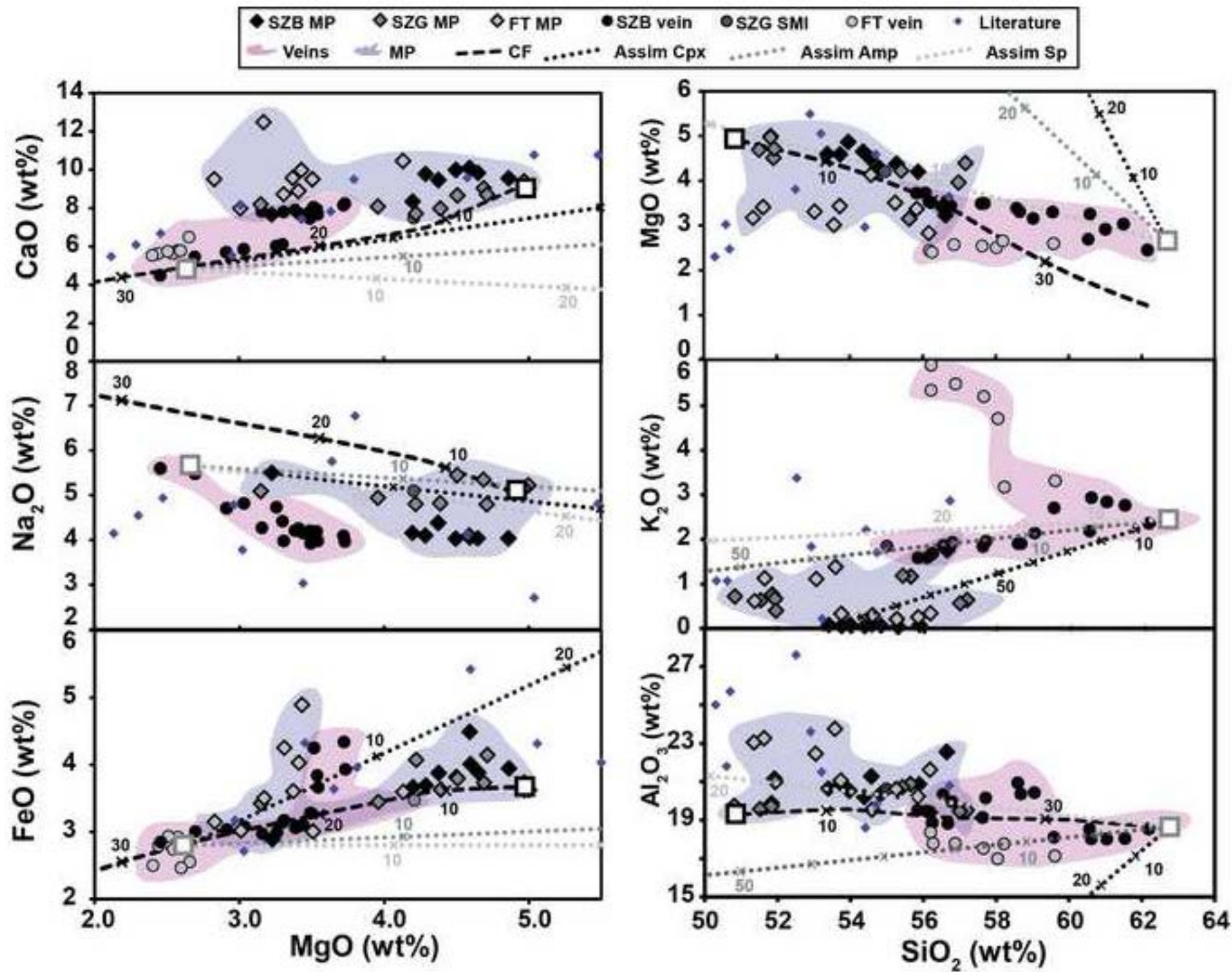




Figure 8  
[Click here to download high resolution image](#)

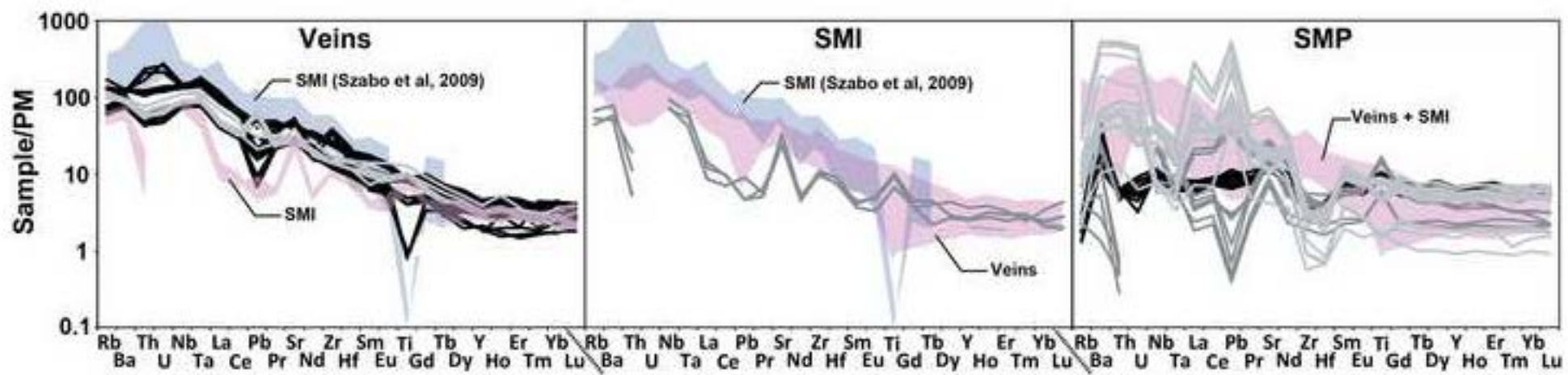


Figure 9  
[Click here to download high resolution image](#)

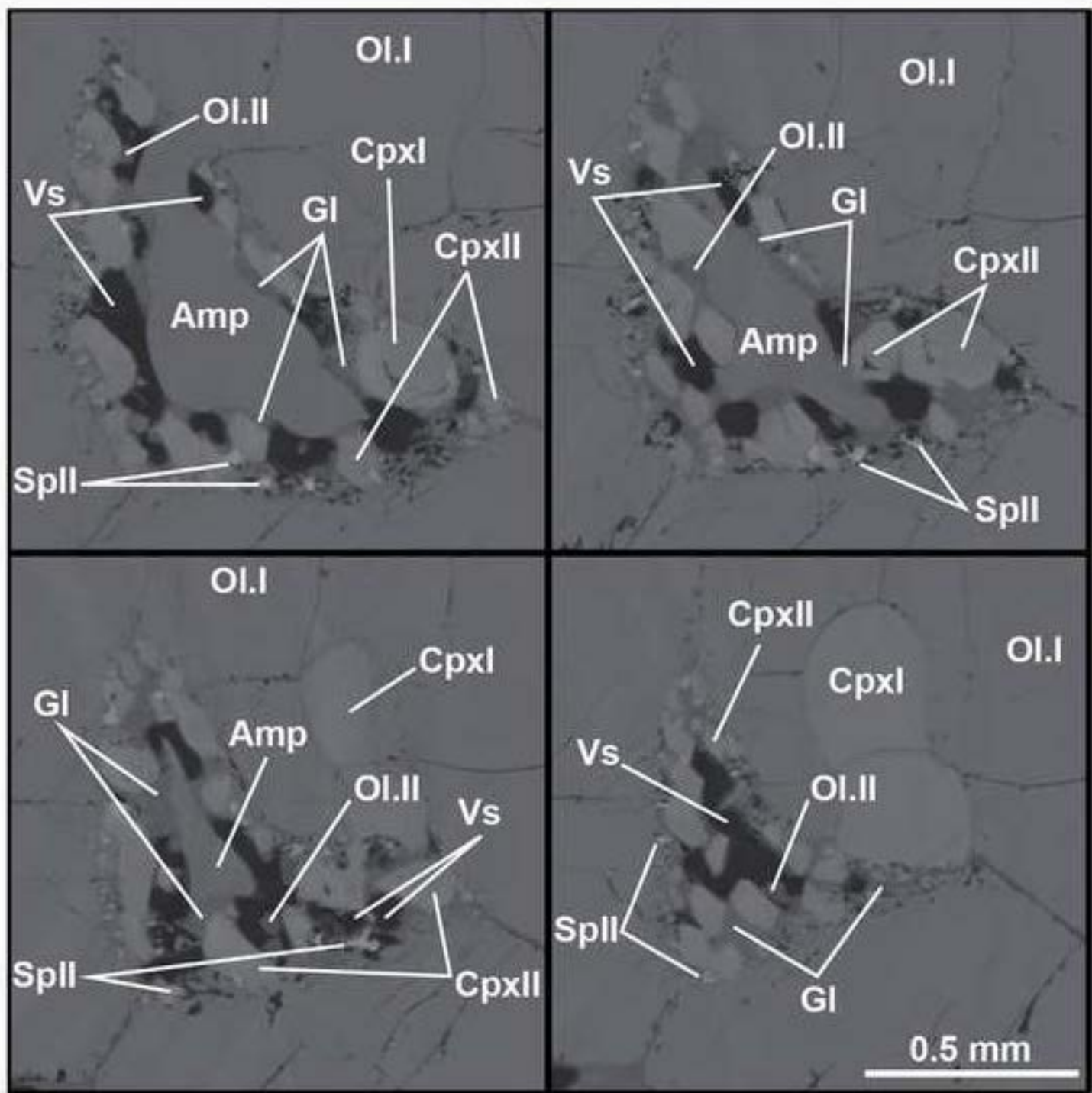


Figure 10  
[Click here to download high resolution image](#)

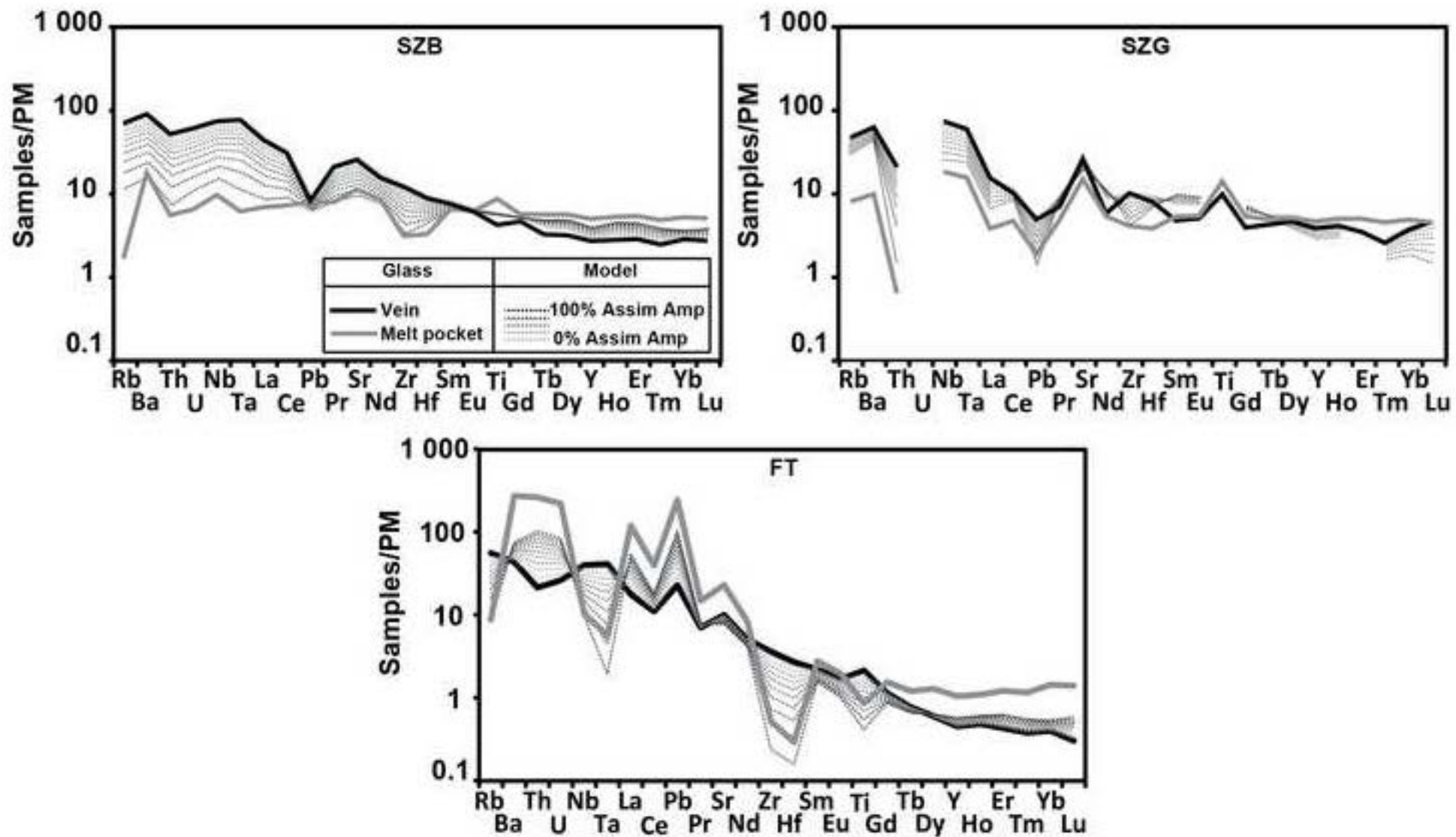


Figure 11  
[Click here to download high resolution image](#)

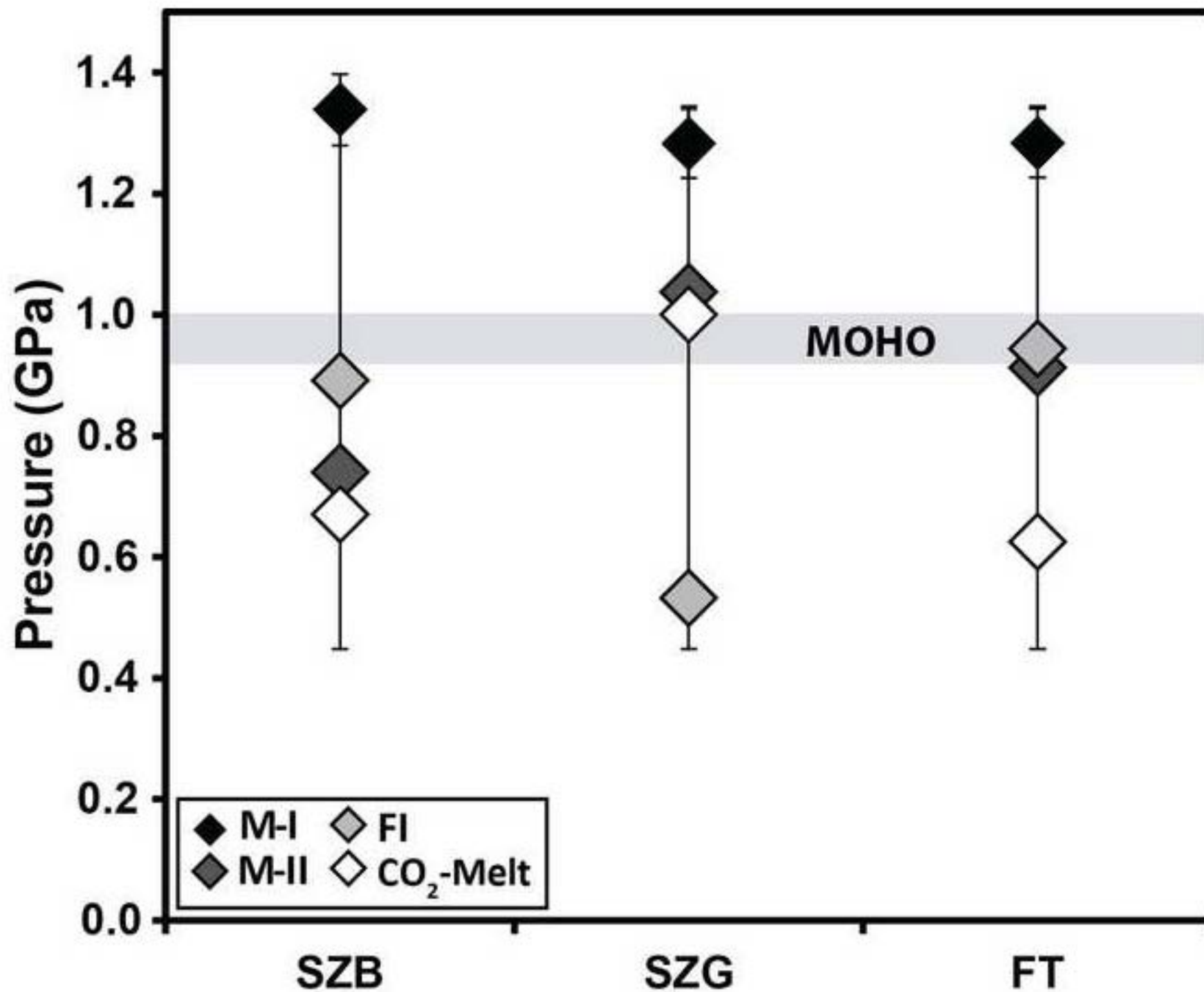




Figure 12  
[Click here to download high resolution image](#)

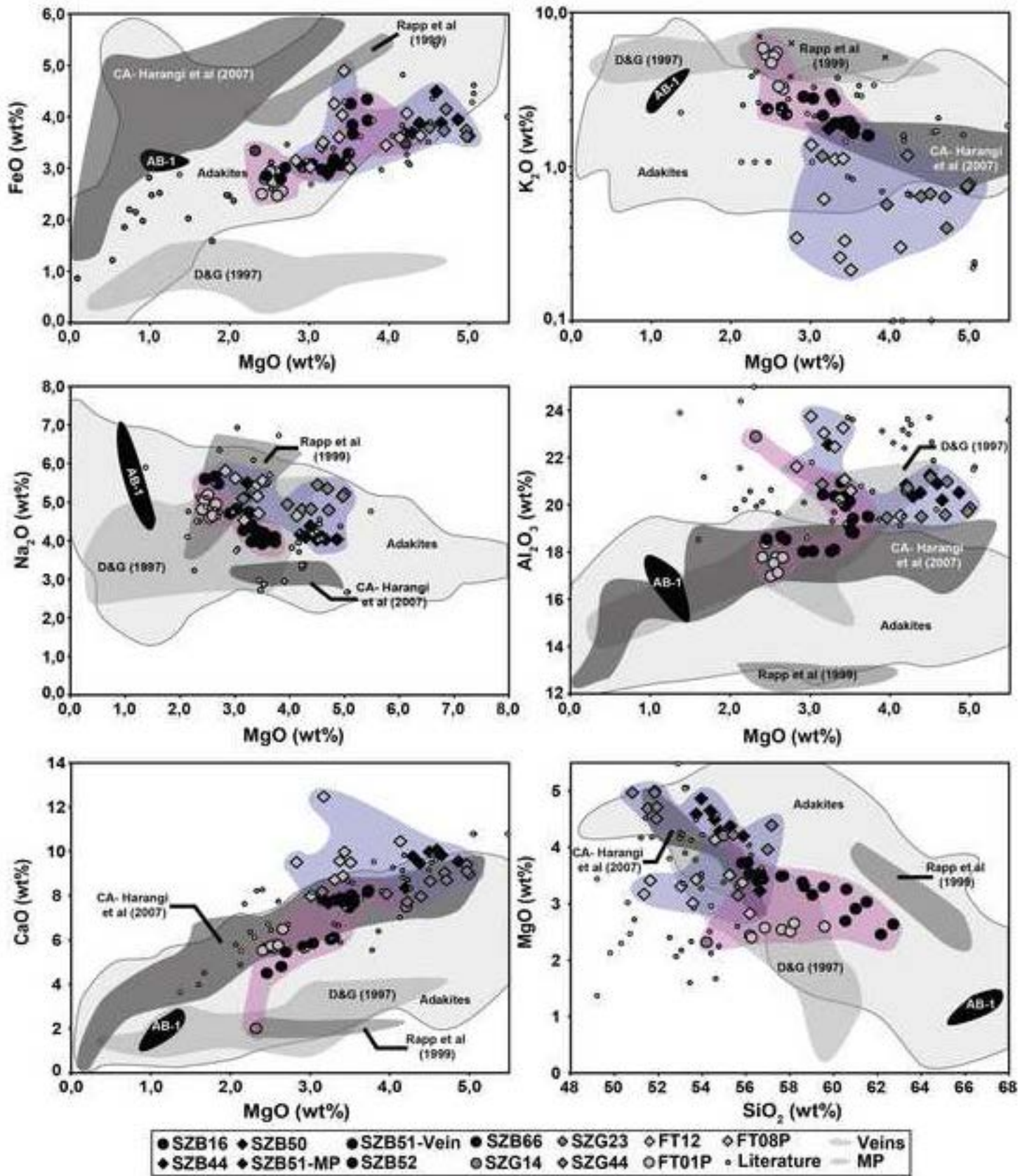


Figure 13  
[Click here to download high resolution image](#)

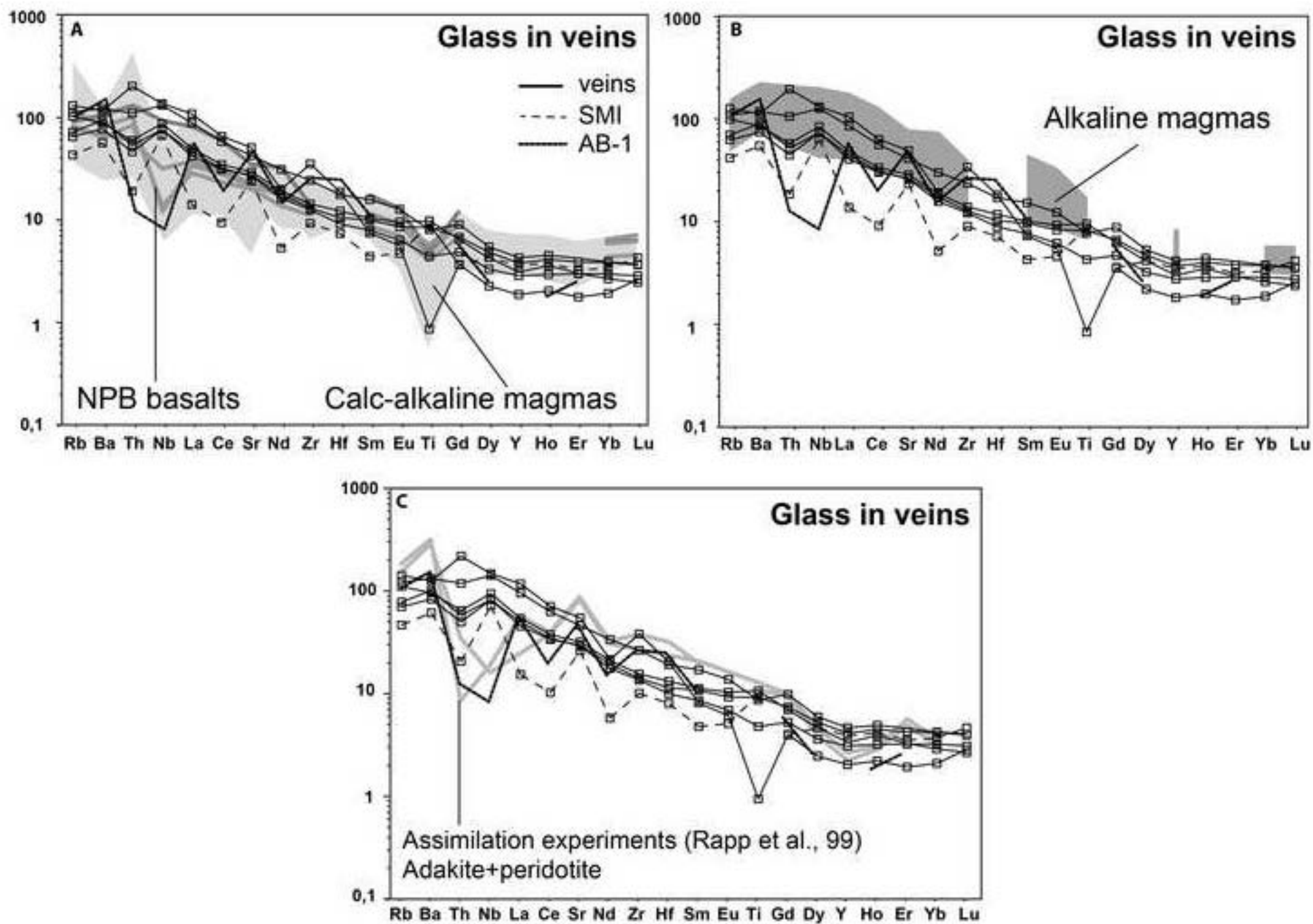


Figure 14  
[Click here to download high resolution image](#)

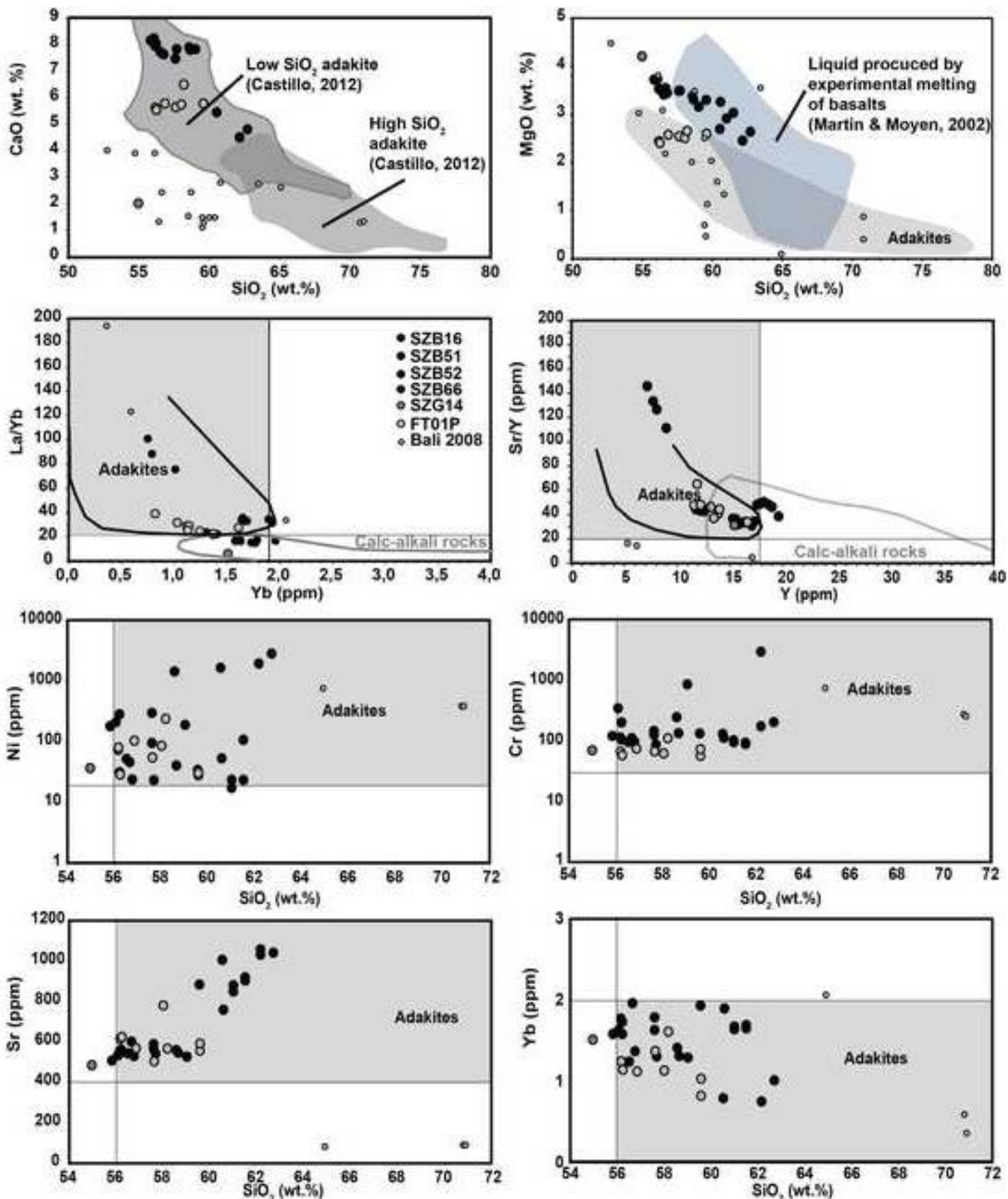
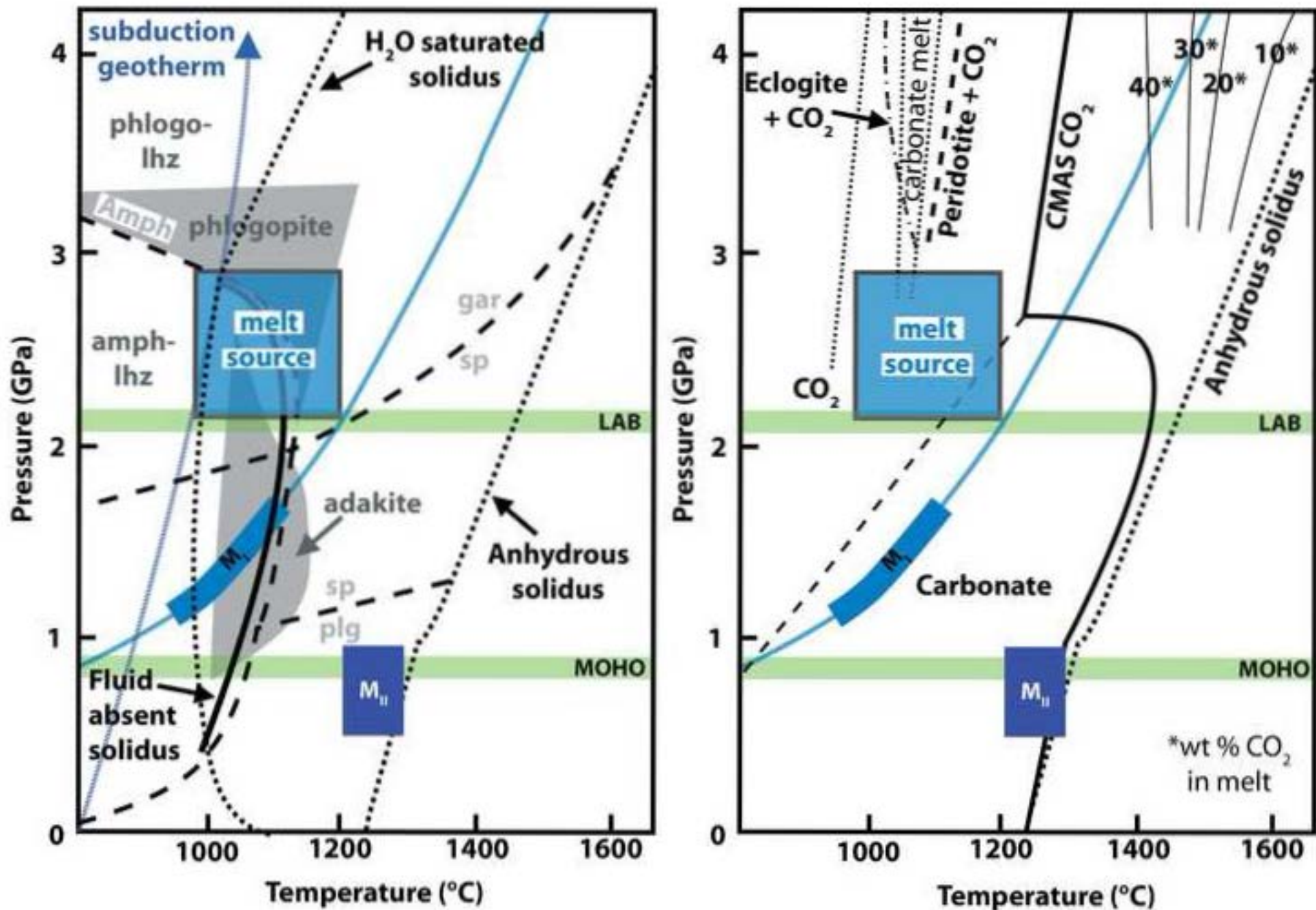




Figure 15  
[Click here to download high resolution image](#)





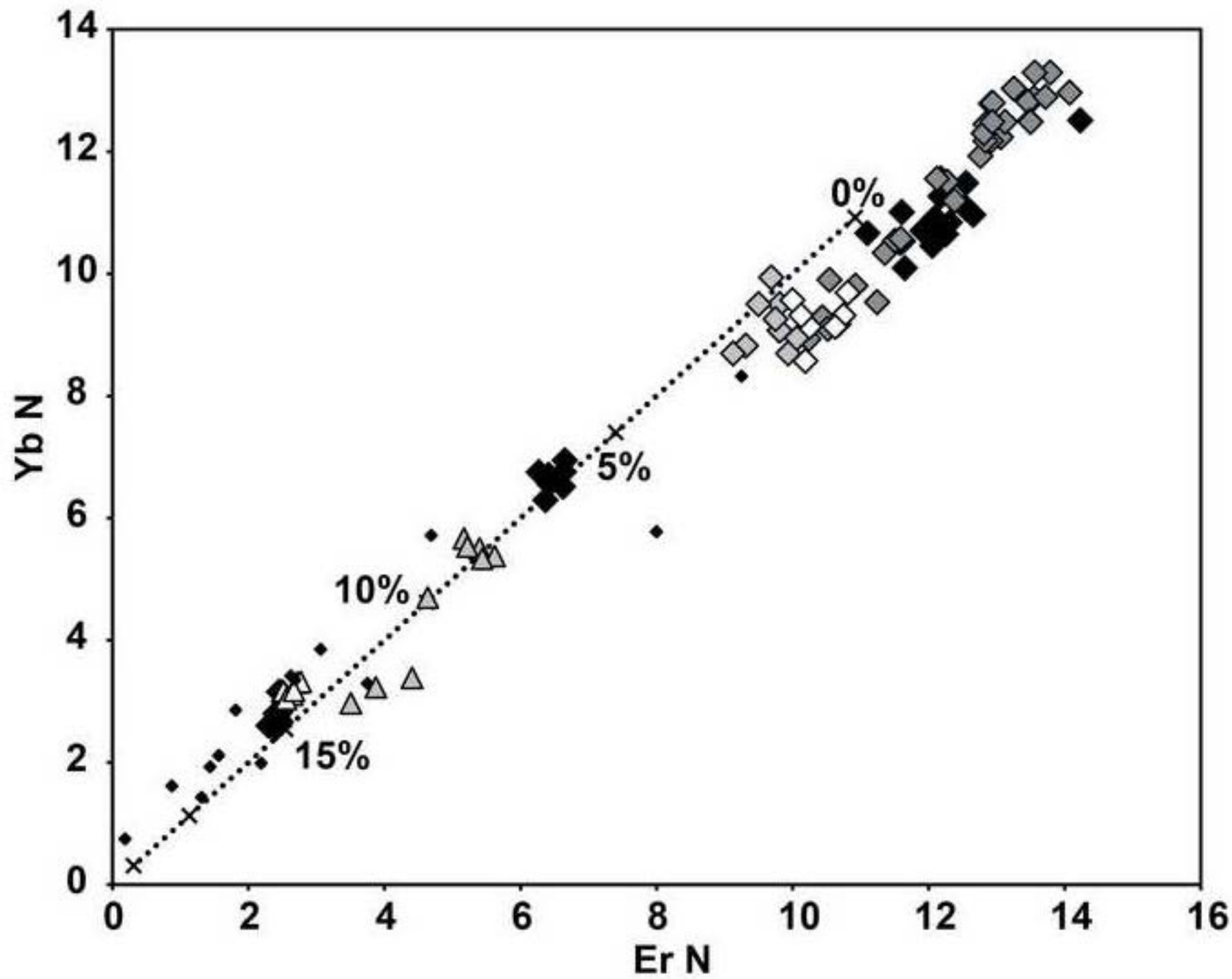


Table1

[Click here to download Table: Table 1.doc](#)

Sample	Whole size	Grain size		Texture	Minerals	Rock name	Fluid inclusions	Melt	2 <sup>nd</sup> Minerals	Major petrographic characters
SZB16	9 cm	<1 to >3 mm	H	Protogranular	Ol, Opx, Cpx, Sp	Lz	2 <sup>ndary</sup>	Vein	Ol, Cpx, Sp	Minerals in contact with melt are broken-down. Phyllosilicates observed in vein. Some Gl (S) observed
SZB44	7 cm	<1 mm	E	Mosaic + Poikilitic features	Ol, Opx, Cpx, Sp	Lz	2 <sup>ndary</sup>	MP	Ol, Cpx, Sp	Spongy Sp at melt contact. Some Gl (S) observed
SZB50	7 cm	~1 mm	E	Mosaic	Ol, Opx, Cpx, Sp	Lz	2 <sup>ndary</sup>	Vein + MP	Ol, Cpx, Sp	Spongy Sp. Gl (S) sometimes associated with FI
SZB51	11 cm	1 to 5 mm	H	Protogranular	Ol, Opx, Cpx, Sp	Lz	2 <sup>ndary</sup>	MP	Ol, Cpx, Sp	Spongy Sp. Large Gl (S) in melt. Melt pocket formed from Cpx breakdown
SZB52	9 cm	<1 to 5 mm	H	Protogranular	Ol, Opx, Cpx, Sp	Lz	2 <sup>ndary</sup>	Vein	Ol, Cpx, Sp	Large vein. No mineral breakdown. Gl (S) sometimes associated with FI
SZB66	18 cm	4 to 6 mm	E	Protogranular + Poikilitic features	Ol, Opx, Cpx, Sp	Lz	2 <sup>ndary</sup>	Vein	Ol, Cpx, Sp	Poikilitic Ol (containing Opx). Little reaction between melt and minerals
SZG14	7 cm	~1 mm	E	Protogranular	Ol, Opx, Cpx, Sp	Lz	2 <sup>ndary</sup>	Vein + SMI	Ol, Cpx, Sp	Poikilitic Opx (containing Ol). Spongy Opx
SZG23	7 cm	<1 to 4 mm	H	Protogranular	Ol, Opx, Cpx, Sp	Lz	2 <sup>ndary</sup>	MP + Vein	Ol, Cpx, Sp	Lot of melt and fluid percolation. Lot of oxides in melt pockets
SZG30	5 cm	~1 mm	E	Mosaic	Cpx, Sp + Amph	Lz	2 <sup>ndary</sup>	Vein	Ol, Cpx, Sp	Lot of carbonate melts + fluid. Amph are broken-down. Gl (S), carbonate melts veins and FI
SZG44	7 cm	~1-2 mm	E	Protogranular with Mosaic tendency	Ol, Opx, Cpx, Sp	Lz	2 <sup>ndary</sup>	Vein + Pockets	Ol, Cpx, Sp	Ol and Cpx are destabilized at melt contact. Gl (S) observed at melt/minerals boundaries
FT12	9 cm	~1 mm	E	Mosaic	Ol, Opx, Cpx, Sp + Amph	Lz	2 <sup>ndary</sup>	MP + Vein	Ol, Cpx, Sp	Broken-down Amph at melt contact. Some Gl (S) at grain boundaries
FT01P	12 cm	<1 to 5 mm	H	Protogranular	Ol, Opx, Cpx, Sp	Hzb	2 <sup>ndary</sup>	Vein	Ol, Cpx, Sp	Gl (S) sometimes associated with FI. Cryptic metasomatism. Newly formed minerals at grain boundaries
FT08P	8 cm	1 to 2 mm	E	Tabular	Ol, Opx, Cpx, Sp + Amph	Hzb	2 <sup>ndary</sup>	Vein + Mp	Ol, Cpx, Sp	Gl (S) observed. Broken-down Amph with CpxII crystallization. Beginning of Opx break-down
MSZK1306 A	2.5 cm	<1 to 3 mm	H	Protogranular	Ol, Opx, Cpx, Sp + Amph	Hzb	2 <sup>ndary</sup>	Vein	Ol, Cpx, Sp	Broken-down Cpx at melt contact. Sp are enclosed in minerals (Poikilitic features). Little destabilization of Amph
MSZK1308	7 cm	<1 to 5 mm	H	Protogranular + Poikilitic features	Ol, Opx, Cpx, Sp	Lz	2 <sup>ndary</sup>	Vein	Ol, Cpx, Sp	Gl (S) in melt and sometimes associated with FI

Table 1: Petrographic description of BBHVF mantle xenoliths. H- heterogranular, E- equigranular, Lz- Lherzolite, Hzb- Harzburgite, 2ndary- trails of secondary fluid inclusions, Gl (s)- sulfide globule.

**Table2**  
[Click here to download Table: Table 2.doc](#)

Olivine																															
Sample	SZB16		SZB44		SZB50		SZB51		SZB52		SZB66		SZG14		SZG23		SZG30		SZG44		FT12		FT01P		FT08P		MSZK1306A		MSZK1308		
n=	8	1σ	3	1σ	2	1σ	4	1σ	4	1σ	3	1σ	6	1σ	3	1σ	4	1σ	4	1σ	4	1σ	2	1σ	6	1σ	2	1σ	4	1σ	
SiO <sub>2</sub>	40,97	0,21	40,9	0,24	40,43	0,27	41,56	0,15	40,84	0,3	41,04	0,09	41,05	0,22	40,8	0,47	41,47	0,34	41,26	0,3	40,96	0,23	42,09	0,12	41,56	0,17	41,31	0,41	41,39	41,39	
TiO <sub>2</sub>	0,02	0,02	0,01	0,01	0	0	0,01	0,01	0,02	0,03	0	0	0,01	0,01	0	0,01	0,02	0,02	0,02	0,02	0	0	0,01	0,01	0	0	0	0	0,01	0,01	
Al <sub>2</sub> O <sub>3</sub>	0,05	0,03	0,03	0,02	0,1	0,08	0,03	0,02	0,04	0,01	0,03	0,01	0,06	0,03	0,06	0,04	0,03	0,02	0,03	0,02	0,02	0,02	0,05	0,01	0,02	0,03	0,01	0	0,04	0,04	
Cr <sub>2</sub> O <sub>3</sub>	0,02	0,02	0,03	0,05	0,01	0,01	0,07	0,08	0,07	0,04	0,06	0,04	0,03	0,04	0,05	0,02	0,02	0,04	0,04	0,05	0,02	0,01	0,04	0,01	0,03	0,04	0,02	0,01	0,03	0,03	
FeO	10,19	0,1	10,78	0,1	10,68	0,05	9,5	0,13	9,24	0,13	9,74	0,29	10,31	0,12	9,93	0,13	10,04	0,09	10,37	0,1	10,45	0,17	9,28	0,1	9,56	0,09	9,22	0,08	9,43	9,43	
MnO	0,13	0,03	0,13	0,04	0,12	0,03	0,12	0,01	0,14	0,01	0,12	0,02	0,15	0,03	0,15	0,04	0,13	0,01	0,15	0,02	0,15	0,02	0,15	0,03	0,14	0,02	0,13	0,02	0,13	0,13	
NiO	0,36	0,03	0,35	0,02	0,36	0,02	0,35	0,02	0,36	0,02	0,4	0,02	0	0	0	0	0	0	0	0	0	0	0	0	0	0	0	0	0	0	
MgO	48,77	0,13	48,16	0,25	48,06	0,03	49,08	0,12	48,99	0,24	48,59	0,22	48,35	0,12	48,17	0,08	48,37	0,21	48,17	0,15	48,22	0,47	48,78	0,01	49,54	0,29	49,98	0,15	49,31	49,31	
CaO	0,09	0,01	0,07	0,01	0,05	0	0,07	0,01	0,12	0,03	0,08	0,01	0,12	0,01	0,11	0,08	0,06	0,01	0,08	0,01	0,05	0,01	0,1	0,02	0,06	0,03	0,04	0,01	0,09	0,09	
Na <sub>2</sub> O	0,02	0,01	0,01	0,01	0	0	0,01	0,01	0,01	0,01	0,01	0,01	0,02	0,02	0,01	0	0,01	0	0,02	0,01	0	0	0,01	0,01	0,01	0,01	0	0	0,01	0,01	
K <sub>2</sub> O	0	0	0	0	0	0	0,01	0,01	0	0,01	0	0,01	0	0	0	0	0	0,01	0,01	0,01	0	0	0	0	0	0	0	0	0	0,01	0,01
V <sub>2</sub> O <sub>3</sub>	0	0	0	0	0	0	0	0	0	0	0	0	0,35	0,04	0,34	0,03	0,35	0,03	0,34	0,04	0,36	0,03	0,37	0,01	0,38	0,02	0,38	0,02	0,37	0,37	
Total	100,62	0,3	100,47	0,21	99,81	0,07	100,81	0,17	99,83	0,44	100,08	0,38	100,45	0,21	99,62	0,37	100,51	0,28	100,48	0,31	100,25	0,27	100,87	0,23	101,3	0,31	101,1	0,64	100,82	100,82	
mg#	89,51	0,09	88,85	0,12	88,92	0,04	90,21	0,11	90,43	0,1	89,89	0,26	89,32	0,11	89,64	0,14	89,19	0,26	89,23	0,07	89,16	0,22	90,36	0,09	90,23	0,09	90,63	0,05	90,31	90,31	

Opx																														
Sample	SZB16		SZB44		SZB50		SZB51		SZB52		SZB66		SZG14		SZG23		SZG30		SZG44		FT12		FT01P		FT08P		MSZK1306A		MSZK1308	
n=	7	1σ	3	1σ	5	1σ	4	1σ	2	1σ	3	1σ	7	1σ	3	1σ	4	1σ	3	1σ	3	1σ	4	1σ	5	1σ	3	1σ	5	1σ
SiO <sub>2</sub>	54,21	0,48	55,41	0,76	55,23	0,19	56,62	33,45	55,45	1,15	56,19	0,2	54,91	0,29	55,25	0,54	55,34	0,45	54,92	0,23	55,17	0,21	56,55	0,23	56,45	0,27	56,82	0,43	55,44	0,23
TiO <sub>2</sub>	0,15	0,02	0,09	0,02	0,1	0,03	0,04	33,45	0,06	0,02	0,04	0,02	0,16	0,03	0,09	0,05	0,14	0,04	0,16	0,01	0,08	0,03	0,09	0,03	0,04	0,03	0,03	0,04	0,12	0,03
Al <sub>2</sub> O <sub>3</sub>	5,7	0,09	4,59	0,14	4,5	0,06	2,8	33,45	5,04	0,19	3,12	0,06	5,18	0,16	3,98	0,22	4,84	0,09	5,12	0,07	4,26	0,07	3,33	0,05	3,48	0,07	2,61	0,07	5,08	0,07
Cr <sub>2</sub> O <sub>3</sub>	0,44	0,05	0,29	0,02	0,24	0,03	0,61	33,45	0,57	0,01	0,61	0,05	0,34	0,04	0,59	0,03	0,4	0,03	0,37	0,03	0,29	0,04	0,8	0,04	0,34	0,04	0,35	0,05	0,5	0,03
FeO	6,52	0,12	6,76	0,16	6,91	0,13	5,98	3,05	5,81	0,12	6,3	0,05	6,47	0,13	6,49	0,19	6,34	0,14	6,57	0,05	6,79	0,1	5,81	0,12	6,34	0,07	6,08	0,12	5,91	0,1
MnO	0,1	0,03	0,14	0,03	0,13	0,05	0,11	33,45	0,13	0,03	0,14	0,04	0,12	0,03	0,13	0,03	0,13	0,03	0,13	0,03	0,14	0,02	0,09	0,01	0,14	0,03	0,13	0,02	0,11	0,03
NiO	0,09	0,04	0,08	0,01	0,09	0,02	0,08	0,46	0,1	0,02	0,1	0,02	0,01	0	0,01	0	0,02	0,01	0,01	0	0,01	0,01	0,02	0	0,01	0	0,01	0	0,01	0
MgO	31,62	0,41	32,2	0,5	32,35	0,12	33,24	33,45	31,98	0,14	32,77	0,09	31,94	0,22	32,08	0,44	32,29	0,19	31,93	0,16	32,48	0,08	32,38	0,22	33,74	0,16	34,28	0,17	32,51	0,13
CaO	1,03	0,02	0,75	0,08	0,68	0,02	0,81	33,45	1,12	0,01	0,89	0,03	0,88	0,1	0,84	0,03	0,78	0,02	0,83	0,03	0,69	0,03	1,17	0,05	0,6	0,02	0,6	0,01	0,93	0,02
Na <sub>2</sub> O	0,18	0,01	0,06	0,01	0,07	0,00	0,06	33,45	0,09	0,01	0,02	0,01	0,15	0,02	0,16	0,01	0,11	0,01	0,15	0,01	0,05	0,01	0,13	0,01	0,02	0,01	0,02	0,03	0,12	0,01
K <sub>2</sub> O	0,01	0,01	0,01	0,01	0,01	0,01	0	33,45	0,01	0,01	0	0,01	0,01	0,01	0	0	0	0	0,01	0,01	0	0	0	0	0,01	0,01	0	0,01	0	0
V <sub>2</sub> O <sub>3</sub>	0,02	0	0,01	0,01	0,02	0,00	0,01	33,45	0,01	0	0,02	0	0,09	0,02	0,08	0,01	0,09	0,01	0,09	0,01	0,09	0	0,1	0,02	0,09	0,02	0,09	0,02	0,1	0,02
Total	100,06	0,84	100,4	0,42	100,33	0,29	100,36	4,96	100,38	1,47	100,19	0,35	100,28	0,35	99,7	0,32	100,48	0,67	100,29	0,21	100,07	0,27	100,47	0,31	101,27	0,25	101,03	0,5	100,84	0,29
mg#	89,62	0,17	89,47	0,19	89,3	0,16	90,83	38,44	90,75	0,15	90,27	0,08	89,8	0,17	89,81	0,37	90,08	0,2	89,65	0,1	89,5	0,12	90,85	0,17	90,46	0,1	90,96	0,17	90,74	0,12

Cpx																																
Sample	SZB16		SZB44		SZB50		SZB51		SZB52		SZB66		SZG14		SZG23		SZG30		SZG44		FT12		FT01P		FT08P		MSZK1306A		MSZK1308			
n=	9	1 $\sigma$	3	1 $\sigma$	5	1 $\sigma$	4	1 $\sigma$	3	1 $\sigma$	3	1 $\sigma$	7	1 $\sigma$	4	1 $\sigma$	3	1 $\sigma$	3	1 $\sigma$	3	1 $\sigma$	2	1 $\sigma$	4	1 $\sigma$	4	1 $\sigma$	6	1 $\sigma$		
SiO <sub>2</sub>	51,55	0,21	52,10	0,22	52,39	0,33	53,73	0,30	51,99	0,27	53,01	0,46	51,65	0,68	51,88	0,70	52,25	0,34	51,93	0,20	52,32	0,29	53,97	0,36	53,34	0,32	53,83	0,18	52,25	0,23		
TiO <sub>2</sub>	0,59	0,06	0,37	0,03	0,34	0,01	0,06	0,03	0,17	0,01	0,06	0,02	0,66	0,14	0,40	0,14	0,49	0,05	0,62	0,05	0,32	0,03	0,22	0,01	0,14	0,03	0,05	0,03	0,46	0,03		
Al <sub>2</sub> O <sub>3</sub>	7,38	0,54	5,65	0,07	5,69	0,06	3,36	0,09	5,84	0,05	3,32	0,06	7,54	0,27	6,13	0,24	6,84	0,12	7,40	0,07	5,38	0,05	4,12	0,01	3,36	0,14	2,29	0,05	6,70	0,06		
Cr <sub>2</sub> O <sub>3</sub>	0,81	0,04	0,47	0,02	0,44	0,04	1,07	0,08	1,03	0,04	0,86	0,07	0,70	0,03	1,23	0,07	0,77	0,03	0,71	0,03	0,51	0,06	1,41	0,09	0,40	0,06	0,35	0,05	0,93	0,05		
FeO	3,44	0,11	3,08	0,08	3,04	0,05	2,81	0,03	2,96	0,08	3,03	0,09	3,17	0,29	3,31	0,14	2,93	0,05	3,25	0,09	2,87	0,07	3,03	0,05	2,56	0,04	2,57	0,02	2,99	0,06		
MnO	0,08	0,02	0,07	0,02	0,07	0,02	0,04	0,02	0,04	0,02	0,04	0,02	0,04	0,03	0,08	0,03	0,03	0,01	0,05	0,02	0,07	0,01	0,06	0,01	0,04	0,03	0,06	0,02	0,06	0,02	0,07	0,01
NiO	0,05	0,03	0,06	0,02	0,04	0,01	0,04	0,01	0,06	0,01	0,06	0,02	0,04	0,00	0,04	0,01	0,04	0,00	0,04	0,00	0,03	0,00	0,03	0,00	0,03	0,00	0,02	0,00	0,03	0,01		
MgO	15,46	0,37	15,71	0,05	15,65	0,15	16,90	0,09	16,41	0,13	16,91	0,32	15,20	0,29	14,96	0,11	15,35	0,10	14,86	0,09	15,70	0,07	16,80	0,16	16,74	0,31	17,51	0,11	15,69	0,06		
CaO	18,53	0,93	20,80	0,16	20,71	0,06	20,90	0,19	19,50	0,41	21,17	0,53	18,76	0,44	19,16	0,20	19,59	0,29	18,84	0,17	21,28	0,15	19,19	0,16	22,63	1,77	23,52	0,08	19,58	0,33		
Na <sub>2</sub> O	1,61	0,37	1,09	0,02	1,07	0,01	0,85	0,01	0,98	0,01	0,44	0,01	1,77	0,14	1,78	0,06	1,62	0,03	1,85	0,05	1,00	0,02	1,14	0,04	0,40	0,04	0,30	0,04	1,52	0,03		
K <sub>2</sub> O	0,02	0,03	0,01	0,01	0,00	0,00	0,00	0,00	0,01	0,00	0,00	0,00	0,00	0,00	0,01	0,00	0,00	0,00	0,00	0,00	0,00	0,00	0,00	0,00	0,00	0,00	0,01	0,01	0,01	0,01		
V <sub>2</sub> O <sub>5</sub>	0,04	0,01	0,03	0,00	0,03	0,00	0,04	0,00	0,04	0,00	0,04	0,01	0,04	0,01	0,04	0,02	0,04	0,01	0,03	0,01	0,03	0,02	0,04	0,02	0,04	0,02	0,04	0,02	0,03	0,03		
Total	99,55	0,30	99,44	0,32	99,48	0,47	99,80	0,13	99,03	0,26	98,93	1,16	99,61	0,67	98,97	0,50	99,97	0,33	99,60	0,31	99,49	0,41	99,98	0,05	99,72	2,03	100,56	0,21	100,27	0,17		
mg#	88,91	0,45	90,09	0,24	90,18	0,13	91,48	0,10	90,81	0,28	90,87	0,20	89,55	0,69	88,97	0,42	90,32	0,16	89,08	0,25	90,69	0,22	90,82	0,21	92,11	0,17	92,40	0,07	90,36	0,18		

Sp																														
Sample	SZB16		SZB44		SZB50		SZB51		SZB52		SZB66		SZG14		SZG23		SZG30		SZG44		FT12		FT01P		FT08P		MSZK1306A		MSZK1308	
n=	8	1 $\sigma$	4	1 $\sigma$	4	1 $\sigma$	5	1 $\sigma$	4	1 $\sigma$	4	1 $\sigma$	11	1 $\sigma$	5	1 $\sigma$	1	1 $\sigma$	6	1 $\sigma$	5	1 $\sigma$	2	1 $\sigma$	7	1 $\sigma$	1	1 $\sigma$	4	1 $\sigma$
SiO <sub>2</sub>	0,11	0,02	0,06	0,01	0,07	0,01	0,63	1,30	0,07	0,02	0,12	0,11	0,10	0,03	0,06	0,03	0,06	-	0,07	0,02	0,05	0,02	0,08	0,02	0,03	0,03	0,01	-	0,06	0,02
TiO <sub>2</sub>	0,22	0,03	0,10	0,00	0,08	0,03	0,10	0,01	0,10	0,03	0,09	0,03	0,26	0,02	0,20	0,03	0,12	-	0,17	0,02	0,09	0,01	0,35	0,03	0,06	0,01	0,07	-	0,18	0,01
Al <sub>2</sub> O <sub>3</sub>	57,18	0,50	58,74	0,44	59,15	0,56	31,24	0,29	50,58	0,35	31,87	0,20	58,34	0,34	43,81	1,44	57,00	-	58,17	0,23	57,63	0,54	30,80	0,03	51,08	0,48	36,38	-	54,09	0,34
Cr <sub>2</sub> O <sub>3</sub>	9,77	0,14	8,30	0,25	7,77	0,34	35,40	0,46	16,72	0,20	31,20	0,73	8,62	0,14	21,63	1,34	10,62	-	8,72	0,21	9,44	0,24	35,92	0,14	15,83	0,39	28,07	-	13,50	0,24
FeO	11,46	0,22	11,58	0,10	11,42	0,18	15,72	0,36	10,79	0,12	18,41	0,76	10,68	0,15	14,71	0,42	10,78	-	11,52	0,13	11,40	0,18	15,42	0,20	12,48	0,64	17,86	-	10,83	0,27
MnO	0,00	0,00	0,00	0,00	0,00	0,00	0,00	0,00	0,00	0,00	0,00	0,00	0,00	0,00	0,00	0,00	0,00	-	0,00	0,00	0,00	0,00	0,00	0,00	0,00	0,00	0,00	-	0,00	0,00
NiO	0,39	0,02	0,38	0,02	0,39	0,02	0,20	0,03	0,33	0,03	0,26	0,03	0,06	0,00	0,08	0,00	0,07	-	0,06	0,00	0,06	0,00	0,14	0,00	0,08	0,00	0,17	-	0,07	0,00
MgO	20,59	0,14	20,16	0,11	20,16	0,06	15,50	0,23	19,61	0,24	15,90	0,67	21,06	0,17	18,08	0,24	20,68	-	20,62	0,11	20,10	0,21	16,26	0,03	19,32	0,54	16,47	-	20,52	0,05
CaO	0,00	0,00	0,01	0,01	0,00	0,00	0,04	0,08	0,01	0,00	0,00	0,00	0,01	0,01	0,00	0,00	0,01	-	0,00	0,00	0,00	0,00	0,00	0,00	0,01	0,01	0,02	-	0,00	0,00
Na <sub>2</sub> O	0,01	0,01	0,01	0,01	0,01	0,01	0,06	0,11	0,01	0,01	0,01	0,01	0,01	0,01	0,01	0,02	0,01	-	0,01	0,01	0,00	0,01	0,00	0,00	0,01	0,01	0,02	-	0,01	0,01
K <sub>2</sub> O	0,00	0,01	0,00	0,01	0,02	0,02	0,02	0,04	0,01	0,01	0,01	0,01	0,00	0,00	0,00	0,00	0,00	-	0,00	0,00	0,00	0,00	0,00	0,00	0,00	0,00	0,00	-	0,01	0,01
V <sub>2</sub> O <sub>5</sub>	0,07	0,00	0,06	0,01	0,06	0,00	0,16	0,01	0,08	0,00	0,20	0,00	0,38	0,03	0,33	0,02	0,38	-	0,36	0,03	0,36	0,03	0,27	0,02	0,31	0,03	0,25	-	0,35	0,03
Total	99,80	0,37	99,40	0,12	99,13	0,17	99,06	0,54	98,28	0,20	98,07	0,87	99,52	0,53	98,92	0,36	99,73	-	99,69	0,39	99,13	0,29	99,24	0,31	99,19	0,62	99,33	-	99,63	0,25
mg#	76,21	0,36	75,62	0,12	75,88	0,26	63,73	0,44	76,41	0,37	60,62	1,92	77,85	0,17	68,66	0,85	77,37	-	76,14	0,16	75,86	0,30	65,27	0,33	73,40	1,47	62,18	-	77,16	0,45
cr#	10,28	0,19	8,66	0,29	8,10	0,39	43,18	0,22	18,15	0,22	39,63	0,47	9,02	0,12	24,89	1,78	11,11	-	9,14	0,22	9,90	0,31	43,89	0,07	17,21	0,40	34,11	-	14,34	0,29

Table 2: Major element composition of primary olivines, orthopyroxenes, clinopyroxènes and spinels (in wt. %).



**Table4**  
[Click here to download Table: Table 4.doc](#)

Cpx I																				
Sample	SZB16		SZB44		SZB50		SZB51		SZB52		SZB66		SZG14		SZG23		SZG30		SZG44	
n=	8	σ	7	σ	5	σ	5	σ	7	σ	6	σ	9	σ	7	σ	7	σ	9	σ
Al27	39514	1903	29057	266	29096	346	17205	290	3265	687	16571	437	41315	1290	33800	1324	36597	1011	40524	1344
Ca44	132416	6614	148566	1273	147672	506	149330	1381	19,7	0,4	149337	3395	18,8	0,44	19,1	0,22	19,6	0,3	18,8	0,16
Sc45	57,2	2,54	58,5	0,82	59,2	0,39	81,81	1,12	53	1,64	61,2	1,84	61,8	2,45	69,4	1,68	64,0	1,87	66	1,63
Ti49	3486	177	2236	35,5	2195,39	28,3	317	2,07	1103	17,9	366	10,1	4112	414	2742	549	3561	73,4	4224	136
V51	125	9,98	158	5,36	161	3,32	nd	nd	nd	nd	53,7	24,5	160	4,68	nd	nd	142	4	165	10,5
Cr52	4862	330	3153	38,8	2911	71,7	nd	nd	nd	nd	3381	1143	4982	182	nd	nd	5375	185	5088	140
Cr53	5136	292	3287	65,8	2991	80,9	6841	358	7259	195	5414	164	5103	183	8815	274	5545	183	5234	134
Mn55	771	41,9	698	4,94	695	11,7	643	13,6	714	22,2	645	17	718	32,3	743	14,9	691	14,7	726	28,1
Co59	25,6	1,44	23,5	0,15	22,9	0,55	23,2	0,67	26,3	0,79	24,5	0,67	23,05	1,17	22,9	0,4	22,3	0,61	22,4	0,7
Ni60	409	23,3	367	3,37	358	7,3	370	11,0	433	11,6	410	11,5	358	17,5	366	6,14	350	11,8	336	8,96
Rb85	nd	nd	nd	nd	nd	nd	nd	nd	nd	nd	nd	nd	nd	nd	nd	nd	nd	nd	nd	nd
Sr88	64,3	4,55	nd	nd	67,75	1,16	105,96	0,78	23,12	1,12	62,4	0,98	77,01	2,9	154,64	34,11	71,2	0,95	nd	nd
Y89	18,1	0,85	17,0	0,37	16,88	0,11	3,07	0,05	8,75	0,22	3,02	0,11	18,67	0,53	15,98	0,49	17,07	0,81	18,61	0,31
Zr90	28,0	1,68	30	0,57	29,42	0,14	9,62	0,34	9,4	0,29	8,58	0,31	33,93	1,66	35,99	2,89	27,46	1,14	34,78	1,01
Nb93	0,19	0,09	0,08	0,01	0,08	0,01	0,12	0,02	nd	nd	0,28	0,02	nd	nd	nd	nd	nd	nd	nd	nd
Ba135	nd	nd	nd	nd	nd	nd	nd	nd	nd	nd	nd	nd	nd	nd	nd	nd	nd	nd	nd	nd
Ba137	0,08	0,02	nd	nd	nd	nd	0,08	0,05	0,43	0,67	nd	nd	nd	nd	nd	nd	nd	nd	nd	nd
La139	0,71	0,15	3	0,04	3	0,03	3,43	0,04	0,94	0,03	1,16	0,05	1,3	0,43	7,44	2,37	1,33	0,03	1,28	0,22
Ce140	2,95	0,26	9,61	0,14	9,35	0,18	5,27	0,2	2,71	0,12	2,35	0,05	4,4	1,32	20,88	6,61	4,36	0,14	4,8	0,17
Pr141	0,61	0,04	1,67	0,02	1,64	0,02	0,44	0,02	0,4	0,01	0,31	0,01	0,78	0,19	2,74	0,85	0,74	0,02	0,84	0,05
Nd146	3,96	0,24	8,25	0,65	8,41	0,08	1,43	0,04	1,97	0,04	1,38	0,04	4,66	0,82	11,92	3,36	4,25	0,1	4,89	0,13
Sm147	1,7	0,09	2,34	0,08	2,34	0,04	0,29	0,02	0,62	0,03	0,35	0,01	1,77	0,18	2,73	0,52	1,58	0,04	1,83	0,05
Eu151	0,69	0,04	0,8	0,07	0,81	0,02	0,12	0,01	0,23	0,01	0,13	0,01	0,72	0,04	1	0,15	0,65	0,02	0,71	0,02
Eu153	0,69	0,04	0,81	0,02	0,8	0,02	0,12	0	0,23	0,01	0,14	0	0,72	0,05	1,01	0,15	0,66	0,02	0,71	0,02
Gd157	2,55	0,16	2,77	0,08	2,68	0,03	0,36	0,02	0,97	0,04	0,38	0,03	2,64	0,15	3,03	0,19	2,42	0,11	2,62	0,1
Tb159	0,48	0,02	0,46	0,04	0,46	0,01	0,06	0	0,18	0,01	0,07	0	0,48	0,02	0,49	0,02	0,43	0,02	0,47	0,01
Dy163	3,23	0,14	3,16	0,09	3,11	0,07	0,48	0,03	1,48	0,04	0,5	0,02	3,47	0,12	3,27	0,09	3,11	0,12	3,39	0,09
Ho165	0,7	0,03	0,66	0,02	0,66	0,01	0,12	0	0,34	0,01	0,12	0,01	0,75	0,02	0,63	0,02	0,67	0,03	0,72	0,02
Er166	2,03	0,11	1,92	0,04	1,88	0,03	0,4	0,01	1,04	0,02	0,39	0,01	2,15	0,06	1,7	0,05	1,92	0,08	2,09	0,04
Tm169	0,28	0,02	0,26	0,01	0,26	0,01	0,06	0	0,16	0,01	0,06	0	0,31	0,01	0,23	0,01	0,27	0,01	0,3	0,01
Yb172	1,81	0,09	1,74	0,07	1,71	0,04	0,48	0,03	1,07	0,03	0,44	0,03	2,07	0,04	1,51	0,06	1,79	0,1	2,01	0,06
Lu175	0,26	0,01	0,24	0,01	0,25	0	0,08	0	0,15	0,01	0,07	0	0,29	0,01	0,2	0,01	0,25	0,01	0,29	0,01
Hf178	0,95	0,05	1,01	0,02	1,01	0,03	0,33	0,03	0,26	0,01	0,28	0,01	1,13	0,1	1,03	0,04	0,91	0,03	1,07	0,04
Ta181	nd	nd	nd	nd	0,01	0	0,01	0	0,02	0,01	0,03	0	0,03	0,01	0,01	0,01	0,02	0	nd	nd
Pb208	0,05	0,01	nd	nd	0,3	0,01	0,37	0,02	nd	nd	0,65	0,03	nd	nd	0,28	0,08	0,09	0,02	nd	nd
Th232	0,03	0,01	0,35	0,01	0,35	0,01	0,37	0,01	0,1	0,01	0,07	0,01	0,05	0,01	0,36	0,06	0,05	0	nd	nd
U238	nd	nd	0,08	0,02	0,09	0	0,08	0,01	0,04	0	0,03	0	0,02	0,01	0,06	0,01	0,02	0	nd	nd

Cpx I										
Sample	FT12		FT01P		FT08P		MSZK1306A		MSZK1308	
n=	10	$\sigma$	3	$\sigma$	6	$\sigma$	6	$\sigma$	7	$\sigma$
Al27	29735	270	22038	1370	18680	1451	13082	518	36909	677
Ca44	152067	1114	137103	1155	161737	12647	168074	596	139918	2328
Sc45	61,3	1,15	56,4	2,18	53,1	3,59	66,3	1,26	63,5	1,27
Ti49	2016	48,3	1348	266	842	74,2	459	11,7	3130	51,1
V51	179	4,91	nd	nd	122	9,9	149	3,84	148	4,94
Cr52	3658	91,1	nd	nd	2982	318	2541	560	6530	245
Cr53	3752	90,6	9920	595	3020	323	2687	602	6864	204
Mn55	674	5,23	688	36,0	617	52	601	14,4	685	14,3
Co59	22,2	0,31	26,1	0,62	21,1	1,94	22,0	0,53	23,4	0,58
Ni60	352	4,05	413	15,6	339	31,2	372	10,5	376	9,58
Rb85	nd	nd	nd	nd	nd	nd	nd	nd	nd	nd
Sr88	109	3,31	88,3	35,5	136	8,27	38,4	0,95	59,8	2,29
Y89	14,6	0,29	6,09	0,73	7,75	0,56	3,45	0,08	15,4	0,31
Zr90	20,6	0,52	16,2	6,29	11,0	1,08	6,49	0,35	23,1	0,42
Nb93	0,21	0,03	1,44	0,32	0,09	0,01	0,12	0,03	0,38	0,01
Ba135	nd	nd	nd	nd	nd	nd	nd	nd	nd	nd
Ba137	nd	nd	0,1	0,03	0,1	0,04	0,04	0,01	nd	nd
La139	13,7	0,41	3,41	1,09	38,5	2,93	2,83	0,06	0,98	0,03
Ce140	36,0	1,13	8,09	2,79	45,4	3,44	6,62	0,35	3,17	0,07
Pr141	4,27	0,15	1,07	0,39	3,68	0,27	0,77	0,07	0,55	0,02
Nd146	15,9	0,5	5,14	1,83	11,5	0,93	2,94	0,24	3,38	0,1
Sm147	2,71	0,07	1,29	0,38	1,66	0,11	0,51	0,05	1,36	0,08
Eu151	0,8	0,03	0,46	0,12	0,44	0,04	0,14	0,01	0,53	0,02
Eu153	0,78	0,02	0,46	0,12	0,43	0,04	0,15	0,02	0,52	0,01
Gd157	2,53	0,1	1,38	0,36	1,37	0,11	0,45	0,03	2,06	0,07
Tb159	0,39	0,02	0,21	0,04	0,21	0,01	0,07	0,01	0,37	0,01
Dy163	2,62	0,11	1,28	0,18	1,37	0,09	0,57	0,04	2,73	0,1
Ho165	0,55	0,02	0,24	0,03	0,29	0,02	0,13	0,01	0,58	0,02
Er166	1,55	0,05	0,63	0,07	0,84	0,05	0,42	0,02	1,66	0,05
Tm169	0,23	0,01	0,08	0,01	0,13	0,01	0,07	0	0,23	0,01
Yb172	1,47	0,06	0,51	0,03	0,86	0,06	0,51	0,02	1,49	0,06
Lu175	0,21	0,01	0,07	0	0,13	0,01	0,07	0	0,21	0,01
Hf178	0,77	0,04	0,49	0,12	0,23	0,03	0,19	0,02	0,79	0,03
Ta181	0,02	0	0,16	0,07	0,02	0	0,02	0	0,03	0
Pb208	1,58	0,08	0,06	0,02	5,42	0,57	0,17	0,02	nd	nd
Th232	2,53	0,18	0,32	0,08	6,71	0,76	0,21	0,02	0,03	0,01
U238	0,36	0,03	0,07	0,01	1,77	0,18	0,04	0,01	nd	Nd

Amphibole				
Sample	FT08P		MSZK1306A	
N=	5	$\sigma$	6	$\sigma$
Al27	68264	785	59474	965
P31	nd	nd	nd	nd
Ca44	71470	0	71470	0
Sc45	58,3	1,27	82,6	1,88
Ti49	3607	83,2	1826	28,3
V51	193	17,8	102	52,18
Cr52	6859	427	4545	1802
Cr53	7324	195	9683	236
Mn55	370	8,53	323	3,03
Co59	34,2	1,29	32,7	0,42
Ni60	759	25,6	781	13,9
Rb85	16,7	1,53	12,3	1,22
Sr88	492	18,8	112	2,82
Y89	16,1	0,35	7,97	0,27
Zr90	20,3	0,45	15,6	0,19
Nb93	10,7	0,33	14,1	0,21
Ba135	912	44,0	235	24,4
Ba137	915	43,3	234	25,4
La139	72,1	2,44	6,69	0,21
Ce140	83,4	3,17	16,0	0,26
Pr141	6,68	0,27	1,89	0,09
Pr141	nd	nd	nd	nd
Nd146	20,8	0,63	7,45	0,52
Sm147	3,14	0,15	1,21	0,08
Eu151	0,88	0,05	0,35	0,01
Eu153	0,85	0,02	0,34	0,01
Gd157	2,77	0,11	1,08	0,05
Tb159	0,4	0,01	0,16	0
Dy163	2,77	0,09	1,25	0,05
Ho165	0,59	0,03	0,31	0,01
Er166	1,75	0,02	0,96	0,04
Tm169	0,25	0,01	0,15	0,01
Yb172	1,64	0,07	1,08	0,04
Lu175	0,25	0,01	0,16	0,01
Hf178	0,41	0,03	0,42	0,02
Ta181	0,34	0,02	0,77	0,04
Pb208	28,4	1,25	0,61	0,02
Th232	14,5	0,5	0,62	0,04
U238	3,16	0,13	0,1	0,01

Table 4: Primary Cpx and amphiboles trace element compositions (in ppm).

Table5

[Click here to download Table: Table 5.doc](#)

Glass																					
	SZB16			SZB44			SZB50			SZB51			SZB51			SZB52			SZB66		
	Vein		MP	MP		MP	MP		MP	Vein		Vein		Vein		Vein		Vein		MP	
	8	Min	Max	10	Min	Max	4	Min	Max	3	Min	Max	4	Min	Max	6	Min	Max	6	Min	Max
SiO <sub>2</sub>	56,55	55,82	57,60	54,16	53,39	54,81	55,43	55,28	55,87	56,63	56,63	56,63	61,89	60,53	62,71	57,87	56,52	59,02	60,86	59,55	61,50
TiO <sub>2</sub>	1,57	1,46	1,69	1,72	1,67	1,84	1,71	1,62	1,73	0,43	0,43	0,43	0,14	0,07	0,19	0,75	0,52	0,99	1,29	1,21	1,41
Al <sub>2</sub> O <sub>3</sub>	19,15	18,82	19,51	20,79	20,20	21,28	20,60	20,52	20,86	22,55	22,55	22,55	18,57	18,54	18,66	20,37	19,96	20,95	18,04	18,02	18,11
FeO	3,85	3,28	4,34	3,99	3,69	4,49	3,82	3,67	3,88	2,89	2,89	2,89	2,88	2,80	3,01	3,11	2,97	3,28	3,06	2,99	3,14
MnO	0,06	0,01	0,09	0,08	0,05	0,11	0,06	0,05	0,06	0,07	0,07	0,07	0,04	0,00	0,07	0,07	0,01	0,13	0,08	0,05	0,12
MgO	3,57	3,49	3,73	4,59	4,29	4,86	4,33	4,20	4,38	3,23	3,23	3,23	2,56	2,46	2,70	3,37	3,16	3,49	3,08	2,91	3,30
CaO	7,88	7,47	8,25	9,89	9,55	10,08	9,19	8,34	9,47	7,66	7,66	7,66	4,82	4,50	5,45	7,79	7,64	7,90	5,88	5,70	6,12
Na <sub>2</sub> O	4,12	3,97	4,21	4,05	4,03	4,10	4,32	4,16	4,38	5,50	5,50	5,50	5,58	5,48	5,66	4,13	3,92	4,27	4,70	4,42	4,82
K <sub>2</sub> O	1,71	1,59	1,84	0,08	0,05	0,09	0,05	0,04	0,08	1,76	1,76	1,76	2,33	2,19	2,42	1,96	1,87	2,15	2,81	2,71	2,94
P <sub>2</sub> O <sub>5</sub>	0,45	0,38	0,52	0,05	0,01	0,07	0,01	0,01	0,03	0,24	0,24	0,24	1,10	0,98	1,15	0,50	0,48	0,54	0,94	0,92	0,94
Total	99,04	98,39	99,39	99,54	98,87	100,24	99,65	98,98	99,87	101,07	101,07	101,07	100,14	99,38	100,99	100,05	98,53	101,41	100,91	99,83	101,53
Mg#	62,35	59,58	65,48	67,25	64,57	68,71	66,89	66,81	67,12	66,58	66,58	66,58	61,33	60,57	62,69	65,83	64,99	66,39	64,14	63,13	65,98

	SZG14		SZG23		SZG44			FT12			FT01P			FT08P			
	Vein		SMI	MP	MP		MP		MP	Vein		Vein		MP			
	3	Min	6	Min	Max	8	Min	Max	9	Min	Max	8	Min	Max	6	Min	Max
SiO <sub>2</sub>	54,97	54,20	56,33	55,41	57,17	51,71	50,81	51,93	54,83	53,73	55,83	57,79	56,18	59,58	52,89	51,35	56,17
TiO <sub>2</sub>	1,74	1,74	1,52	1,27	1,88	2,72	2,45	3,21	1,64	1,60	1,69	1,76	1,58	2,03	0,80	0,72	0,93
Al <sub>2</sub> O <sub>3</sub>	20,63	22,89	20,16	19,46	20,87	20,40	19,58	21,15	20,43	19,55	21,06	17,56	16,99	18,37	22,90	21,62	23,75
FeO	3,47	3,34	3,60	3,42	4,07	3,82	3,62	4,15	3,62	3,01	4,89	2,67	2,47	2,94	3,67	3,02	4,25
MnO	0,11	0,01	0,08	0,00	0,14	0,08	0,04	0,12	0,05	0,03	0,10	0,04	-0,01	0,08	0,09	0,06	0,11
MgO	4,21	2,32	3,88	3,15	4,39	4,76	4,51	5,00	3,61	3,37	4,13	2,54	2,40	2,66	3,19	2,83	3,41
CaO	7,50	2,02	8,02	7,72	8,19	8,91	8,66	9,40	9,83	9,50	10,45	5,80	5,54	6,50	9,41	7,99	12,47
Na <sub>2</sub> O	5,10	7,31	4,93	4,80	5,09	5,17	4,79	5,45	5,15	4,65	5,55	4,82	4,59	5,20	5,25	4,53	5,81
K <sub>2</sub> O	1,85	5,26	0,90	0,57	1,19	0,63	0,40	0,77	0,26	0,21	0,33	4,55	3,18	5,87	0,95	0,34	1,38
P <sub>2</sub> O <sub>5</sub>	0,22	0,12	0,08	0,04	0,12	0,05	0,04	0,06	0,05	0,00	0,09	0,48	0,45	0,54	0,09	0,06	0,11
Total	99,92	99,39	99,58	99,02	100,26	98,30	97,83	98,81	99,56	99,06	100,09	98,15	97,60	98,76	99,65	98,92	100,91
Mg#	68,35	55,30	65,49	62,14	68,30	68,91	66,95	71,08	62,59	55,57	67,52	62,91	60,38	65,24	60,94	58,11	63,99

Table 5: Major element composition for glass in melt veins, melt pockets (MP) and silicate melt inclusions (SMI) (in wt. %).



Table6

[Click here to download Table: Table 6.doc](#)

Sample	SZB16		SZB44		SZB50		SZB51		SZB51		SZB52		SZB66	
Area	vein		MP		MP		MP		vein		vein		vein	
n=	8	$\sigma$	10	$\sigma$	4	$\sigma$	3	$\sigma$	4	$\sigma$	6	$\sigma$	6	$\sigma$
Al27	101040,49	1801,77	109676,54	1926,10	109303,43	872,20	119310,66	30,55	98308,24	300,94	107799,47	1762,47	95459,12	213,46
P31	1919,30	221,93	nd	nd	198,27	38,58	484,84	331,48	5565,36	1759,09	2104,08	114,06	4403,98	269,55
Ca44	55865,74	2544,66	109509,87	89709,17	65041,53	3400,12	294332,43	234191,99	39333,34	8606,68	53587,94	1822,67	40433,12	1783,61
Sc45	24,68	1,62	84,03	95,15	38,72	0,51	312,72	267,09	35,82	31,15	19,66	1,58	24,96	0,85
Ti49	10377,10	800,97	13640,90	5207,73	11042,95	338,57	4387,56	1514,70	1045,92	120,49	5367,87	546,38	9828,74	331,54
V51	183,45	17,29	370,93	217,85	213,71	13,45	428,35	289,10	112,91	45,77	110,80	3,86	159,98	4,87
Cr52	157,71	81,26	4547,71	8431,73	117,29	87,04	16977,90	12479,66	865,04	1392,96	251,48	300,36	103,46	16,08
Cr53	134,38	35,97	4783,44	8918,07	113,78	85,97	24251,49	22983,23	873,94	1378,29	262,08	324,38	107,17	17,17
Mn55	656,53	67,49	715,39	216,35	741,21	266,20	958,82	484,17	5717,65	9279,33	577,32	230,70	469,73	41,04
Co59	19,54	5,99	22,35	10,31	31,32	28,92	45,81	26,43	791,75	1347,95	25,33	28,65	10,09	2,06
Ni60	154,12	106,84	206,29	280,27	366,49	561,08	727,31	679,09	2172,06	625,64	297,97	570,17	43,75	34,36
Rb85	39,89	3,28	nd	nd	1,05	0,28	17,96	14,61	80,87	15,84	44,47	3,00	69,94	5,60
Sr88	557,77	29,91	205,35	74,44	237,71	9,28	486,64	183,18	1034,42	21,91	541,32	11,74	866,23	57,64
Y89	16,46	0,80	34,62	22,17	22,69	1,15	13,69	6,61	8,08	0,75	12,33	0,27	18,58	0,75
Zr90	139,74	11,47	35,61	3,29	34,49	2,29	71,45	15,15	378,02	21,36	134,38	3,21	259,74	14,04
Nb93	51,62	3,62	5,14	2,45	6,74	0,63	23,33	17,39	92,80	4,52	51,77	1,06	89,18	3,26
Cs133	0,49	0,06	nd	nd	0,05	0,01	nd	nd	1,99	0,33	0,59	0,05	0,99	0,10
Ba135	524,37	29,69	95,32	76,02	124,99	71,45	209,99	167,51	791,48	48,44	635,20	36,62	833,22	20,00
Ba137	526,16	29,32	95,66	76,93	124,30	69,88	211,34	166,13	791,05	25,30	632,61	34,98	830,98	15,27
La139	27,98	2,52	3,81	1,18	4,72	0,46	16,68	7,14	72,55	4,02	30,41	0,74	58,58	3,86
Ce140	53,10	4,52	12,46	2,00	12,83	0,42	27,71	6,85	112,40	4,12	54,64	1,11	100,46	2,32
Pr141	5,84	0,52	2,24	0,27	2,13	0,05	2,57	0,16	9,17	0,54	5,64	0,14	11,07	0,79
Nd146	22,58	2,51	12,41	3,26	11,33	0,30	8,80	1,18	25,30	4,03	20,64	0,99	39,95	2,40
Sm147	4,08	0,35	3,89	1,87	2,79	0,14	1,57	0,44	3,06	0,69	3,23	0,28	6,56	0,38
Eu151	1,34	0,08	1,39	0,71	0,99	0,10	0,60	0,15	0,89	0,30	0,99	0,10	1,97	0,12
Eu153	1,33	0,13	1,36	0,68	1,05	0,07	0,59	0,18	0,87	0,16	0,99	0,09	2,00	0,13
Gd157	3,73	0,40	5,11	3,14	3,26	0,23	1,78	0,73	nd	nd	2,67	0,22	4,99	0,29
Tb159	0,53	0,04	0,87	0,58	0,59	0,04	0,30	0,13	nd	nd	0,34	0,04	0,66	0,03
Dy163	3,28	0,24	6,41	4,25	4,01	0,20	2,13	0,96	nd	nd	2,26	0,12	3,74	0,27
Ho165	0,62	0,04	1,32	0,86	0,83	0,09	0,52	0,25	0,30	0,09	0,44	0,03	0,69	0,04
Er166	1,72	0,11	3,84	2,44	2,50	0,19	1,57	0,77	0,78	0,12	1,32	0,09	1,87	0,13
Tm169	0,25	0,02	0,55	0,35	0,35	0,02	0,26	0,14	0,16	0,09	0,18	0,02	0,26	0,02
Yb172	1,71	0,13	3,61	2,17	2,43	0,13	1,99	0,87	nd	nd	1,32	0,06	1,75	0,13
Lu175	0,25	0,02	0,49	0,25	0,36	0,01	0,29	0,12	0,18	0,07	0,19	0,01	0,25	0,01
Hf178	3,01	0,31	1,21	0,38	0,98	0,04	1,93	0,35	5,40	1,08	2,65	0,06	5,05	0,38
Ta181	3,03	0,29	0,22	0,09	0,24	0,03	1,19	0,80	6,08	0,47	3,03	0,17	5,39	0,27
Pb208	2,99	0,75	nd	nd	1,26	0,13	1,05	0,83	nd	nd	1,31	0,14	6,45	0,49
Th232	3,77	0,45	0,37	0,17	0,47	0,03	2,31	1,69	16,68	2,46	4,39	0,23	8,94	0,53
U238	1,15	0,15	nd	nd	0,14	0,03	0,58	0,50	5,12	0,54	1,32	0,06	2,59	0,17

Sample	SZG14		SZG14		SZG23		SZG44		FT12		FT01P		FT08P	
Area	vein		SMI		MP		MP		MP		vein		MP	
n=	1	$\sigma$	2	$\sigma$	6	$\sigma$	8	$\sigma$	9	$\sigma$	8	$\sigma$	6	$\sigma$
Al27	109184,34	-	120748,48	561,36	106873,28	4107,02	92149,11	27353,80	96488,23	28673,88	92956,22	2433,56	109978,23	26805,35
P31	1325,29	-	695,06	116,52	395,80	137,63	228,64	74,04	nd	nd	nd	nd	nd	nd
Ca44	48857,56	-	25493,42	347,92	55263,25	3220,70	50025,66	16068,89	51124,42	15685,12	39010,05	6080,18	87336,26	34620,34
Sc45	17,60	-	16,16	0,88	35,98	5,04	24,81	9,24	28,15	8,78	16,40	2,21	48,69	53,13
Ti49	11032,17	-	10232,71	2984,16	10372,61	748,18	15903,28	5672,20	9276,16	2734,51	12077,85	1369,54	5420,33	396,15
V51	108,41	-	106,48	2,80	247,47	60,32	228,88	84,38	231,67	74,98	159,65	16,94	311,34	111,38
Cr52	69,51	-	251,93	180,20	3351,20	5110,57	87,50	32,26	775,32	1873,72	70,50	17,10	2023,04	3415,28
Cr53	85,82	-	270,75	200,30	3549,59	5406,26	84,03	33,18	796,64	1925,38	73,07	16,51	2896,19	5262,64
Mn55	531,03	-	446,90	6,08	973,95	984,09	496,40	157,47	536,41	139,93	375,15	66,66	530,91	157,25
Co59	12,84	-	17,12	2,41	69,37	125,36	12,38	4,18	33,77	36,52	11,34	4,36	24,84	24,18
Ni60	37,19	-	53,88	14,28	1000,93	2196,28	39,20	18,03	712,91	1544,87	82,33	70,76	318,39	470,67
Rb85	26,33	-	35,87	6,05	6,28	1,99	4,52	2,06	5,56	1,48	63,00	4,46	18,90	8,82
Sr88	485,15	-	570,38	128,38	609,64	112,98	278,51	77,77	364,70	108,65	601,18	81,48	1067,74	455,20
Y89	15,51	-	11,04	0,31	18,52	2,94	18,76	6,13	18,83	5,68	13,46	1,61	22,92	2,97
Zr90	99,41	-	111,08	5,51	69,92	22,61	40,34	12,20	25,84	7,49	153,22	11,02	34,31	5,89
Nb93	45,24	-	54,40	9,67	23,89	9,47	11,24	3,96	23,33	6,92	59,35	6,18	24,64	10,91
Cs133	0,27	-	0,25	0,06	0,11	0,06	0,03	0,02	nd	nd	nd	nd	nd	nd
Ba135	380,70	-	414,13	117,80	187,31	39,59	60,52	34,04	322,11	96,39	603,80	30,84	2696,51	1232,56
Ba137	388,04	-	434,17	137,19	188,01	37,66	61,45	34,23	321,29	96,49	604,99	35,11	2691,62	1232,25
La139	9,37	-	6,71	1,56	17,56	6,21	2,32	0,70	21,52	6,47	33,15	4,81	151,07	58,82
Ce140	15,95	-	14,12	3,26	47,19	15,60	7,41	2,19	53,38	15,90	59,45	8,17	163,69	51,63
Pr141	1,67	-	1,36	0,09	5,68	1,47	1,16	0,35	6,11	1,85	6,44	0,78	12,21	3,13
Nd146	6,78	-	5,90	0,37	23,83	6,72	6,28	1,92	22,41	6,82	24,73	3,38	35,98	5,73
Sm147	1,81	-	1,57	0,13	4,60	1,32	2,02	0,66	3,58	1,09	4,27	0,79	4,72	0,35
Eu151	0,68	-	0,66	0,22	1,54	0,39	0,79	0,26	1,07	0,33	1,48	0,37	1,38	0,12
Eu153	0,78	-	0,63	0,16	1,58	0,45	0,78	0,25	1,06	0,32	1,53	0,22	1,40	0,13
Gd157	2,00	-	2,24	0,26	4,34	1,02	2,73	0,93	3,17	0,98	3,55	0,74	3,86	0,71
Tb159	0,40	-	0,33	0,16	0,58	0,14	0,46	0,14	0,48	0,15	0,50	0,08	0,58	0,10
Dy163	2,92	-	1,88	0,09	3,67	0,77	3,25	1,08	3,26	1,01	2,91	0,37	3,88	0,88
Ho165	0,57	-	0,44	0,04	0,68	0,11	0,70	0,23	0,69	0,21	0,54	0,12	0,82	0,15
Er166	1,43	-	1,19	0,15	1,85	0,23	2,05	0,65	2,01	0,61	1,33	0,16	2,54	0,38
Tm169	0,16	-	0,20	0,01	0,24	0,03	0,29	0,09	0,30	0,10	0,18	0,03	0,39	0,07
Yb172	1,51	-	0,99	0,11	1,60	0,26	2,01	0,66	2,14	0,67	1,18	0,23	2,72	0,28
Lu175	0,29	-	0,16	0,04	0,22	0,04	0,29	0,09	0,30	0,09	0,17	0,04	0,38	0,07
Hf178	2,11	-	2,25	0,31	1,23	0,33	1,01	0,33	0,83	0,25	3,52	0,36	0,61	0,10
Ta181	2,05	-	1,94	0,54	0,56	0,37	0,54	0,19	0,58	0,18	3,51	0,27	0,82	0,33
Pb208	0,69	-	1,03	0,47	5,36	1,44	0,27	0,18	12,56	3,61	6,95	2,87	57,38	27,54
Th232	1,55	-	0,65	0,33	0,40	0,03	0,05	0,01	4,43	1,30	4,84	0,64	32,23	14,03
U238	nd	-	nd	nd	nd	nd	nd	nd	0,60	0,19	1,43	0,21	7,11	3,07

Table 6: Trace element compositions for glass in in melt veins (GB), melt pockets (MP) and silicate melt inclusions (SMI) (in ppm).

Table7

[Click here to download Table: Table 7.doc](#)

SZB50					SZG23					FT12										
	Ol-II	Cpx-II	Sp-II	Glass	MP compo	SZT1111		Ol-II	Cpx-II	Sp-II	Glass	MP compo	FT08P		Ol-II	Cpx-II	Sp-II	Glass	MP compo	FT08P
Modal	0,13	0,34	0,17	0,36			Modal	0,12	0,5	0,13	0,26			Modal	0,44	0,19	0,05	0,33		
Na <sub>2</sub> O	0,01	1,07	0,00	4,16	<b>1,86</b>	2,90	Na <sub>2</sub> O	0,07	1,00	0,01	4,93	<b>1,79</b>	2,72	Na <sub>2</sub> O	0,01	0,77	0,01	5,15	<b>1,85</b>	2,72
MgO	49,09	15,65	20,81	4,20	<b>16,75</b>	18,07	MgO	48,02	13,28	18,55	3,88	<b>15,82</b>	17,60	MgO	49,58	14,58	21,08	3,61	<b>26,83</b>	17,60
SiO <sub>2</sub>	41,06	52,84	0,06	55,87	<b>43,43</b>	42,46	SiO <sub>2</sub>	41,38	46,63	0,09	56,33	<b>42,94</b>	43,18	SiO <sub>2</sub>	41,78	47,83	0,08	54,83	<b>45,57</b>	43,18
Al <sub>2</sub> O <sub>3</sub>	0,05	5,76	56,35	20,86	<b>19,05</b>	15,28	Al <sub>2</sub> O <sub>3</sub>	0,39	8,49	38,56	20,16	<b>14,55</b>	14,75	Al <sub>2</sub> O <sub>3</sub>	0,06	9,32	54,34	20,43	<b>11,26</b>	14,75
K <sub>2</sub> O	0,02	0,01	0,02	0,08	<b>0,04</b>	0,36	K <sub>2</sub> O	0,04	0,01	0,00	0,90	<b>0,24</b>	0,63	K <sub>2</sub> O	0,01	0,03	0,00	0,26	<b>0,10</b>	0,63
CaO	0,16	21,06	0,02	8,34	<b>10,19</b>	11,58	CaO	0,31	19,97	0,05	8,02	<b>12,11</b>	11,67	CaO	0,16	20,05	0,03	9,83	<b>7,13</b>	11,67
TiO <sub>2</sub>	0,05	0,43	0,23	3,67	<b>1,51</b>	1,20	TiO <sub>2</sub>	0,07	1,37	0,64	3,60	<b>1,71</b>	0,71	TiO <sub>2</sub>	0,02	1,77	0,27	3,62	<b>1,55</b>	0,71
FeO	8,99	3,20	11,28	1,62	<b>4,76</b>	4,09	FeO	8,27	2,98	14,54	1,52	<b>4,77</b>	4,11	FeO	8,23	3,14	10,63	1,64	<b>5,29</b>	4,11
P <sub>2</sub> O <sub>5</sub>	0,02	0,04	n.d	0,03	<b>0,03</b>	n.d	P <sub>2</sub> O <sub>5</sub>	0,04	0,01	0,01	0,08	<b>0,03</b>	0,04	P <sub>2</sub> O <sub>5</sub>	0,04	0,06	0,06	0,05	<b>0,05</b>	0,04
MnO	0,12	0,04	n.d	0,05	<b>0,05</b>	0,06	MnO	0,12	n.d	0,00	0,08	<b>0,04</b>	0,01	MnO	0,13	0,04	0,00	0,05	<b>0,08</b>	0,01
Cr <sub>2</sub> O <sub>3</sub>	0,08	n.d	10,85	n.d	<b>1,85</b>	n.d	Cr <sub>2</sub> O <sub>3</sub>	0,11	3,80	25,60	n.d	<b>5,24</b>	1,29	Cr <sub>2</sub> O <sub>3</sub>	n.d	2,52	12,31	n.d	<b>1,09</b>	1,29
<b>Total</b>	<b>99,91</b>	<b>100,85</b>	<b>99,82</b>	<b>98,98</b>	<b>99,88</b>	<b>97,55</b>	<b>Total</b>	<b>99,08</b>	<b>97,58</b>	<b>98,15</b>	<b>99,58</b>	<b>99,33</b>	<b>97,02</b>	<b>Total</b>	<b>100,34</b>	<b>100,40</b>	<b>99,01</b>	<b>99,56</b>	<b>101,03</b>	<b>97,02</b>

Table 7: Bulk melt pocket compositions based on mass balance calculation from modal and chemical compositions of phases. Comparison with pargasite amphibole compositions (SZT111 and FT08P).

**Table8**[Click here to download Table: Table 8.doc](#)

	Rock type	T primary (°C)	Estimated P (GPa)	T cpxII-glass (°C)	$\Delta T$ (°C)	P cpxII-glass (GPa)
<b>SZB16</b>	Lhz	1135	1.50			
<b>SZB44</b>	Lhz	992	1.28	1250	258	0.8
<b>SZB50</b>	Lhz	1007	1.14	1245	238	0.7
<b>SZB51</b>	Lhz	1039	1.27	1211	172	0.7
<b>SZB52</b>	Lhz	1128	1.59			
<b>SZB66</b>	Lhz	1029	1.36			
<b>SZG14</b>	Lhz	1086	1.30			
<b>SZG23</b>	Lhz	1041	1.30	1228	187	0.7
<b>SZG30</b>	Lhz	1052	1.25			
<b>SZG44</b>	Lhz	1086	1.17	1267	181	0.9
<b>FT12</b>	Lhz	968	1.15	1207	239	0.6
<b>FT01P</b>	Hbz	1137	1.63			
<b>FT08P</b>	Hbz	852	1.07	1222	370	0.6
<b>MSZK1306A</b>	Lhz	861	1.07			
<b>MSZK1308</b>	Lhz	1080	1.39			

Table 8: Minimum T and P of melt pocket formation in the lithospheric mantle beneath the BBHVF. T for the primary mantle mineral assemblage calculated after [Brey & Kohler \(1990\)](#); Estimated P from T equilibrium and [Kovacs et al. \(2012\)](#) geotherm;  $\Delta T$  = temperature difference between the mantle minerals and melt pocket phases